A Field Effect Gas Sensor based on Self-Standing Nanowire Arrays

Ramin Banan Sadeghian

A Thesis

in

The Department

of

Electrical and Computer Engineering

Presented in Partial Fulfillment of the Requirements

For the Degree of Doctor of Philosophy at

Concordia University

Montréal, Québec, Canada

August 2007

Your file Votre référence
ISBN: 978-0-494-31140-0
Our file Notre référence
ISBN: 978-0-494-31140-0

ABSTRACT

A Field Effect Gas Sensor based on Self-Standing Nanowire Arrays

Ramin Banan Sadeghian, Ph.D.
Concordia University, 2007

In this thesis we have introduced a novel gas sensor that works by fingerprinting the *ionization breakdown* characteristics of the unknown gases. This technique provides excellent selectivity; it is well established that at a constant temperature and pressure, every gas displays a unique breakdown electric field. In addition, because this technique does not involve adsorption or desorption of gases, the sensor exhibits a fast response and is not limited by considerations of reversibility and recovery.

We employed vertically-aligned, self-standing arrays of gold nanowires (AuNWs) at one of the electrodes of a miniature parallel-plate ionization cell. The AuNW arrays were synthesized using a tailored version of the electrochemical template-assisted technique, resulting freestanding structures with controlled sparseness. Individual AuNWs, owing to their nanoscale tips generate very high non-linear electric fields near their tips that provoke the breakdown process due to formation of a corona and allow self-sustaining discharges to be created at relatively low voltages.

In an alternative approach, we exploited the *tunneling field ionization* characteristics of the gases to identify the unknown gas type and measure its concentration. The phenomenon of field ionization consists of electron tunneling from gas atoms (molecules) through a potential barrier into a vacant energy level of the conduction band of a metal. It has been widely used in field-ion microscopy and mass spectrometry. However, the electric fields required to field-ionize gaseous species are in the range of 2–5 V/Å, orders of magnitude higher than the breakdown fields. With the provision of low voltage operation, this method can be utilized in detection of gases at very low concentrations. In this research, we also fabricated sensors using AuNWs with particular tip geometry and composition capable of field-ionizing gas particles at sub-10V voltages. The devices were successfully characterized using several gas species.

To my Family

ACKNOWLEDGMENTS

First and foremost, I thank my Lord almighty, for giving me knowledge, health, patience, and strength to complete my graduate studies in Electrical Engineering.

I would like to express my sincere gratitude to my supervisor, Dr. Mojtaba Kahrizi for his great support, guidance, and encouragement throughout my graduate studies. His expertise and competent pieces of advice have shaped the character of my research.

Through out my studies in Concordia, many people have helped and encouraged me in my research work. I am especially thankful to Dr. Simona Badilescu for her kindness, attention, and for her valuable scientific suggestions regarding my chemical experiments.

I have enjoyed the company of my colleagues in the nanotechnology group, Farshid, Nader, Ciwei, Nika, Sheikh, Svetlana, and Farah. I wish to thank them all for their friendship and support. Furthermore, I would like to thank Mr. Shailesh Prasad who assisted me in setting up the lab.

I am greatly thankful to Dr. Hojatollah Vali from McGill University for providing me with unlimited access to the SEM facilities at that university. Also, I would like to thank Dr. Yahia Djaoued from Université de Moncton for helping me in MicroRaman analysis.

I would also like to express my gratitude and thanks to my supervisory committee for their insightful reviews, comments, critics, and invaluable feedback.

Most importantly, I would like to reserve my deepest thanks to the love of my life, my dear wife, Atefeh, who supported and encouraged me during these years. I am also very much indebted to my dear parents, my first teachers, Almas and Jalil, who are my everything; this is for you.

TABLE OF CONTENTS

LIST OF TABLES

LIST OF FIGURES

LIST OF ACRONYMS

AAO	Anodized Aluminum Oxide
ADFET	Adsorption Field-Effect Transistor
AFM	Atomic Force Microscopy
AuNW	Gold Nanowire
CNT	Carbon Nanotube
DC	Direct Current
FEM	Field Emission Microscopy
FI	Field Ionization
FIM	Field Ion Microscopy
F-N	Fowler Nordheim
GIS	Gas Ionization Sensor
MCC	Monte-Carlo Collision
MOSFET	Metal-Oxide Field-Effect Transistor
MWCNT	Multi-Walled Carbon Nanotube
NEA	Negative Electron Affinity
NDR	Negative Differential Resistivity
NWFET	Nanowire Field-Effect Transistor
OGFET	Open-Gate Field-Effect Transistor
PAA	Porous Anodic Alumina
PIC	Particle in Cell
PPC	Parallel-Plate Cell
PS	Polystyrene
SBFE	Schottky Barrier Field Enhancement
SEM	Scanning Electron Microscope
SMU	Source-Measure Unit
SOC	System On Chip
SOI	Silicon On Insulator
SPA	Semiconductor Parameter Analyzer
TEM	Tunneling Electron Microscopy
TSFE	Two-Step Field Enhancement
WKB	Wentzel-Kramers-Brillouin

LIST OF SYMBOLS

P	Gas pressure		[torr]
c_g	Gas concentration		[cm^{-3}]
T_g	Gas temperature		[K]
G_r	Ion-electron generation rate		[$cm^{-3}s^{-1}$]
R_r	Ion-electron recombination rate		[$cm^{-3}s^{-1}$]
α_r	Recombination coefficient		[cm^3s^{-1}]
e	Charge per electron	1.602×10^{-19}	[C]
P_i	Dipole moment		[C·m]
α_p	Polarizability		[Cm^2V^{-1}]
n	Charged particle concentration		[cm^{-3}]
N	Number of gas molecules		–
N_s	Maximum number of adsorption sites per unit area		[cm^{-2}]
N_d	Semiconductor donor doping density		[cm^{-3}]
$\frac{dn}{dt}$	Rate of production of charged particles		[$cm^{-3}s^{-1}$]
n_e, n_i	Concentration of electrons and ions		[cm^{-3}]
μ_e, μ_i	Electron and Ion mobilities		[$cm^2V^{-1}s^{-1}$]
n_i	Ions produced per second per unit length direction		[$cm^{-4}s^{-1}$]
n_+	Secondary electrons generated per second		[$cm^{-3}s^{-1}$]
n_0	Primary leaving the cathode per second		[$cm^{-3}s^{-1}$]
n_a	Total electrons arriving at the anode		[$cm^{-3}s^{-1}$]
λ_e	Mean-free-path of electrons in the swarm		[cm]
V_b	Breakdown voltage		[V]
d, d_{gap}	Interelectrode distance		[cm]
E	Effective electric field		[Vcm^{-1}]
E_{app}	Applied electric field		[Vcm^{-1}]
E_{loc}	Local electric field at the sharp tips		[Vcm^{-1}]
J	Current density		[Acm^{-2}]

σ	Conductivity	[$\Omega^{-1}cm^{-1}$]
G	Conductance	[Ω^{-1}]
α	Townsend's primary ionization coefficient	[cm^{-1}]
ω/α	Total secondary electron factor	–
γ	Secondary electron factor by ion bombardment	–
β	Electric field enhancement factor	–
l	Nanowire length	[μm]
r_t	Nanowire tip radius	[nm]
E_F	Fermi level	[eV]
E_C	Minimum energy level of the conductance band	[eV]
E_V	Maximum energy level of the valence band	[eV]
ε_r	Relative permittivity	–
ϕ	Workfunction	[eV]
ϕ_{Bn}	Schottky barrier height	[eV]
χ	Electron affinity	[eV]
y	Image force barrier lowering factor	–
ϕ_S	Surface band bending	[eV]
λ_S	Field penetration depth	[Å]
U_I	Ionization potential	[eV]
U_P	Polarization energy	[eV]
D	Tunneling probability	–
τ	Characteristic time for ionization	[s]
v_e	Orbital frequency of the tunneling electron	[s^{-1}]
x_c	Critical ionization distance	[cm]

Chapter 1

Introduction

1.1. An Overview of Gas Sensors

Of late there has been an increasing demand in highly sensitive and selective solid-state gas sensors, whereas research and development of these devices began in 1950s. Since then the number and pace of such investigations have been growing in response to the increasing pressure placed on automotive and environmental industries, environment, public health and national security. Innovative concepts, both in device structure and operation principles, have been introduced recently. However miniaturization of such devices and at the same time maintaining reasonable functionality is still a challenge. Sensors are also critical in improving the reliability and efficiency of manufacturing operations by providing faster, more accurate feedback regarding product quality. In the area of environmental health and safety, lowering the limits of detection while improving its selectivity can improve the quality of life through better information regarding the pollutants in soil, water and air.

The following summarizes the requirements and constraints of an ideal gas sensor [1]:

1. Sensitivity
2. Selectivity
3. Reversibility
4. Fast response time
5. Durability

6. Non-contaminating
7. Simple operation
8. Portability
9. Simple fabrication
10. Temperature insensitivity
11. Stability against drift
12. Low noise
13. Low manufacturing cost
14. Maintainability

Obviously, no sensor could be made to fulfill all of these features, so that, as any other engineering problem, a trade off must be made among those factors which are more important. However, such detectors should allow continuous monitoring of particular gases in the environment quantitatively and selectively.

Gas detectors operate by various fundamentally different mechanisms. The detection method of gas sensors can be categorized into two main groups: (1) Calorimetric detection, which measures gas concentration versus temperature rise produced by the heat of reaction on a catalytic surface, and (2) Electrical detection, which measures the change in electrical parameters, such as conductivity change caused by adsorption or reaction of gases on the solid surfaces. Gentry and Jones [2], have extensively reviewed these two mechanism.

The latter method has been of more interest due to its faster response time and better reversibility; two major features of an ideal sensor device. Semiconducting metal oxides are the most widely used catalytic materials in fabrication of electrically detecting gas

sensors. They contain lattice defects due to an oxygen excess or deficit. The association of electrons with these defects, following adsorption, allows a certain change of the electrical conductivity of the oxide [2].

Recently, one-dimensional (1D) nanostructures made of metal-oxide semiconductors have attracted considerable attention in fabrication of catalytic based gas detectors because of their large surface-to-volume ratio [3-7]. Carbon nanotubes (CNTs), initially discovered by Iijima [8], are also being considered as prime materials for gas adsorption due to their large surface area and hollow geometry [9-12], and the significant influence of the gases on their transport properties [13-16].

On the other hand, in metals, the most significant parameter which changes due to adsorption of gas molecules at the surface, is the metal work function ϕ [2]. This change happens because of altering the charge distribution on the metal surface following the adsorption of certain gas molecules or atoms. Numerous devices can be made by which monitoring the work-function can aware us of the ambient gas concentration. In addition to work-function change, other phenomena taking place due to the gas adsorption are used in sensing applications, some of which include [1]:

- Changes in the optical parameters of materials such as reflectance, transmittance and absorptance (optical spectroscopic sensors).
- Changes in the dielectric properties of materials, mainly piezoelectric crystals (microbalance sensors).
- Changes in the wave propagation properties of surface acoustic wave devices (SAW sensors)

- Detection of the gas adsorption heat using pyroelectric materials (Pyroelectric sensors)
- Changes in the Fermi level of semiconductors, caused by adsorption of oxidizing or reducing gases (Resistive-film sensors, OGFETs, nanotube and metal oxide nanowire ADFETs).

1.2. Why Gas Ionization Sensors?

The conventional catalyst based sensors, however, suffer from sensitivity and selectivity issues, as their electrochemical cells cannot detect gases at low concentration [1]. In addition, it is difficult to detect gases of low chemical adsorption energy such as inert gases or those with low electronegativity toward the active layer [17, 18]. Also, different gases once were adsorbed may induce similar changes in the electrical properties of the catalyst [17]. Adsorption and absorption of chemicals, not only affect the response time of the sensor, but also limit its durability [19]. For the same reason, catalyst based sensors are limited by reversibility considerations.

To overcome the selectivity issues, the *ionization* characteristics of gases can be used to uniquely identify the gas type. Certain ionization sensors such as photo-ionization detectors (PID) , flame-ionization detectors (FID) [20], or electron-capture detectors (ECD) are not suitable for direct application to gas mixtures. These detectors should work in conjunction with a gas-chromatography set-up or mass spectrometer that separate the mixture into distinct bands that can then be qualitatively and quantitatively analyzed [21]. Furthermore, these instruments suffer by their huge, bulky structure, high power consumption and difficult high-voltage operation.

1.2.1. Breakdown Ionization Sensors

As a solution for miniaturization, researchers have recently introduced and developed gaseous breakdown ionization sensors [18, 19, 22-27]. These devices work by fingerprinting the ionization *breakdown voltage* of the unknown gas. Such a technique is feasible and provides improved selectivity, because it is well-established that at constant temperature and pressure, every gas has a unique breakdown electric field [28-30]. However, in uniform fields, the voltages required to cause gaseous breakdown are in the order of several hundred to thousand volts [29], therefore, either difficult or hazardous to employ. Recently, breakdown ionization sensors were reported using a film of vertically-aligned CNT arrays at one of the electrodes of a parallel-plate ionization cell to amplify the applied electric field and reduce the operating voltage [18, 19, 22-27]. Individual CNTs within the film, owing to their high aspect-ratio and sharp tips, provide very high nonlinear fields near the tips. This hastens the breakdown process due to formation of a *corona* or conducting filament of highly ionized gas that surrounds the CNT tips. This corona promotes the formation of an electron avalanche or plasma streamer that bridges the gap between the electrodes, and allows a self-sustaining interelectrode discharge to be created at relatively low voltages [19]. Ionization sensors identify gases by measuring these voltages, and if designed properly can determine the gas concentration by measuring the discharge current after the occurrence of breakdown [18, 19].

Figure 1.1 shows a diagram of the component parts and the configuration of the electrodes of the CNT-based breakdown ionization senor made by Modi et al. [19]. Multi-walled carbon nanotubes (MWCNTs) were grown on an SiO_2-covered Si substrate (**Figure 1.1c**). Nanotubes are 25 – 30 nm in diameter, 30 μm long, with an average

separation of 50 nm. Variable DC voltage was applied between the MWCNT film and the aluminum counter electrode, while the sensor was placed in a test chamber. The device was first tested in air with an electrode spacing of d = 150 μm and displayed a breakdown voltage of 346 V. The experiment was repeated with metal electrodes (no CNTs) having the same d. For this case, a breakdown voltage of 960 V was obtained [19].

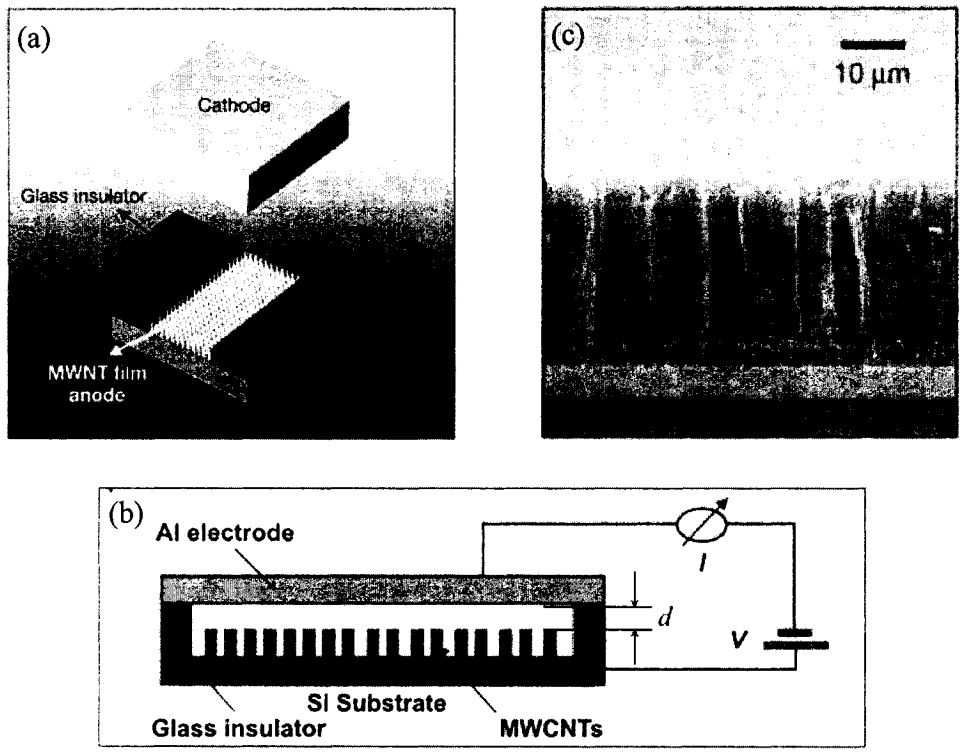

Figure 1.1 (*after Modi et al. in* [19]). The CNT-based breakdown ionization sensor. a) Exploded view of the sensor showing the nanotubes as the anode electrode and aluminum plate as cathode. b) Diagram of the test and measurement setup. c) SEM micrograph of vertically aligned MWCNTs on an SiO_2/Si substrate as the anode.

With the CNTs at the anode, the sensor was used to detect the identity of several gases, over a concentration range of 10^{-7} to 10^{-1} mol·liter^{-1} at room temperature (corresponding to a pressure range of 2×10^{-3} to 2×10^{3} torr) . Prior to each test, the chamber was evacuated to establish a base pressure of 10^{-4} torr. **Figure 1.2a** shows the

breakdown voltages of several gases under atmospheric pressure (760 torr), corresponding to a concentration of 0.04 mol·liter^{-1}. Note that for all the tests, the anode-cathode separation was kept at 150 μm. It can be seen that each gas exhibited a distinct breakdown behavior; helium displayed the lowest (164 V) and ammonia showed the highest (430 V) breakdown voltage [19].

The effect of gas concentration on the breakdown voltage was studied at reduced pressures. **Figure 1.2b** shows the breakdown voltages as a function of gas concentration (at room temperature). Note that according to the general law of gases, at a constant temperature, the pressure is proportional to concentration for a fixed chamber volume. Apparently, the breakdown voltages did not vary significantly with the gas pressure. It was suggested that the breakdown behavior in this case is governed by the highly nonlinear electric fields near the nanotube tips, resulting a pre-breakdown plasma that hastens formation of a streamer that bridges the electrode gap. The sensitivity of the breakdown voltage to gas pressure is therefore, reduced.

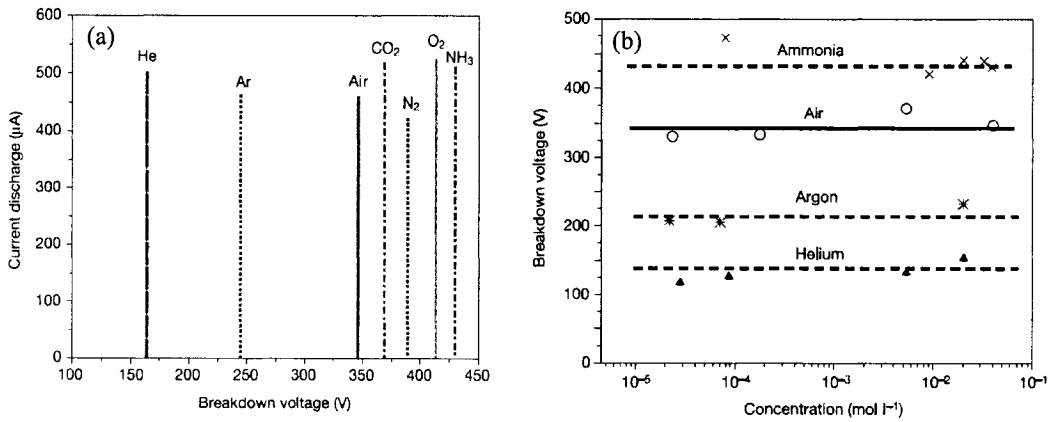

Figure 1.2 (*after Modi et al. in* [19]). Breakdown $I - V$ curves for NH_3, CO_2, N_2, O_2, He, Ar and air, showing distinct breakdown voltages at P = 760 torr; ammonia displays the highest breakdown voltage; and helium the lowest. b) Breakdown voltage as a function of concentration, showing only a weak dependence.

However, at very low concentrations (below 10^{-6} mol·liter^{-1} or 0.02 torr), the breakdown voltage increased according to Paschen's law for uniform fields [28-30]. It was concluded that a certain concentration threshold is needed for the discharge to be self-sustaining and therefore, lead to breakdown [19].

1.2.2. Field Ionization Sensors

The field-enhancement effect of sharp tips or protrusions can be also employed to field-ionize the unknown gas. Field ionization is defined as the process of extracting the valence electron(s) from the gas atom by tunneling through the metal/vacuum interface. Instead of the breakdown field, the *tunneling field-ionization* characteristic can then be used as a signature to fingerprint the unknown gas type and measure its concentration. The theory of field ionization is discussed in detail in Chapter 2. This principle was applied for the detection of gases at atmospheric pressure by Madou and Mossison [31]. Ghodsian et al. [32, 33] developed a standard silicon micromachining process that enabled low cost fabrication of a single field ionization tip.

Field ionization of elemental gases requires very high field strengths in the order of several V/Å. Such high fields are achievable only at the vicinity of sharp tips, for example, 10 kV must be applied to a metallic specimen, even with end radii of 50 – 100 nm to produce measurable field ionization [34]. As we will later discuss in the Chapter 2, the occurrence of field ionization, and the amplitude of the resultant current, depend strongly on the ionization potential of the gas particle. As a result, field ionization of organic molecules with ionization energies of 9 – 12 eV, entail much lower fields than elemental gas molecules having ionization energies above 12 eV.

Jiangbo et al. [35], applied an alternative method to detect gases, using field ionization. In their approach, instead of sensing the gas directly, the gas molecules were first ionized and then the ionized molecules were sensed by a single CNT-based ion sensor. The adsorption of ionized gas molecule on the carbon nanotube surface introduces electrons into the material and consequently changes the current of the sensor, much alike catalyst based sensors. They showed that the adsorption and desorption of an ionized gas molecule are much faster than neutral molecules.

Figure 1.3 shows a schematic illustration of the single CNT, gas sensing system. The MWCNT is assembled onto the electrodes with an AFM nanomanipulation system, and placed into the sensor chamber where the ionized gas is fed.

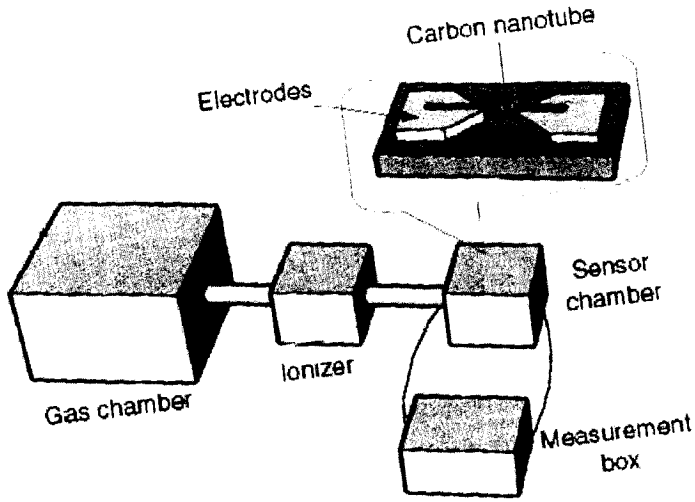

Figure 1.3 (*after Jiangbo et al. in* [35]). Schematic of the single carbon nanotube gas sensing system.

The sensor was characterized particularly in ionized oxygen, where the current through the CNT was measured under a constant bias. It was demonstrated that the ion sensor exhibits a reversible response with a recovery time of a few seconds, whereas traditional CNT-based sensors have recovery times of about several minutes. However, such a sensor requires a companion bulky field-ionizer to supply the ionized gas.

Both the breakdown-ionization- and field-ionization- sensors are the subject of this research and henceforth they will be referred to as Gas Ionization Sensors (GISs).

1.3. Objective of the Research

The goal of this research is to introduce, fabricate and characterize a novel miniature GIS, using vertically-aligned nanowire arrays. The proposed device is intended to offer enhanced selectivity, sensitivity and speed of response and fast recovery time, over the previous nanostructured catalyst based sensors. Depending on the composition and geometry of the nanowires, our sensor can be operated in either breakdown-ionization or field-ionization modes. In terms of the operation principle, our device differs from conventional field-effect devices where electric fields modulate the conduction through the channel. Instead, the electric field is used to initiate conductance through an ionization process.

Even CNT-based ionization sensors may suffer from reversibility concerns. Extremely dense CNTs make dispersion of the gas difficult, so the sensor cannot be reused prior to some sort of cleaning treatment [22]. Single-walled carbon nanotubes (SWCNTs) and MWCNTs are both known to absorb and react with certain gases, thus making them a poor choice for a durable ionization sensor [13-16]. Additionally, the

generated heat in the CNT ionization sensors operating in the corona discharge region may destroy sharp and slender CNTs. It is therefore, favorable to employ a chemically inert and mechanically robust material instead of CNTs.

In this work we used electrochemically-grown freestanding arrays of gold nanowires (AuNWs), as a replacement for CNTs. AuNWs, apart from being more robust and chemically inert, are much easier to synthesis and their geometry could be tailored during the electrochemical deposition. A modified version of the template-assisted electrochemical nanowire synthesis technique was developed and employed in this work. The original version of this method has been widely used in the fabrication of nanostructures due to its low cost and simplicity [36-41]. In addition, it provides an efficient control on the aspect ratio of the nanowires.

We fabricated several GISs by incorporating a variety of freestanding AuNW films with different geometries and compositions at one of the electrodes of a standard ionization cell, with constant electrode spacing. Devices containing regular AuNWs were tested in the ionization breakdown mode. The curves of breakdown voltage against gas pressure were extracted and the effect of electrode polarity of the breakdown GISs on the output characteristic was also studied. It was demonstrated that when the AuNWs are at the cathode electrode, the sensor displays a superior performance than anode-AuNWs.

On the other hand, film of AuNWs terminated with gold nanoparticles at their tips, and containing a thin layer of residual alumina were used in GISs that operate by field-ionizing gaseous species. These devices provided very high electric fields capable of ionizing gas molecules. The resultant field-ion $I - V$ was employed to identify the gas type and determine its concentration.

Note that the field strengths required for field ionization of typical gases are much higher than their breakdown fields. However, contrary to breakdown, a high electric field is required 'locally' at the specimen tip where tunneling ionization takes place. In other words, in order that field ionization occur before breakdown, electron multiplication must be insufficient to cause a self-sustaining discharge. The above conditions impose geometrical constraints on the device. Particularly, the field ionization sites at the anode (i.e. high aspect ratio protrusions) must have sharper tips, while they can be much shorter with respect to the electrode separation. In addition, in this case, the electrode separation itself must be as small as possible to reduce the amount of electron multiplication.

We believe that this work will open up a brand new class of electron devices that their operation principle follows a combination of solid-state electronics and vacuum/gas physics. In addition to successful fabrication and characterization of the sensors, we carried out simulations and numerical analysis to predict the breakdown voltage of the breakdown GIS and the overall field enhancement factor of AuNWs in both the breakdown and field-ionization GISs.

1.4. Organization of the Dissertation

There are six chapters in this dissertation and they are organized in the following topics:

- *Chapter I* provided an overview of regular gas sensors, gas ionization sensors, motivation for the development of miniature gas ionization sensors based on nanowires. The advantages and suitability of AuNWs and the template-assisted growth technique were also explained.
- *Chapter II* presents the theoretical background of gas ionization, including the electron-impact and tunneling-field ionization mechanisms. This chapter also provides a review on the geometrical field enhancement phenomena of sharp protrusions, and electron field emission.
- *Chapter III* describes the nanowire synthesis process steps in detail, and the characterization of the as-grown AuNW films.
- *Chapter.IV* explains the device fabrication process and characterization methods, including low level measurement techniques.
- *Chapter V* presents the results, analysis and discussion of the experimental work.
- *Chapter VI* Concludes the achievements of the research.

Chapter 2

Theoretical Background

2.1. Ionization and Breakdown

In this section, we treat the theory of the ionization of gases. In the beginning, an overview of common ionization principles will be presented. Among these ionization methods, we will focus on *electron impact ionization* mechanism that leads to the breakdown of gas, because Gas Ionization Sensors (GISs) work by measuring the breakdown voltage of the unknown gas. The discharge and breakdown characteristics will therefore be given attention in the ensuing sections. In addition, tunneling field ionization of gases as a separate approach will be covered at the last section. Our theoretical reflections will then be implemented in the fabrication and characterization of GISs that work by either mechanism.

2.1.1. Principles of Ionization

Under normal conditions, any sample of gas can be expected to contain a number of electrons and ions. For instance, at ground level, the atmosphere contains an order of 1000 positive and negative ions per cm^3 generated due to cosmic and ultraviolet radiation and radioactivity. The rate of ionization which maintains this number is in the range of 2 – 10 $cm^{-1} \cdot s^{-1}$ [28]. The density of these 'natural' ions is therefore, negligible. Only when a significant part of a gas is ionized we speak of *plasma*. To ionize a neutral particle, either an electron must be extracted from the electron cloud, or added to it. The former

mechanism requires energy and the latter releases it. Note that, the ionization discharge and breakdown processes are mainly governed by valence electrons, as the electrons at higher states are tightly bonded to the nucleus and do not contribute.

Various mechanisms enable ionization of neutral gas particles. In the following we briefly introduce each mechanism:

Field ionization: Consists of pulling electron(s) out of the atom's electron cloud under the action of very high electric fields (~10 V/Å), thus creating positively charged ions. The process is hastened at the vicinity of a positively biased metal by tunneling and is described in detail in section 4 of this chapter.

Impact ionization: Collision with energetic electrons or particles can force electrons out of the shell, excite the particle, or dissociate molecules. Excited (metastable) molecules may pass their energy to others and ionize them.

Thermal ionization: In case sufficient energy is supplied to the gas by heating, the binding energy of atoms and molecules are overcome and therefore they are ionized. Flame Ionization Detectors (FIDs), for instance, use hydrogen-oxygen flames to pyrolyze most organic compounds, producing ions and electrons [20].

Photoionization: Photoionization takes place upon the absorption of the incident photon if its energy exceeds the ionization potential of the atom. If the later is in the ground state and has ionization potential of U_I, the photon frequency ν, must be such that:

$$h\nu \geq U_I, \tag{2.1}$$

Here the quantum can still be absorbed if its frequency is in excess of the threshold value; the excess is imparted to the released electron as kinetic energy. The critical frequency for most gases lies in the X-ray region and for metal vapors in the UV.

Radioactive ionization: Radioactive irradiation excites particles and ionizes neutrals. Natural ionization by cosmic rays is an example.

Processes where ionized particles play an important role in gaseous electric conduction are called *discharges*. Here we begin by introducing the different regions of a discharge.

2.1.2. Different States of a Discharge

In a two electrode configuration, there are always a few electrons available due to the above phenomena. The rate of gas ionization and emission from the electrodes can be greatly increased by using external radiation sources of sufficient frequency [28].

In the equilibrium state, where there is no electric field, the rate of generation of charged particles G_r, is balanced by the rate of recombination R_r, therefore the net rate of charged particle production per unit volume is

$$\frac{dn}{dt} = G_r - R_r = 0\,, \tag{2.2}$$

In small electric fields, current flows by the movement of already existing ions and electrons, that may upset the equilibrium. In this case, the value of current is proportional to the speed at which electrons and ions move toward the electrodes; as the mobilities are almost constant, the current density J, is proportional to the field strength E. Therefore, under these conditions, the gas is an ohmic conductor whose conductance depends upon

the mobilities and number of charged particles (the electron and ion generation rate, and the recombination):

$$J = \left(n_e \mu_e + n_i \mu_i\right) \cdot eE\,, \tag{2.3}$$

where n_e and n_i are the number of electrons and ions, and μ_e and μ_i are their drift mobilities respectively, assuming to be constant under these conditions.

At a higher E, the equilibrium is upset by the number of electrons and ions reaching the electrodes and being neutralized. This increases the effective recombination coefficient α_r, and therefore reduces total charge particles. Consequently, the rate of increase of current with voltage decreases. If the generation rate remains constant, a limiting condition is reached as E increases when all the electrons and ions reach the electrodes before they have the time to recombine. The total number of charges arriving at the electrodes is then equal to the number being produced, so that

$$J = d_{gap} e \frac{dn}{dt}, \tag{2.4}$$

where d_{gap} is the distance between the electrodes, e is the electron charge, and dn/dt the total rate of production of charged particles per unit volume, assuming all to be singly charged. The current density does not depend on E nor on the mobilities, and is called the *saturation current density*. Between the stage where $J \propto E$ and the saturation stage, the dependence of J upon E can be determined by considering the combined effect of carrier recombination and current to the electrodes on the rate of disappearance of charges, and an equation can be obtained.

The current density is usually very small under these conditions, indeed less than 10^{-9} $A \cdot cm^{-2}$ [28]. The discharge is quite dark, since the rate of excitation is comparable with

the low rate of ionization and the resultant emission too weak to be visible. This kind of discharge is non-self-sustaining, as it depends on external radiation; it is the principle cause of leakage from charged bodies and the starting point of various forms of discharge. One can produce such a discharge by using a heated cathode to provide electrons. The action when saturated resembles a temperature-limited thermionic diode.

If the field is increased further after the saturation has reached, there comes a state at which the current again increases. The nature of the increase depends on the gas pressure and type, and as far as a *low-pressure* case is considered (typically a few torr), there are still many mean free paths between the electrodes. With increasing the voltage, the current rises at an increasing rate until the breakdown voltage V_B is reached. **Figure 2.1** shows the $I - V$ characteristic of the discharge up to this point. The characteristic between the region of saturation and the point of breakdown represents the *Townsend* discharge.

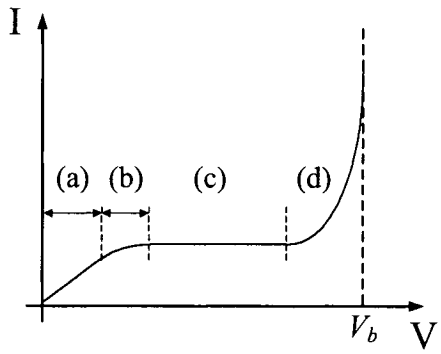

Figure 2.1. Volt–ampere gaseous discharge characteristic in uniform fields, up to the breakdown point V_b. (a) Ohmic region, (b) transition to saturation, (c) saturation, (d) pre-breakdown Townsend discharge.

Before breakdown, a number of factors contribute to the current between the electrodes. These factors depend on the material, geometry and the ambient conditions (gases/vapors, pressure and temperature) around the electrodes. **Figure 2.2** illustrates

different pre-breakdown conduction mechanisms, followed by definitions for each [42]. After breakdown, electron transport through the ionized gas between the electrodes is the main contribution to the current that increases by orders of magnitude when breakdown occurs.

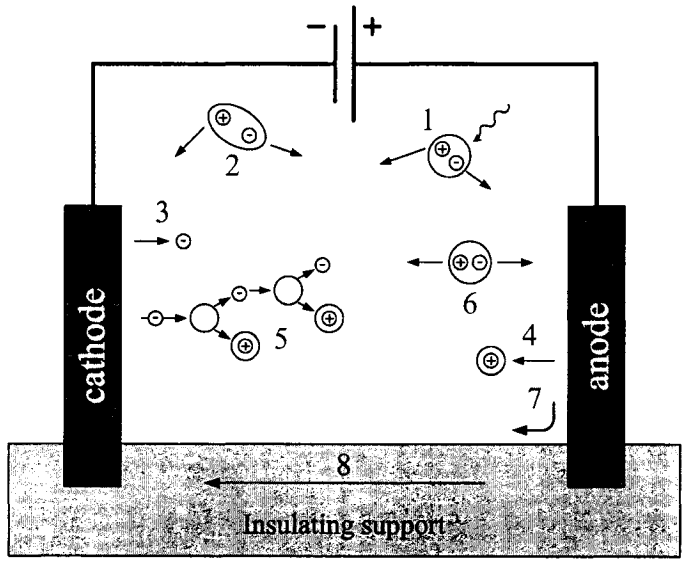

Figure 2.2 (*adapted from Longwitz* [42]). Variety of conduction mechanisms in a double electrode gap prior to breakdown.

1. Radiation induced ionization (photons, cosmic rays) [28-30].
2. Charge transfer by particles. Strong fields may pull particles off an electrode surface. Such particles may trigger a breakdown.
3. Electron field-, secondary electron- or photoelectron-emission [28-30, 43].
4. Field desorption, evaporation or ionization [34, 43-45].
5. Charge multiplication by electron impact [28-30].
6. Dissociation of neutral particles.
7. Conduction over adsorbed layers.
8. Insulator leakage current.

2.1.3. Initiation of Electric Breakdown, the Townsend Mechanism

Suppose that in addition to n_0 electrons per second leaving the cathode (liberated by photons, cosmic rays or field emission), there are n_i ion-electron pairs produced per second per unit length along the field direction. Then in a length dx, distant x from the cathode, the increase dn in the electron flow per second is partly due to ionization by the electrons entering the element (n per second) and partly due to the ionization of the atoms within the element (e.g. photoionization). Therefore

$$dn = \alpha n dx + n_i dx, \tag{2.5}$$

where α is known as Townsend's first ionization coefficient and represents the number of ionizing collisions an electron makes by traveling the unit distance [28].

Integration from the cathode surface, where there are n_0 electrons, toward anode at a distance x, where there are n electrons yields:

$$\int_{n_0}^{n} \frac{dn}{\alpha n + n_i} = \int_0^x dx, \tag{2.6}$$

and from that, the number of electrons at x is given by

$$n = n_0 e^{\alpha x} + \frac{n_i}{\alpha}\left(e^{\alpha x} - 1\right), \tag{2.7}$$

where $n = n_a$ and $x = d_{gap}$ at the anode end. If we include emission of secondary electrons, n_+, from the cathode as well, the above equation can be re-written as

$$n = \left(n_0 + n_+\right)e^{\alpha x} + \frac{n_i}{\alpha}\left(e^{\alpha x} - 1\right), \tag{2.8}$$

A steady state condition demands that the difference between the number of electrons arriving at the anode and the number leaving the cathode shall equal the number of generated electrons, or the total number of ions arriving at the cathode. Therefore:

$$n_a - (n_o + n_+) = \frac{n_+}{\omega/\alpha} + n_i d\,, \tag{2.9}$$

where ω/α is known as Townsend's secondary ionization coefficient representing the number of secondary electrons produced per primary ionization (α). ω/α is actually the sum of the individual coefficients representing various secondary ionization processes which are in turn each related to emissive properties of the cathode for the various types of interaction involved and can be written as:

$$\omega/\alpha = \gamma + \beta/\alpha + \delta/\alpha + \varepsilon/\alpha + \ldots, \tag{2.10}$$

where γ is the number of electrons ejected from the cathode per incident positive ion, β is a coefficient representing ionization of gas atoms by collision with positive ions, and δ/α is the number of secondary photoelectrons produced per primary electrons [29]. Among these processes, secondary electron emission by bombardment of cathode, the γ process, is usually the most predominant. Therefore, we may write:

$$\omega/\alpha \approx \gamma\,. \tag{2.11}$$

By combining (2.8) with (2.9), we get

$$n_a = \frac{e^{\alpha d}}{1-\gamma\left(e^{\alpha d}-1\right)}\left(n_0 + \frac{n_i}{\alpha} - n_i\gamma d\right) - \frac{n_i}{\alpha}, \tag{2.12}$$

and after some algebraic manipulations, (2.12) can be written in the following form:

$$n_a = \frac{n_i}{\alpha}\cdot\frac{(1+\gamma)\left(e^{\alpha d}-1\right)-\alpha\gamma d e^{\alpha d}}{1-\gamma\left(e^{\alpha d}-1\right)} + \frac{n_0 e^{\alpha d}}{1-\gamma\left(e^{\alpha d}-1\right)}\,. \tag{2.13}$$

Equation (2.13) represents our version of the pre-breakdown current, which includes the contribution of electron-ion pair generation by cosmic radiation (process #1 as

illustrated in **Figure 2.2**) that is independent of the primary ionization process. Evidently, for $n_i = 0$, (2.13) reduces to the well-known Townsend's formula [28-30],

$$n_a = \frac{n_0 e^{\alpha d}}{1-\gamma\left(e^{\alpha d}-1\right)}. \tag{2.14}$$

The $I - V$ curve of **Figure 2.1** shows a sharp rise at the breakdown voltage V_b. The current may increase 10^6 folds if the circuit permits. Equation (2.14) shows that the Townsend current becomes theoretically infinite if

$$\gamma\left(e^{\alpha d}-1\right)=1. \tag{2.15}$$

The characteristic may therefore, be interpreted by supposing the increasing voltage, and thus field, in the Townsend region (region (d) in **Figure 2.1** to affect α and γ in a way that this unstable condition is reached and the current rises uncontrollably until some other limitation sets in. The condition, therefore, forms a possible breakdown criterion, known as the *Townsend criterion*, or the *sparking criterion*. The criterion defines the onset of a kind of positive feedback when each primary electron produces at least one secondary electron which can then carry on the process. Since the production of electrons becomes independent of the external radiation, previously essential, we have a *self-sustaining* discharge.

2.1.4. Paschen's Law

Experiments confirm that α and γ are functions of a quantity known as the reduced field, that is, E/P [28, 29], where P is the gas pressure. It is found that they are uniquely determined by E/P within a wide though limited range, and are written as

$$\frac{\alpha}{P} = \varphi\left(\frac{E}{P}\right), \tag{2.16}$$

and

$$\gamma = \psi\left(\frac{E}{P}\right). \tag{2.17}$$

A general form of (2.16) was derived approximately by Townsend, given by

$$\frac{\alpha}{P} = Ae^{-BP/E}, \tag{2.18}$$

where A and B are constants that depend on the gas used [28]. There has been no particular analytical expression for γ reported in the literature, as it also depends on the cathode material and microstructure. Since in uniform fields we have $V_b = Ed$, Townsend criterion may be written as

$$\psi\left(\frac{V_b}{Pd}\right)\left(e^{Pd\varphi\left(\frac{V_b}{Pd}\right)} - 1\right) = 1. \tag{2.19}$$

Which is identical to the case where for a fixed $P{\cdot}d$, the breakdown voltage V_b, is also fixed; hence V_b depends only on the product of gas pressure and electrode spacing and we may write

$$V_b = f(Pd), \tag{2.20}$$

for uniform fields. Since the general law of gases requires that

$$P = \frac{Nk_B T}{\mathrm{V}}, \tag{2.21}$$

where N is the number of gas molecules, T is the thermodynamic temperature (in Kelvin) and V is the volume, to avoid stipulation of constant temperature, (2.20) can be written as

$$V_b = g(Nd). \tag{2.22}$$

Equations (2.20) and (2.22) express the experimental relationship known as *Paschen's law*. It holds widely, although there are exceptions to it. For instance experiments show that in micrometer separations due to electron field emission from the cathode, V_b depends on the field and is no longer a function of Pd [29, 46-49].

It is possible to obtain analytical forms for f (or g), based on expressions for α which have limited validity but agree with experiment in one important respect: The curve of V_b versus Pd for any combination of gas and electrode has a unique minimum. The minimal value of V_b is called the *minimum sparking*, or *breakdown potential*, $(V_b)_{\min}$, and is in the order of several hundred volts. For instance, Held et al. [50] obtained the following relationship for uniform fields:

$$V_B = B\frac{(Pd)}{\ln\left(\frac{A}{\ln(1+1/\gamma)}\right)+\ln(Pd)}, \tag{2.23}$$

and $(V_b)_{\min}$ and its corresponding $(Pd)_{\min}$ are given by:

$$(V_B)_{\min} = B\cdot(Pd)_{\min}, \tag{2.24}$$

and

$$(Pd)_{\min} = \frac{e\ln(1+1/\gamma)}{A}. \tag{2.25}$$

Figure 2.3 shows some experimental curves [28]. The existence of V_b is readily explained qualitatively: for $Pd > (Pd)_{min}$, the number of collisions made by an electron in crossing the gap is higher than at the minimum but the energy gained between collisions, and hence the possibility of ionization at a collision, is much lower unless the voltage is increased; for $Pd < (Pd)_{min}$, the reverse holds.

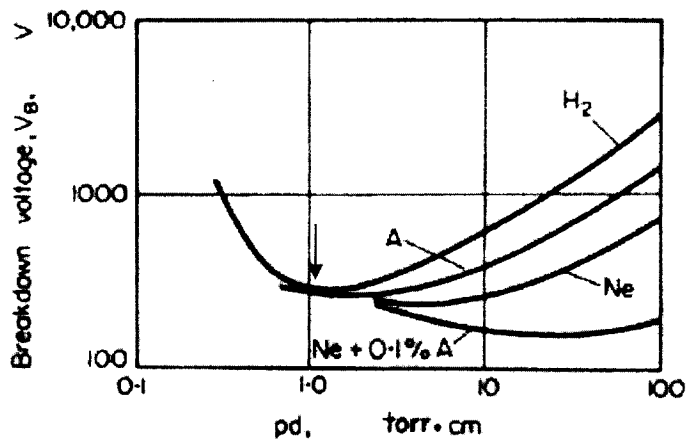

Figure 2.3 (*adapted from Howatson in* [28]). Variation of breakdown voltage, for uniform fields. The arrow shows the $(V_b)_{min}$ of H_2.

In certain cases small admixtures of gases have drastic effects on the curves of V_b; for example a small amount of Ar greatly lowers the breakdown voltage of Ne. This is due to metastable Ne atoms causing ionization of the Ar by the *Penning* effect [29, 51].

2.1.5. Breakdown in Non-uniform Fields

The Townsend theory of discharge can be applied to non-uniform field conditions as well, but the product αd must be replaced by its effective value:

$$\langle \alpha d \rangle = \int_0^d \alpha(x) dx . \tag{2.26}$$

Although this can be inserted in (2.15), calculations of V_b from the resulting equation would be difficult. For the simple case of parabolic point-to-plane geometry, Held et al. [50] plugged the following expression for the electric field distribution in (2.18)

$$E(z)=\frac{V}{(d+r_t/2-z)\ln(2d/r_t+1)}. \tag{2.27}$$

where d is the point to plane distance and r_t is the radius of the parabolic point, and found

$$V_B' e^{-B\frac{r_t}{2d}\frac{Pd}{V_B'}}\left(1-e^{-B\frac{Pd}{V_B'}}\right)=\frac{B}{A}\ln(1+1/\gamma). \tag{2.28}$$

where V_b' is the breakdown voltage in this geometry. Derivation with respect to Pd yields

$$(V_B)'_{\min}=B\cdot(Pd)'_{\min}, \tag{2.29}$$

and from that

$$(Pd)'_{\min}=F(r_t,d)\frac{\ln(1+1/\gamma)}{A}. \tag{2.30}$$

where the geometrical factor F is given by

$$F(r_t,d)=\left(\frac{r_t}{2d}+1\right)\ln\left(\frac{2d}{r_t}+1\right)\exp\left[\frac{r_t}{2d}\ln\left(\frac{2d}{r_t}+1\right)\right]. \tag{2.31}$$

In the asymptotic limit is where $r_t/2d >> 1$, equations (2.28), (2.29) and (2.30) reduce to (2.23), (2.24) and (2.25) respectively. Paschen's law may not apply for non-uniform fields in more complex geometries [52]. The variation of γ with the field at the cathode means that V_b depends on the polarity. For the common geometries that generate nonuniform fields (e.g. coaxial, point-to-plane and etc.), where the field is greater at the stressed electrode, the value of γ is normally greater when this electrode is the cathode. V_b is therefore expected to be lower when the stressed electrode is negative than when it is

positive [28]. This is confirmed by experiment, although not without exception [29]. The curves of V_b against pressure show minima corresponding to the Paschen curves for uniform fields. The curvature of the $V_b - Pd$ characteristic for $Pd > (Pd)_{min}$ however, is less, compared to that of uniform fields [50]. Discharges in highly non-uniform fields are generally known as corona, but this term is more often reserved for high pressures.

2.1.6. Corona

In non-uniform fields, breakdown at high pressures is, as at low pressures, markedly dependent on the geometry of the electrodes and on their polarity. It is however, distinguished from the low-pressure case by the appearance of *corona* [28, 30]. Corona, while may not constitute the breakdown of the gas itself, can carry appreciable current (of the order of 1 mA) and can be self-sustaining. It requires photoionization of neutrals in the medium. The resulting electron creates further electron-ion pairs by collisions with neutral atoms, which eventually form an avalanche. Coronas are named based on the polarity of the stressed electrode. Both positive and negative coronas rely on electron avalanches. In processes which differ between positive and negative coronas, the energy of these plasma processes is converted into further initial electron dissociations to seed further avalanches.

In a positive corona, electrons are attracted towards the stressed electrode. Secondary electrons are generated predominantly by photoionization in the plasma. Negative coronas on the other hand depend on secondary emission form cathode [28].

2.2. Geometrical Field Enhancement

Similar to Field-Ion- and Field-Emission Microscopy (FIM and FEM), knowledge of the distribution of the electric field and potential within the GIS is of fundamental importance, since the field strength in the gap determines the overall breakdown conditions. At the metal-vacuum (AuNW-vacuum) interface, it also dictates the rate of electron field emission and ionization in the field limited regime. Regional differences over the AuNW tip surface control the local gas supply function and affect the local rate of field ionization and evaporation. However, unlike FIM applications, the trajectories of the gas ions are not important in an ionization sensor. Therefore, atomic scale variations of the field which determine the FIM image contrast can be neglected. It is instructive to begin with theoretical expressions to estimate the field strength at the tip of a AuNW.

In geometrical configurations resembling a parallel-plate capacitor, the applied electric field, often called the *applied macroscopic field*, is defined as

$$E_{app} = V/d, \tag{2.32}$$

where V is the voltage applied across the electrodes and d is the gap spacing between them. Obviously, E_{app} is uniform in the gap spacing, providing that the lateral dimension of the capacitor be very much greater than d. Enhancement of the electric field takes place at the vicinity of conductive sharp tips or protrusions on one of the flat planar electrodes, which we term the *emitter plane*. **Figure 2.4** shows a schematic illustration of a sharp tip. The upper-limit of the local field amplitude E_{loc} at the apex of a hemisphere is basically reduced from the equivalent value at the surface of a free conducting sphere by the presence of the shank by a factor of k_f and can be expressed as

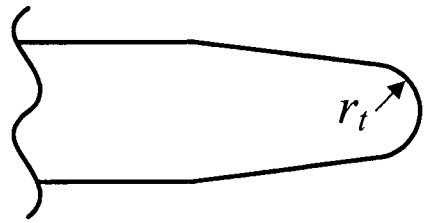

Figure 2.4. The shape of a typical field enhancing specimen. r_t denotes the tip curvature.

$$E_{loc} = V/k_f r_t\,, \tag{2.33}$$

where r_t is the apex radius, and k_f is a numerical constant which depends on the taper angle of the protrusion, with an average approximate value of 5 [43].

It is imperative to note that the E_{loc} defined by (2.33), corresponds to the field strength within 1 – 2 Å of the surface atoms and can be applied in field ionization and field emission processes, where the field at the interface determines the ionization rate and the emission current respectively. For instance Sakurai and Müller [53] studied the energy of ions produced by free space field ionization and found k_f to be in the range of 5 – 8 for slender etched protrusions, depending on the cone angle. This value dropped to ~3 if the specimen was annealed at high temperature, because of the bulb shape formed at the apex by blunting effects.

The field-enhancement factor in general, is defined as the ratio between E_{loc} to the applied field E_{app}, or

$$\beta = E_{loc}/E_{app}\,, \tag{2.34}$$

The question then arises of how the values of β can be estimated. In fact, β has been the subject of analytical, computational and experimental investigations and several formulas have been obtained to predict a value for it based on the geometrical model for the microprotrusion or nanoprotrusion [54, 55]. These geometrical models include

"hemisphere on a plane", "hemisphere on a post" and "hemi-ellipsoid on plane". In this research we employed the "hemisphere on a post model" [54], because it suits the most to our fibrillar AuNWs. This model is illustrated in **Figure 2.5**.

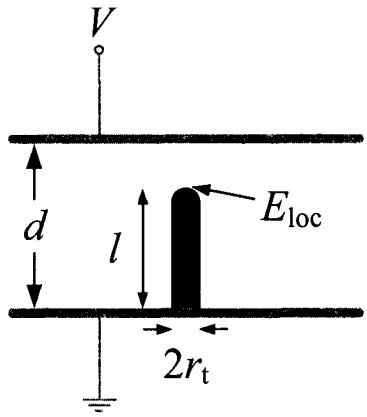

Figure 2.5. Geometrical model for a field-enhancing hemisphere-on-post. See text for the exact definitions of symbols.

We need to note that the discussion assumes that the scale of the total length of the protrusion (nanowire) l, to be much smaller that the plane-to-plane gap spacing d. Otherwise, β will be conversely affected. Miller [56] showed that the effective value of β depends on d, according to

$$\beta(d) = \beta|_{d=\infty}[1 - l/d]. \tag{2.35}$$

A suitable unifying expression of various results for β was given by

$$\beta \approx 2 + l/r_t = 3 + h/r_t, \tag{2.36}$$

in which $h = l - r_t$ stands for the length of the post [54]. This formula is in fact a special case of the general 'paraboloid on a plane' model, given by

$$\beta \approx 3 + h/r_t \cos\theta, \tag{2.37}$$

where the polar angle θ equals, for instance, 45° for a pyramid and 0° for a hemisphere. In the limit that $l >> r_t$, (2.36) is reduced to

$$\beta \approx l/r_t \,, \tag{2.38}$$

which is used often as a rough approximation. However, it has been discussed that (2.36) or (2.38) significantly over-predict the value of apex enhancement factor β, at large values of l/r_t [54].

For convenience of discussion hereafter, we introduce the symbol v to denote the ratio of protrusion length to the post base (or hemisphere) radius, or $v = l/r_t$. In the range of $4 \le v \le 3000$, the factor β is adequately represented, to within $\pm 3\%$, by [54]:

$$\beta \cong 1.2(2.15 + v)^{0.90} \tag{2.39}$$

A simpler formula, applicable within the range $30 \le v \le 2000$, and valid to within $\pm 25\%$, is

$$\beta \approx 0.7v \,. \tag{2.40}$$

The conventional formula (2.39) is a good approximation for smaller values of v. The results of finite element analysis performed in [57] and presented in **Figure 2.6**, show the extent of validity of the above formulas [54].

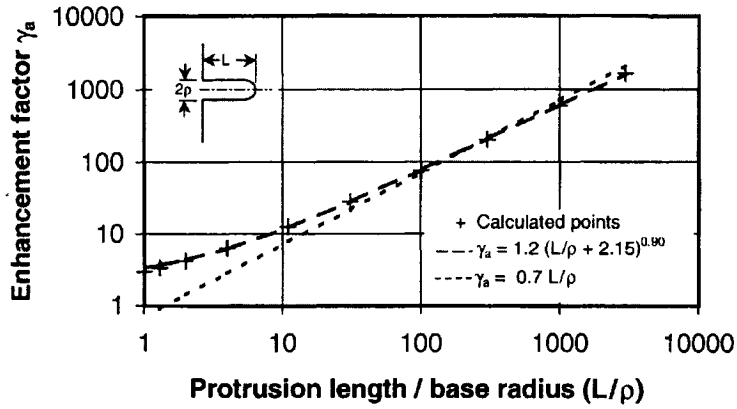

Figure 2.6 (*adapted from Forbes et al. in* [54]). Calculated results for the field-enhancement factor β (here γ_a), for the 'hemisphere on post' model. The fitted curved line corresponds to (2.39) and the fitted dashed straight line corresponds to (2.40). 'Calculated points' refer to the simulated results.

The nominal range of values predicted for high aspect ratio structures such as carbon nanotubes lie within $20 \lesssim \beta \lesssim 1650$ [54, 55]. However, it is well-established that if the protrusion is of atomic or sub-atomic scale, the abovementioned models are not correct, and the distribution of electron charge needs to be calculated using quantum mechanics, and the field distribution deduced from the atomic-level charge distribution [34, 44].

2.2.1. The Two-Step Field Enhancement (TSFE) Model

This model is a modified version of the simple field enhancement model developed to account for the complicated morphology of a nanowire tip [58]. The surface of a nanowire tip may contain a number of small protrusions or whiskers that act as tiny tips. The nanowire with a height of l_1 and tip curvature of radius r_{t1} is assumed to consist of a number of tiny tips with height l_2 and tip radius r_{t2} as shown in **Figure 2.7**.

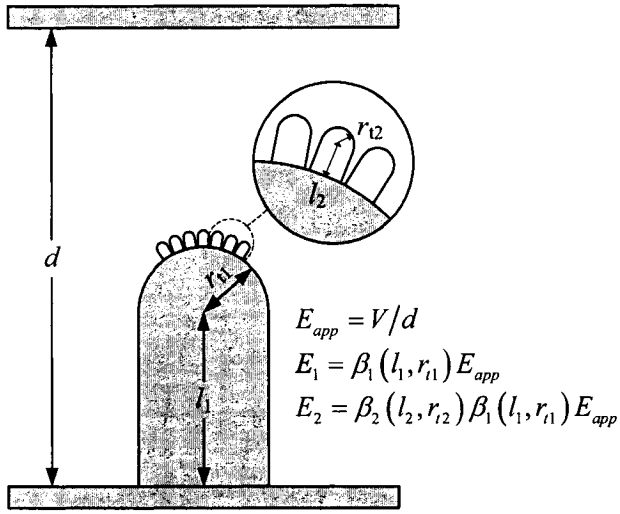

Figure 2.7. Schematic illustration of the two step field enhancement model

The electric field on the blunt tip is equal to

$$E_1 = \beta_1(l_1, r_{t1})E_{app}, \tag{2.41}$$

and the field at the end of the tiny protrusion is equal to

$$E_2 = \beta_2(l_2, r_{t2})\beta_1(l_1, r_{t1})E_{app}, \tag{2.42}$$

where either (2.39) or (2.40)can by used to as β_1 and β_2.

The TSFE approach was used earlier to explain field emission from diamond coated silicon field emitters [59, 60]. The model is useful in particular to justify the high enhancement factor and the resultant low-voltage field ionization and field emission observed form our AuNWs containing gold nanoparticles and whiskers at their tips.

2.3. Theory of Field Emission

Field emission of electrons from a surface of a condensed phase (usually a metal) into a secondary phase (usually vacuum) takes place under high electrostatic fields (0.3 – 0.6 V/Å). The phenomenon consists of the tunneling of electrons through a deformed

potential barrier at the surface [43, 61]. It is fundamentally different from thermionic emission or photoelectron emission, where only electrons with sufficient energy jump over the barrier and are ejected. A detailed energy band diagram of a field emission system is depicted in **Figure 2.8**.

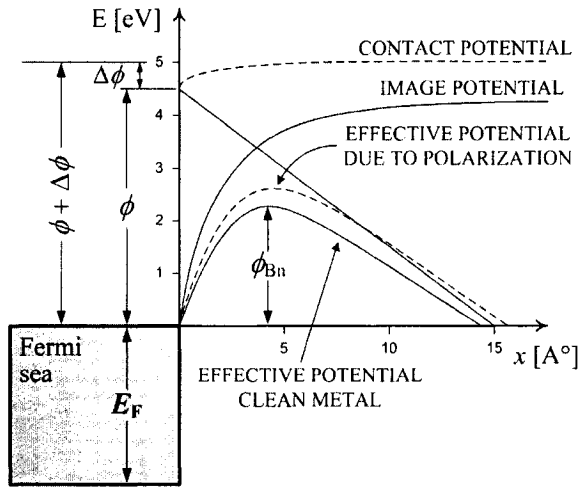

Figure 2.8 (*adapted from Gomer in* [43]). Potential-energy diagram for electrons at a metal surface in the presence of an applied field, with image potential included; dashed curves refer to the additional potential caused by gas adparticles.

In the above diagram, E_F denotes the Fermi level of metal, ϕ is the metallic work function, $\Delta\phi$ is the change in ϕ due to absorption or adsorption and is ϕ_{Bn} is the effective barrier height when the Schottky image force lowering is considered [62]. The emission current highly depends on the local electric field at the interface as well as the surface conditions which affect the potential barrier through which electrons tunnel. The relationship between the emission current density J and the local electric field E_{loc} is given by the Fowler and Nordheim (F-N) equation [63] :

$$J = a\frac{E_{loc}^{\ 2}}{t(y)^2\phi}\exp\left[-b\frac{\phi^{3/2}}{E_{loc}}v(y)\right], \tag{2.43}$$

where a and b are the universal F-N constants given by:

$a \equiv e^3/16\pi^2\hbar = 1.541434\times10^{-6}$ A·eV·V^{-2}, and

$b \equiv (4/3)(2m_0)^{1/2}/e\hbar = 6.830888\times10^{7}$ eV$^{-3/2}$·V·m^{-1},

with $\hbar = h/2\pi$, where $h = 4.13566733\times10^{-15}$ eV·s is the Plank's constant, e is the electronic charge, m_0 is the mass of free electron, ϕ is the metal workfunction, and the image force barrier lowering factor y is defined as

$$y = \frac{c\sqrt{E_{loc}}}{\phi}, \tag{2.44}$$

where $c \equiv (e^3/4\pi\varepsilon_0)^{1/2} = 3.794687\times10^{-4}$ eV·V$^{-1/2}$·cm$^{1/2}$. The generalized correction factors $v(y)$ and $t(y)$ are given by [63, 64]:

$$v(y) = \frac{1}{\sqrt{2}}\left[1+\left(1-y^2\right)^{\frac{1}{2}}\right]^{\frac{1}{2}}\cdot\left[E\left(k^2\right)-y^2\frac{K\left(k^2\right)}{1+\left(1-y^2\right)^{\frac{1}{2}}}\right], \tag{2.45}$$

and

$$t(y) = \frac{1}{3}(4s-v), \tag{2.46}$$

where

$$k^2 = \frac{2\left(1-y^2\right)^{\frac{1}{2}}}{\left[1+\left(1-y^2\right)^{\frac{1}{2}}\right]}, \tag{2.47}$$

and where $E\left(k^2\right)$ and $K\left(k^2\right)$ are the elliptic integrals given by [64]

$$E\left(k^2\right) = \int_0^{\pi/2}\sqrt{1-k^2\sin^2\theta}\,d\theta, \tag{2.48}$$

$$K\left(k^2\right)=\int_0^{\pi/2}\left(1-k^2\sin^2\theta\right)^{-1/2}d\theta\,, \tag{2.49}$$

and

$$s=v-\frac{1}{2}y\frac{dv}{dy}\,. \tag{2.50}$$

In experimental context, when the $I-V$ curves are measured and studied, (2.43) becomes

$$I=A_{\mathrm{FN}}a\frac{(\zeta V)^2}{t(y)^2\phi}\exp\left[-b\frac{\phi^{3/2}}{\zeta V}v(y)\right], \tag{2.51}$$

where A_{FN} is the effective emission area, and ζ is the field factor. The correction factors are also adjusted accordingly. Note that ζ could include the field enhancement factor β, defined earlier, as follows:

$$E_{\mathrm{loc}}=\beta E_{\mathrm{app}}=\zeta V\,. \tag{2.52}$$

To further simplify the study of the experimentally obtained $I-V$ curves, they are usually drawn in so called F-N coordinates, where $\ln(I/V^2)$ is plotted against $1/V$:

$$\ln\left(I/V^2\right)=B_{\mathrm{FN}}-\frac{S_{\mathrm{FN}}}{V}\,, \tag{2.53}$$

where the intersection with the $\ln(I/V^2)$ axis, B_{FN}, is given by

$$B_{\mathrm{FN}}=\ln\left(A_{\mathrm{FN}}a\frac{\zeta^2}{t(y)^2\phi}\right), \tag{2.54}$$

and the slope of the curves, S_{FN}, by

$$S_{\mathrm{FN}}=-b\frac{\phi^{3/2}}{\zeta}v(y)\,. \tag{2.55}$$

We neglect the small dependence of v on V.

For metals, empirical F-N plots given by (2.53) are often straight lines, because the dependence of B_{FN} and S_{FN} upon voltage, through the image force factor is minor. However, to be precise, the parameters derived from an experimental F-N plot are actually parameters associated with a tangent to the theoretical curve described by (2.51). Consequently, the linear approximation of (2.53) can be only employed for a small range of $1/V$ values.

2.3.1. Effect of Ambient Gas on the Field Emission Properties

a. Determination of the Changes in Workfunction

The metallic workfunction ϕ is known to be affected by the presence of gas. Upon adsorption of gas particles on the metal surface due to polarization forces, double layers are formed and change the charge distribution over the surface. A dipole moment P_i (in first approximation) can be associated with each adsorbed particle, henceforth referred to as adparticle. As a result, the adsorbed layer will contribute a term $\Delta\phi$ to the workfunction [43, 65] which may be written as:

$$\Delta\phi = -2\pi P_i N_s \theta_s , \tag{2.56}$$

where N_s is the maximum number of adsorption sites per unit area, and θ_s is the fraction of filled ones, and P_i is given by

$$P_i = \alpha_p E , \tag{2.57}$$

where α_p is the polarizability volume[1] with units of cm^3. The polarity of P_i is defined positive (negative) if the dipole is pointing away from (toward) the surface. In practice,

[1] Polarizability has the SI units of $C \cdot m^2 \cdot V^{-1} = A^2 \cdot s^4 \cdot kg^{-1}$ but is more often expressed as polarizability volume with units of cm^3 or in $Å^3 = 10^{-24}\ cm^3$.

the measured quantity of $\Delta\phi$ is often 1 – 2 eVs, even for physically adsorbed gases on clean metals. As a result, the apparent workfunction due to *monolayer* adsorption would be:

$$\phi_{\text{mono}} = \phi + \Delta\phi, \tag{2.58}$$

If the workfunction of the clean metal is known, then the changes in on adsorption can be determined by comparing the slopes of F-N curves. In these cases, the field factor ζ (or β) presumably remains constant and need not always be evaluated explicitly. According to (2.55) comparison of the slopes for clean and adsorbate covered emitters yields:

$$\phi_{ad} = \left(S_{FN-ad}/S_{FN-cl}\right)^{2/3}\left(v_{cl}/v_{ad}\right)^{2/3}\phi_{cl}, \tag{2.59}$$

where ϕ_{ad} and ϕ_{cl} are the average workfunctions with and without adsorbate and $S_{\text{FN-}ad}$ and $S_{\text{FN-}cl}$ are the corresponding slopes [43]. The factor $\left(v_{cl}/v_{ad}\right)^{2/3}$ is usually so close to unity that it can be neglected. As mentioned earlier, the use of equations (2.55) and (2.59) is strictly correct if the slopes are considered invariant within the studied range of field (applied voltage) and ϕ is assumed to be constant over the emitting region, which is seldom the case.

There is however, an additional effect that must be considered in using (2.59) for computing average workfunction changes upon adsorption. If such a calculation is to be valid, the relative emission anisotropy of the emitter tip before and after adsorption must remained unchanged, that is, the regions contributing most to emission of the clean tip must be still the ones whose changed workfunction is measured after adsorption. Fortunately, experiments have shown that this is generally the case, since contact-

potential (see **Figure 2.8**) anisotropies are usually insufficient to alter the relative positions of the various emission regions.

The errors inherent in the determination of average changes can be overcome by measuring workfunctions of individual regions of the emitter tip by photoemission spectroscopy. For instance Singh et al. [66] used the technique to characterize their β-phase W nanorods. In our particular case, because of the difficulties in measuring the workfunction of each nanowire, we assumed a constant value of ϕ_{Au} = 4.8 eV for adsorbate-free samples.

For heavy coverage, the workfunction decreases for neon, increases for argon, and remain constant for krypton and xenon, relative to the monolayer values as described by (2.58). In all cases however, the total emission is decreased because of changes in the pre-exponential term due to the reduction of the emission area and will be discussed in the next section. In the following we explain the governing mechanisms that affect the apparent work function due to *multilayer* adsorption.

The thickness of the adsorbed film is 20 – 30 Å at maximum coverage and exceeds the length of the potential barrier seen by the electrons near the Fermi level (**Figure 2.8**), even if the reduction in field strength by $1/\varepsilon_r$, where ε_r is the dielectric constant of the gas, is considered. Since electrons close to the Fermi level contribute most heavily to the field emission current, the barrier region of interest can be considered to be filled with gas atoms. It is known that only the first layer contains strong dipoles. As a result, the emission occurs through a shell of nonpolar dielectric. In this case, to simplify the problem, it can be assumed that emission occurs through a potential barrier modified in accord to monolayer conditions, but with the following considerations:

1. The field in the dielectric shell is reduced by a factor of $1/\varepsilon_r$.
2. In addition to the field strength itself, the image potential is reduced by $1/\varepsilon_r$ (see the derivation method of y discussed in detail at [43, 62]).
3. The potential of electrons in the dielectric is reduced by the average polarization energy.
4. Each gas atom represents a short range deep attractive potential for electrons because at small distances the nucleus is not screened completely, so that the barrier opacity is reduced by these potential 'holes'.

From the four phenomena mentioned above, the first two raise the apparent workfunction ($\Delta\phi_{\text{mult}} > 0$) and last two reduce it ($\Delta\phi_{\text{mult}} < 0$). In the case of neon which has a low dielectric constant for instance, the *hole* effect is predominant, in argon the opposite is the case and ϕ increases upon adsorption. In krypton and xenon, the effects more or less balance each other. The raise in the apparent work function can be treated as follows. In (2.43) instead of replacing E_{loc} by $E_{\text{loc}}/\varepsilon_r$, ϕ must be multiplied by $\varepsilon_r^{2/3}$. The modified image potential term is also given by

$$y = \frac{c\sqrt{E_{\text{vac}}}}{\varepsilon_r \phi}, \tag{2.60}$$

where E_{vac} is the field that would exist if there where no dielectric [67]. The correction function $v(y)$ should also be adjusted accordingly. The appropriate values of ϕ and v can therefore be found by iteration.

The polarization energy $\Delta\phi_{\text{pol}}$ usually imposes a small correction to the energy except at very close atom-electron distances and can be calculated as a lattice sum over the terms

$\frac{1}{2}\alpha_p E_{eff}^{\ 2}$ where α_p is the atomic polarizability, and E_{eff} is the effective field at an atom due to the polarizing electron.

It is assumed that the contact potential of the monolayer is not affected by subsequent adsorption, the hole effect problem will consist of finding the effect of an array of small potential wells on the expectation value of ϕ. The arguments require detailed quantum mechanical analysis and are outlined in [43] and [68]. A simplified general expression obtained by treating the situation as scattering problem is

$$\left|\Delta\phi_{\text{hole}}\right| = 2\pi n_h a_h \hbar^2 / m_e \,, \tag{2.61}$$

where n_h is the density of holes, a_h is the scattering length, and m_e is the effective electron mass. The workfunction change due to the hole effect can now be found by subtracting the corrected multilayer workfunction from that of the monolayer;

$$\Delta\phi_{hole} = \phi_{mono} - \phi_{multi} - \Delta\phi_{pol} \,. \tag{2.62}$$

Table 2.1 shows a summary of hole parameters for inert gases.

Table 2.1 (*after Gomer in* [43]). Summary of hole parameters for inert gases. $\Delta\phi_{\text{hole}}$ is the workfunction change due to the hole effect; a_h is the scattering length and r_0 is the hole radius.

Gas	$\Delta\phi_{\text{hole}}$ [eV]	a_h [Å]	r_0 [Å]
Neon	0.80	0.46	0.60
Argon	0.50	0.42	0.52
Krypton	0.89	1.23	1.00
Xenon	1.17	1.95	1.38

b. Changes in the Effective Emission Area

In addition to the changes in workfunction, adsorption causes large changes in the effective microscopic emitting area of a given region. In the case of electronegative adparticles emission may occur only from between adparticles. For electropositive adparticles, the opposite may be the case, that is, the particles act like windows in the barrier. Either case results a reduction in the microscopic emission area. According to (2.54), any change in the effective area A_{FN}, would be reflected in the intersection of F-N plots with the $\ln(I/V^2)$ axis (B_{FN}). In addition, the change in the workfunction due to polarization and given by (2.56), may produce a change in B_{FN}.

2.3.2. Schottky-Barrier Field-Enhanced Emission Mechanism

Theoretically, no measurable emission would occur from a perfectly smooth surface at fields less than 0.1 V/Å. Material and fabrication techniques have both been used to increase the emission by enhancing the electric field and reducing the barrier over which electrons can tunnel. There are two generally accepted mechanisms that enable achieving the required field strengths for FN emission: The geometrical field enhancement explained earlier and the Schottky barrier field enhancement created by a negative-electron-affinity (NEA) semiconductor. In the former approach, the field strength can be increased above 1000 times the average E_{app}, making it possible to obtain emission with an average E_{app} of 10^4 V·cm^{-1}.

The Schottky barrier field enhancement (SBFE) technique requires an *n-type* NEA semiconductor (usually diamond doped with an electron donor impurity such as nitrogen) [58, 67, 69-72]. **Figure 2.9** shows the energy band illustration of this mechanism. The

semiconductor forms a Schottky barrier with the metal. Therefore, the magnitude of the emission current density is limited by electrons tunneling through the metal-semiconductor Schottky diode and not by emission from the metal to the vacuum. Since in an NEA semiconductor the vacuum energy level lies below the minimum energy level in the conduction band, the tunneling electrons from the Schottky barrier are liberated into vacuum without any energy loss. However, because of the depletion region formed at the metal-semiconductor junction, the electric field across the junction is higher than that of a metal-vacuum interface, though reduced by a factor of ε_r (relative permittivity of the NEA material). In addition, the Schottky barrier height ϕ_{Bn}, is usually smaller than the metal work function. The emission current is therefore several orders of magnitude higher than from regular metal-vacuum interface. SBFE has been discussed in more details [69], and variations of this mechanism have been used to explain many experimental results [58, 60, 72-77].

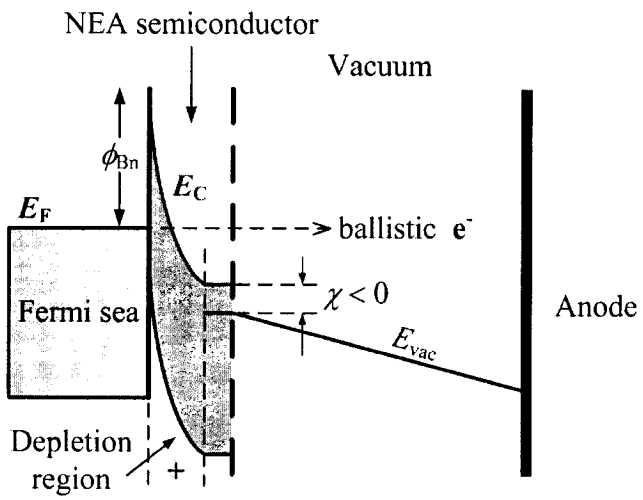

Figure 2.9. Energy band diagram of the Schottky barrier field enhanced emission mechanism. E_F is the Fermi level, ϕ_{Bn} is the Schottky barrier height, and E_C and χ are the minimum conduction band energy level and the electron affinity of the NEA material respectively. Note that the voltage drop across the depletion region is higher than that of vacuum.

A complex relationship that explains the emission current density based on semiconductor doping density N_d, barrier height and the potential drop across the semiconductor V, was derived using the WKB approximation and is given by [70]:

$$J = \frac{eN_d}{\pi h \varepsilon_r \varepsilon_0} \frac{1}{\mathrm{X}^2} \exp\left[-\left(\frac{\pi V}{h} \right) \sqrt{\frac{\varepsilon_r \varepsilon_0 m_e}{eN_d}} \Theta \right] \approx a_1 V^2 \exp\left[-\frac{b_1}{\sqrt{V}} \right] \text{ for } V >> \phi_{Bn}, \quad (2.63)$$

where

$$\Theta = D + \frac{\left(1 - D^2\right)}{2} \ln\left[\frac{(1-D)}{(1+D)} \right] \approx \frac{2D^3}{3} + \frac{2D^3}{15}, \quad (2.64)$$

$$\mathrm{X} = -D \ln\left[\frac{(1-D)}{(1+D)} \right] \approx 2D^2 + \frac{2D^4}{3}, \quad (2.65)$$

and

$$D^2 = \frac{\phi_{Bn}}{V}, \quad (2.66)$$

and where ε_0 is the vacuum permittivity, m_e is the effective electron mass in the semiconductor and h is planks constant. The electron emission increases as N_d increases and ε_r, m_e, and ϕ_{Bn} decrease.

Although the functional form of (2.63) is substantially different from (2.43), both functions will usually describe the data when the measured current from a cathode is plotted in F-N coordinates. Thus, we cannot easily distinguish between the two mechanisms on the basis of the emission parameters of the cathode. As with (2.43), accurate emission-current calculations using (2.63) are almost impossible because not enough of the parameters are known to sufficient accuracy [67]. Arrays of these cathodes emit current densities above 10 $A \cdot m^{-2}$ when potentials of 10 to 20 V are applied between

the metal substrate contacting the semiconductor and a metal gate structure spaced about 1 μm away [69, 77]. It is expected, however, that adsorption would have less effect on the SBFE emission current than that of the regular metal/vacuum interface, because the barrier which limits the current is not exposed.

Apparently, the SBFE emission can be combined with geometric field enhancement technique by sharpening the metal-semiconductor interface, to obtain further field enhancement.

In this work, instead of using (2.63), we propose using the following model to explain the SBFE emission mechanism from our AuNWs and estimate their geometrical field enhancement factor. Schottky barrier emission can be conveniently cast in a form similar to the conventional F-N equation of (2.51). This way of thinking was initially suggested by Lerner et al. [67], however, they did not consider the variation of the correction factors $t(y)$ and $v(y)$ and the ballistic (over-barrier) transport when $y > 1$.

In (2.43) both E_{loc} and y are reduced by a factor of $1/\varepsilon_r$, to account for the reduction of field strength in the semiconductor and b is replaced by

$$b_e = b\sqrt{m_e/m_0}\,, \tag{2.67}$$

where m_0 is the mass of free electron. The resulting expression for the SBFE current density can be written as:

$$J_{SBFE} = a\frac{\left(E_{\text{loc}}/\varepsilon_r\right)^2}{t\left(y/\varepsilon_r\right)^2\phi}\exp\left[-b\sqrt{m_e/m_0}\,\frac{\phi^{3/2}}{\left(E_{\text{loc}}/\varepsilon_r\right)}v\left(y/\varepsilon_r\right)\right], \tag{2.68}$$

where E_{loc} is the local field that would exist if there were no semiconductor (local field in the vacuum), and the rest of parameters and functions retain their definition.

Now, to compute the field enhancement factor of the emitting tips, for instance, the slope of the corresponding empirical F-N plot given by

$$S_{\mathrm{FN}} = \frac{\partial}{\partial(1/V)} \ln\left(J_{SBFE}/V^2\right), \tag{2.69}$$

can be solved self-consistently with (2.52) to find β (or ζ) and the local field strength at the tunneling barrier $E_{\mathrm{loc}}/\varepsilon_r$.

2.4. Theory of Field Ionization

Field ionization (FI) occurs when a valance electron of a gas atom or molecule (hereafter referred to as gas particle) having an ionization potential of U_I, tunnels through a potential barrier into a vacant energy state of the conduction band of a metal with a work function of ϕ [34, 43-45, 78, 79]. **Figure 2.10** shows the energy band illustration of FI of a hydrogen atom. FI of elements normally requires very high electric field strengths of the order of $E_i \sim 2 - 6$ V/Å, depending on the U_I of the residing gas particle [78, 80]. For instance helium atoms with the highest ionization energy among substances (U_I = 24.5874 eV) requires about 6 V/Å, whereas organic molecules with low ionization energies (9 – 12 eV) can be field ionized at considerably lower field strengths (0.1 V/Å or even less) [81].

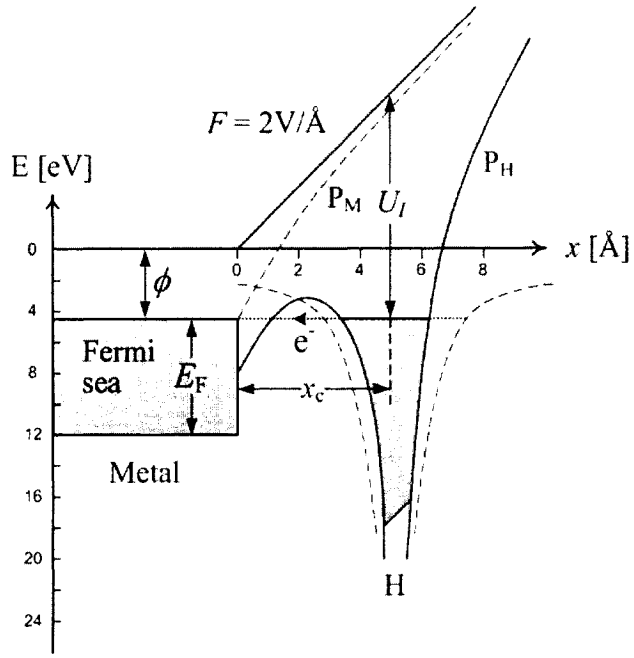

Figure 2.10 (*adapted from Gomer in* [43]). Potential energy diagram for a 1*s* electron of a hydrogen atom in a field of 2V/Å, at a distance of 5.5Å from a tungsten surface. E_F is the Fermi level; U_I, ionization potential, P_M, atom potential; P_W, superposition of applied and pseudo image potential; x_c, critical distance. Dashed lines show the potential in the absence of an external field.

Such fields are achievable only at the vicinity of very sharp tips or protrusions. For instance to produce ionization at an applied voltage of 10 kV, it is necessary to make tips with end radii of $r_t = 50 - 100$ nm.

The process of FI can be described to occur in three steps and is usually illustrated by a potential diagram of the valance electrons. First, the gas atoms which are polarized near the tip, are attracted and accelerated to the surface by the field gradient along the radial direction. The second step is the energy loss and the resulting deceleration of atoms by bouncing on the surface. In the third step, the gas atoms attached to the tip are field ionized by quantum mechanical tunneling of electrons from the atoms through the narrow potential barrier into the metal tip, when the potential energy of the electron approaches the Fermi level of the metal. The resulting ions are then repelled from the surface.

The first observations of field ionization were made by Müller, when he admitted hydrogen at low pressure (10^{-3} torr) to a field-emission tube and instead of a negative bias, applied a high positive voltage to the tip. A highly resolved, though faint, image appeared on the screen which he attributed to protons desorbed from the tip [43]. This technique is known as Field Ion Microscopy (FIM), and if combined with a mass spectrometer, provides the Atom probe analysis method. Atom probe FIM has the highest analytical spatial resolution of any microscope that enables fundamental determination of the chemistry of a nanoscale region by simply counting the number of atoms of each type in a given volume. **Figure 2.11** illustrates the principle of an atom probe field ion microscope. For further details see [34].

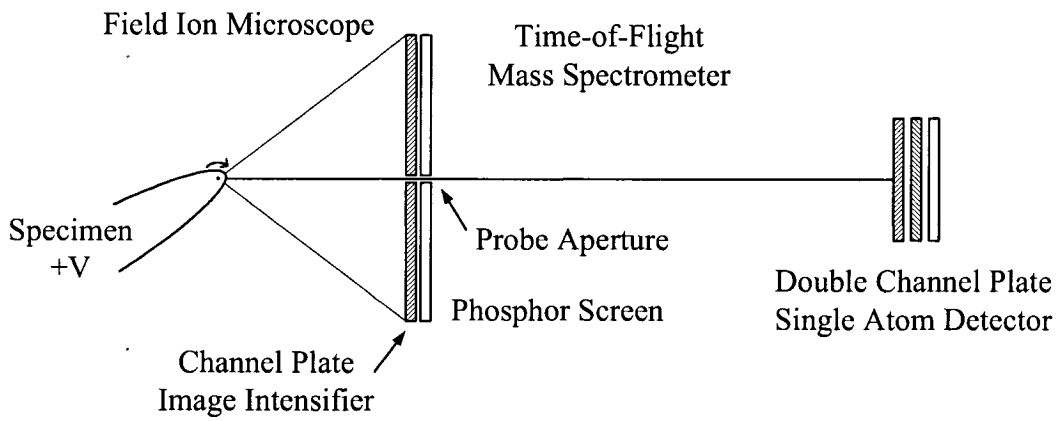

Figure 2.11 (*adapted from Miller et al. in* [34]). Principle of the atom probe; the FIM is shown on the left and the time-of-flight mass spectrometer on the right. The mass spectrometer consists of a drift tube at the end of which is a detector that has single-atom sensitivity. A small probe aperture in the microchannel plate and phosphor screen assembly defines the area of the specimen surface that will be analyzed in the mass spectrometer.

As U_I is specific to any gas particle, the resulted tunneling current can be used in a certain manner to fingerprint the unknown gas type. In addition to detecting the ionization breakdown voltage of the gas to be identified, the GIS proposed in this

research can be tailored to provide FI of gas species at sub-10 V applied biases (three orders of magnitude smaller than typical voltages used in FIMs). In addition to geometrical field enhancement, further lowering of the FI voltage is achievable by coating the metallic tip with a thin layer of semiconductor. In the following we explain the basic FI formalism on metals first and then discuss the required modifications for semiconductors.

2.4.1. Basic Field Ionization Formalism

Even in the presence of a positive (ionization) field E_i, FI cannot occur when the gas particle is at a distance from the surface less than the critical distance given by

$$x_c \cong (U_I - \phi)/E_i , \tag{2.70}$$

because the electron energy level in the particle would lie below the metallic Fermi level, where there are no available states for tunneling to take place (see **Figure 2.10**).

Despite the relative simplicity of FI, the mechanism of current generation can be a complex function of field and temperature, and is best discussed in limiting cases. Müller and Bahadur [82] have calculated tunneling probabilities assuming the gas atom velocity to be directly related to the potential energy arising from polarization

$$U_P = -\frac{1}{2}\alpha_p E^2 . \tag{2.71}$$

Also recently, Liu and Orloff [79] have proposed an analytical model of a gas phase field ionization source. In practice it is found that ionization only occurs when the gas has become thermally accommodated to the temperature of the tip, and it is therefore this temperature that controls the gas atom velocity and not the polarization energy U_P. A characteristic time for ionization can be defined as

$$\tau = \left(v_e D\right)^{-1}. \tag{2.72}$$

where v_e is the orbital frequency of the tunneling electron in the gas particle and D is the tunneling probability given by

$$D = \exp\left[-6.8\times10^{-7}\left(U_I - 7.6\times10^{-4}E^{1/2}\right)^{1/2} x_c\right], \tag{2.73}$$

where U_I and E are given in eV and V·cm^{-1} respectively [43, 78].

Depending on the field strength, the field-ion $I - V$ characteristic consists of three distinctive regimes: In the *field-limited* regime where the field is relatively low, the total rate of ionization is small compared to the rate of arrival. The current is proportional to the equilibrium number of particles near the tip which exceeds the zero-field value due to the polarization effect in the high-field region. The ion current in this case is approximately given by

$$I_{FL} = 2\pi r_t^2 e x_c c_t \tau^{-1}, \tag{2.74}$$

where r_t is the metal tip curvature, e is the electron charge, x_c and τ were defined previously, and c_t is the equilibrium gas concentration near the tip given by

$$c_t = c_g\sqrt{T_g/T_t}\exp\left(|U_P|/k_B T_g\right), \tag{2.75}$$

where c_g is the concentration far from the ionization zone, T_g and T_t are the gas and tip temperatures respectively, k_B is the Boltzmann constant, and U_P is the polarization energy defined previously. The ion current in the field-limited regime rises steeply with the electric field [43, 79, 82, 83].

At sufficiently high fields, nearly all particles approaching the tip become ionized before reaching it. The current is therefore limited by the gas supply into the ionization zone and rises mildly with the field [79, 83]. The *supply-limited* ionization current can be written as:

$$I_{SL} \approx 4\pi r_t^2 eY, \tag{2.76}$$

where Y is the supply function, or the number of particles impinging on a unit surface per unit time [43, 78, 79, 82]. It also exceeds the gas kinetic value due to the attraction of particles by polarization forces. After some algebraic simplification it is given by:

$$Y = \frac{P}{k_B T_g}\sqrt{\frac{\pi|U_P|}{2\pi m_g}}, \tag{2.77}$$

in which P is the gas pressure and m_g is the atomic (molecular) weight of the gas particle. For example, Figure **2.12** shows a comparison of the calculated $I - V$ characteristic for a H_2 (gas) – Ir (tip) gas phase field ionization source at T_g = 300° K, $P = 10^{-3}$ Torr, and r_t = 0.1 μm with the experimental data by Orloff and Swanson [83]. The experimental data have been recalibrated assuming that the total current is emitted within a half aperture angle of 20° – 30°, corresponding to a solid angle ~0.5 sr. The experimental data were taken using a detector with a 9 msr solid angle.

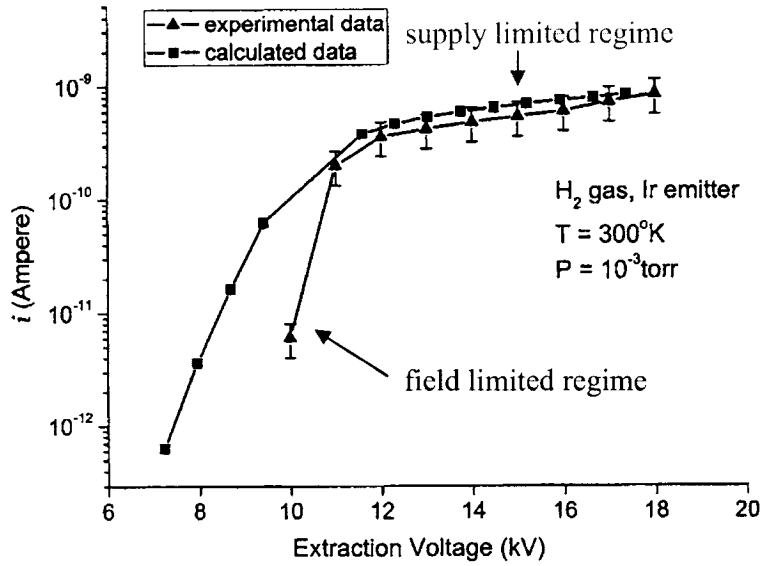

Figure 2.12 (*adapted from Liu and Orloff in* [79]). Comparison of the experimental and calculated $I - V$ characteristic of H_2 – Ir gas phase field ionization source at 300 °K. Experimental data were scaled to take into account the small solid angle of the detector.

At intermediate fields between these extremes, the situation becomes more complicated and the ion current must be calculated from detailed kinetic considerations [43].

Obviously, the field-limited current depends strongly on U_I through both the tunneling probability D and the critical distance x_c, and also α_p through U_P. The supply limited current on the other hand, does not depend on U_I though it is proportional to $(\alpha_p/m_g)^{1/2}$, but such a linear dependency is weak compared to the strong exponential dependency of the field-limited current upon U_I.

Therefore, much alike the atom probe which detects the mass-to-charge ratio of the ions, the abovementioned dependence of I_{FL} on U_I can be employed to fingerprint different gas species, by comparing the field-ion currents of different gases at a particular

voltage. However, note that we presume the particles are singly ionized, as the next ionization levels usually require much higher energies.

2.4.2. Field Ionization Above Semiconductor Surfaces

In the case of semiconductors, the basic FI theory outlined above requires some modification. Field penetration into the semiconductor, may cause significant upward band bending and make the near surface region to become *p-type* degenerate [34, 84-87]. The characteristic length of the electric field screening is given by the Debye length as

$$\delta = \sqrt{\frac{\varepsilon_r \varepsilon_0 k_B}{2 n_i e^2}}, \tag{2.78}$$

where n_i is the intrinsic carrier concentration in the semiconductor and the rest of the parameters are already defined. Field penetration depth λ_S, as well as band bending potential ϕ_S can be both calculated as a function of δ [88]. Equation (2.78) though adequate at low fields, gives incorrect value for the decay of high fields (~0.1 V/Å) at a semiconductor surface. The applied field causes significant band bending at the surface of the semiconductor, as indicated by the surface potential in **Figure 2.13** and results in a high density of carriers in the near-surface regions. The semiconductor surface can hence be regarded as semi-metallic in character and most of the applied field decays within 1 nm of the surface.

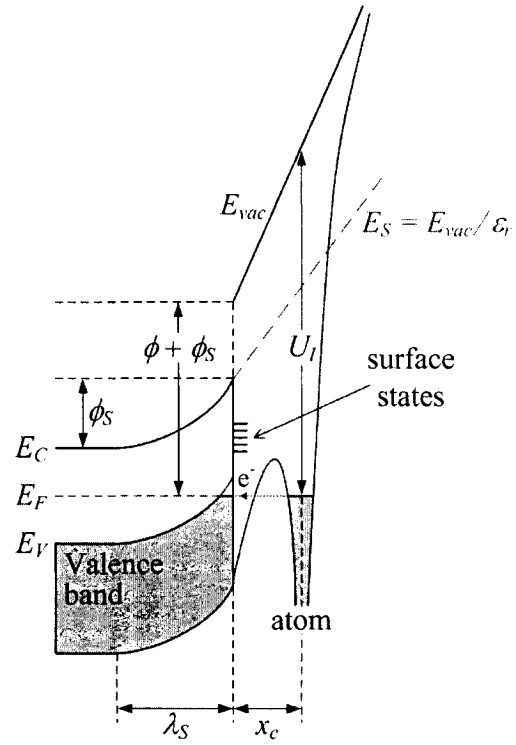

Figure 2.13. Field ionization of an atom at the vicinity of a semiconductor under a positive applied field. The semiconductor work function at the surface ϕ, increases by the amount of band bending ϕ_S. λ_S is the field penetration depth and x_c is the critical distance.

Band bending in the semiconductor can be computed using the Poisson equation as

$$\frac{d^2V}{dx^2} = -\frac{\rho_c(x)}{\varepsilon_r \varepsilon_0}, \tag{2.79}$$

where $\rho_c(x)$ is the charge density for band bending under a positive applied field and is equal to the density of holes p:

$$\rho_c(x) = p = N_v \frac{2}{\sqrt{\pi}} f_{1/2}\left(\frac{E_V - E_F}{k_B T}\right), \tag{2.80}$$

where N_v is the density of states in the valence band, E_V and E_F are the maximum energy level of the valence band and the Fermi level respectively (see) and $f_{1/2}$ is the half-order Fermi integral given by [62]:

$$f_{1/2}(\eta) = \int_0^\infty \frac{\sqrt{y}dy}{1+\exp(y-\eta)}, \tag{2.81}$$

For simple hemispherical geometries similar to field ion tips, Tsong [84] showed that in high fields (E_{vac} ~ 1.5 V/Å) band bending results are similar to planar cases, first calculated by Seiwatz and Green [89] , as long as the radius of curvature r_t is not much less than 200 Å. The field penetration depth λ_S, under such high fields is also insensitive to the doping of impurities within the limit that the semiconductor is nondegenerate. For intrinsic silicon for instance, an internal field of E_S = 0.1 V/Å (vacuum field of E_{vac} = 1.2 V/Å) gives a band bending of ϕ_S = 1.1 eV, that is, a heavily inverted surface.

In the presence of surface states, band bending occurs even if there is no applied field, typically generating a *p-type* surface [34]. With an applied field, space charge is formed by charging of these states and reduces the band bending in the bulk, according to (2.79) [85].

As shown in Figure **2.13**, FI of a gas atom takes place by tunneling electron into the empty states of the valence band. Due to the inversion of the surface, there are empty valence states above E_F into which tunneling may occur. Even if due to presence of surface states, there is no inversion, tunneling may happen into the surface states above E_F. Also the effective work function at the surface increases by the amount of band bending ϕ_S. The critical distance is given by

$$x_c \cong \left(U_I - (\phi + \phi_S)\right)/E_i, \tag{2.82}$$

where according to [87] the expression for upward electron energy band bending ϕ_S is

$$\phi_S = \frac{E_{vac}}{\varepsilon_r}\lambda_S, \tag{2.83}$$

Various authors have measured E_i values considerably lower than the equivalent values for metallic counterparts [86, 87, 90]. At a constant applied field, the resulting x_c is usually smaller compared to the case of metal anodes. This would imply a higher tunneling probability and therefore a higher FI current.

Chapter 3

Synthesis and Characterization of Nanowires

Nanowires and nanorods have gained considerable attention because of their potential uses in both mesoscopic research and in the development of nanodevices [91]. In terms of definition, nanowires have a higher aspect ratio compared to nanorods, for instance [92] defines nanorods as nanostructures with aspect ratios of 2 – 20 and nanowires with aspect ratios higher than 20. The devices fabricated in this research, involve arrays of vertically-aligned, self-standing nanowires as the building blocks.

In terms of fabrication technology, nanowires can be divided into two main categories: (1) nanowires of the first type are explicitly FETs (NWFETs), and they resemble the group of narrow channel SOI MOSFETs [93]. Unlike planar SOI MOSFETs, lithographically defined channel widths (e.g. Si body) are comparable to the active layer thickness, so the gate could be wrapped around the channel to realize a gate-all-around (GAA) structure. Multi-gate or gate-all-around FETs provide much better gate control compared to planar MOSFETs [94]. Therefore at the ultimate scaling limits, where the gate length could be shorter than 10 nm, the wire thickness has to be shrunk down to the sub–10 nm regime in order to maintain good electrostatic integrity [95]. To achieve this, very high resolution lithography is required. It should be noted that the minimum channel length of the NWFETs defined by lithography is almost equal to the thickness of the active overlay. Also the mentioned technique is only capable of fabricating NWFETs of standard semiconductors processes such as SOI, Ge or GaAs/AlGaAs. (2) In addition to lithographic techniques which produce single wires, experimental groups have been

trying to fabricate nanowires by chemical methods. Some of which include CVD [96], sol-gel [97], and thermal decomposition [98]. These methods are capable of producing a bunch of disordered nanowires. However in our work, a highly ordered self-standing array of vertical nanowires is required. In this case we will use the general template based method to force the nanowiers to grow vertically.

3.1. The General Template-Assisted Method

The template based method involves the synthesis of a desired material within the pores of nanoporous template such as anodic alumina or track-etched polymer membranes [41]. Since the pores within these membranes are cylindrical and uniform in diameter, monodisperse nanowires of the desired material can be obtained. The template based process is a very general approach in the fabrication of nanotubes and fibrils composed of a variety of materials including metals, semiconductors, etc. The usefulness of this technique is three fold: First, it is extremely general in terms of the types of materials that can be prepared. Second, depending on the pore wall and material, both tubular and fibrillar nanostructures can be fabricated, and finally these nanostructures can be mounted on various substrates for a variety of applications. To date, most of the work in template synthesis has entailed the use of two types of nanoporous membranes, a) track-etched polymeric membranes and b) porous alumina membranes:

a) Track-etched

Membranes prepared by this method have filtration applications. A non-porous sheet of desired material such as polycarbonate with thicknesses ranging from 6 – 20 μm, are

bombarded with neutrons to create damage tracks in the material and then chemically etched the tracks into pores. The resulting membranes contain randomly distributed holes uniform in diameter as small as 10 nm, with a density of 10^9 pores/cm^2 [99]. An SEM micrograph of a porous polycarbonate membrane with pore diameter of 1 μm is presented in Figure **3.1a**. Due to the nature of the production process, the angle of the pores with respect to surface normal can be as large as 34°. Therefore depending on the pore size and density, not only the nanowires grown through these pores are not quite vertically aligned, but also there might be intersections within the membrane.

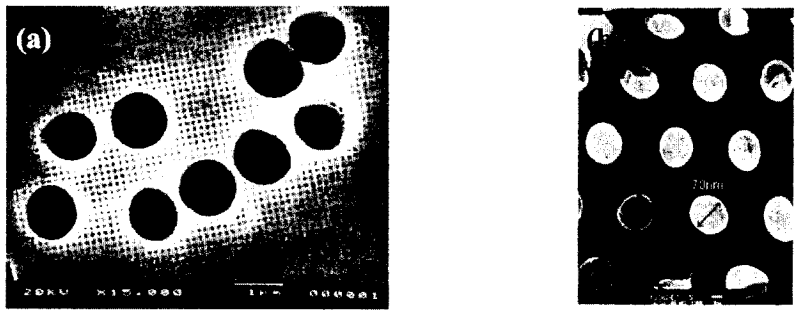

Figure 3.1. a) SEM micrograph of the surface of a polycarbonate membrane, b) TEM micrograph of a microtomed section of a PAA membrane [41].

b) Porous alumina

Porous alumina (Al_2O_3) membranes are made by anodization of aluminum in an acidic solution. They are usually referred to as Porous Anodic Alumina (PAA) or Anodized Aluminum Oxide (AAO) in the literature. The pores are uniform in diameter and arranged in a hexagonal array. But unlike the track-etch membranes, the pores are almost vertical and parallel and uniformly distributed at the surface. A TEM image of a thin PAA is shown in **Figure 3.1b**. Commercial PAAs are available with pore diameters as

small as 20nm. Usually the porosity is reported in lieu of pore density, ranging from 20% to 50% [100, 101]. Membranes with higher porosity would allow a greater number of nanowires to be fabricated per unit area of the membrane.

There are there main concerns that need to be taken care of during any template based growth process, (1) the precursor solution used to prepare the material must wet the pore walls; (2) the deposition reaction must not take place too fast to cover the pores and avoid tubule/fiber growth; and (3) the host membrane must be stable thermally and chemically.

There are a variety of chemical strategies that can be used to employ template based nanowire synthesis using PAAs and polymeric membranes [41]. Among them, the electrochemical deposition technique owing to its simplicity, low temperature deposition process and low cost [36, 40, 41, 101-111], is the most suitable for our case. Besides, it can be used to prepare both metallic (Au, Ag, Ni, Cu and Co) [109] and semiconducting (TiO_2, ZnO and WO_3) [41, 102, 107] nanowires. Electrochemical deposition of a material within the nanopores is accomplished by coating one side of the membrane with a metal film. The metal is either ion-sputtered or thermally evaporated on the membrane surface and serves as the cathode in electroplating. The length or aspect ratio (length to diameter) of the wires can be controlled by the amount of material electrochemically deposited into the pores.

3.2. Electrochemical Deposition

Electrochemical deposition of metals in general, entails the reduction of the metallic salt on the cathode. A metallic salt, when dissolved in water, dissociates to form positive ions. The solution that contains these charged ions is referred to as an electrolyte or a plating solution. By passing a sufficient amount of current through this electrolyte, one can reduce the metal ions to form the solid metal. The above process, which has been most commonly used to deposit coatings, is referred to as electroplating or electrochemical deposition. It can also be used to fabricate both metallic and semiconductor nanowires. In this research however, electrodeposition is solely utilized to grow gold nanowires (AuNWs) within the nanopores of PAA membranes as the templates.

Electrodeposition is usually carried out in a standard three electrode electrochemical cell that contains a *working electrode* (the PAA template) where reduction takes place, a *reference electrode* (saturated Ag/AgCl), and a *counter-* or *auxiliary electrode* (noble metal such as platinum) [112, 113]. We employed the galvanostatic transient method where the current between the working electrode and the counter electrode, I, is held constant with a current source (galvanostat) and the potential between the test electrode and the reference electrode, V, is measured during the deposition process. The potential is the dependent variable, which is recorded. **Figure 3.2** shows an illustration of an electrochemical cell configured for galvanostatic measurement.

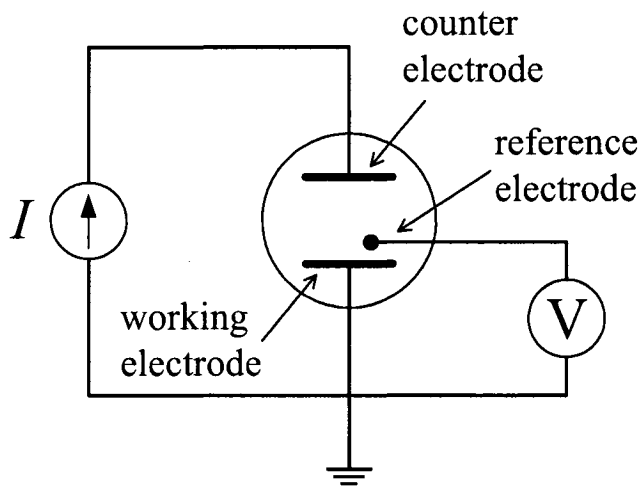

Figure 3.2. Schematic diagram of apparatus for galvanostatic measurement; *I* is the constant current source and *V* is the potential-time recording instrument.

According to the Helmhotlz model [17, 112], the interface of the metal electrode and the electroplating solution consists of two equal and oppositely charged layers, one on the metal (q_M) and the other in the solution (q_S). This pair of charged layers, called the 'double layer', is equivalent to a parallel-plate capacitor with a potential independent capacitance (C_{dl}).

The input signal and the response to it are compared in **Figure 3.3a** and **Figure 3.3b**. The response function $V_i = f(t)$ shows that a certain time is necessary to reach a potential V_i when the electrode reaction begins at the measurable rate. The duration of this time can be estimated by considering a simplified equivalent circuit to the single-electrode reaction (**Figure 3.3c**). When a constant current is applied to the system, the current is used for a) charging the double-layer capacitance C_{dl} up to the potential at which the electrode reaction can proceed with a measurable rate, and b) electrode reaction (charge transfer). The total galvanostatic current density J_g is thus given by

$$J_g = J_{dl} + J_{ct}, \tag{3.1}$$

where J_{dl} denotes the capacitive current and J_{ct} denotes the Faradic (charge transfer) current. The first process after applying current to the system, involves charging C_{dl}, up to V_i when the electrode reaction begins at a measurable rate. In accord to the model of **Figure 3.3c**, the instantaneous capacitive charging current is given by

$$J_{dl} = J_o \exp(-t/R_{ct}C_{dl}), \tag{3.2}$$

where J_0 is the input current density. **Figure 3.3d** shows the charging current versus time. The time necessary to charge C_{dl} to almost 99.0 % of the imposed voltage is therefore given by:

$$t_{V=0.99V_i} = 4.6R_{ct}C_{dl}. \tag{3.3}$$

Note that in the galvanostatic transient method, the charging time ($t_{V=0.99Vi}$), is of the order of milliseconds. In addition, from a series of measurements of V_i for a set of J (or the deposition current I) values, one can construct the current-voltage relationship for an electrochemical process.

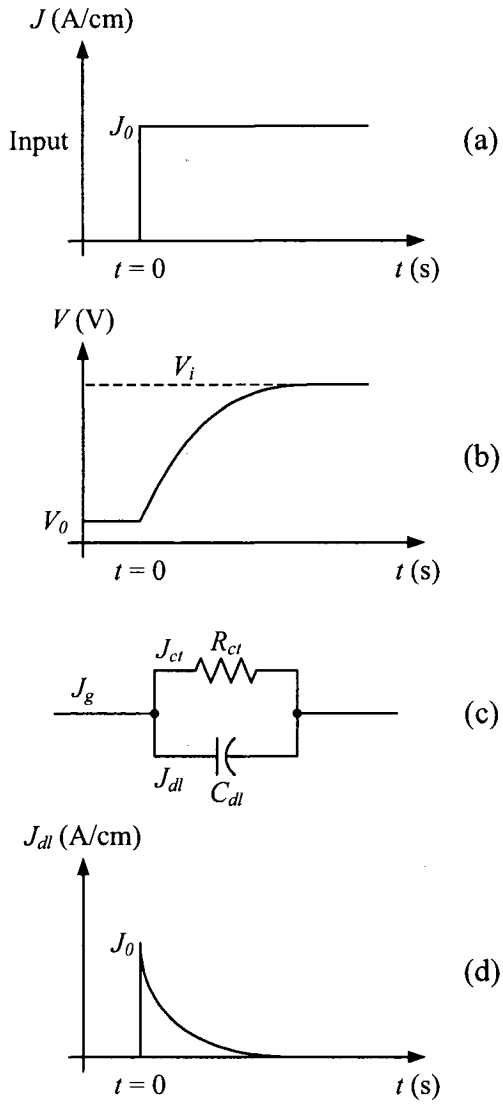

Figure 3.3. a) Input signal as applied to the working electrode, c) Simplified equivalent circuit for single-electrode reaction; C_{dl} is the double-layer capacitance at the working electrode (Helmholtz bilayer model) and R_{ct} is the charge-transfer resistance; c) Variation of potential of the working electrode, V, with time during galvanostatic deposition; E_i is potential of the working electrode at beginning of electrolysis at constant current density J, d) Capacitive charging current versus time

In the template based technique particularly, the PAA which serves as the working electrode must be conducting at the side where nanowires are supposed to nucleate and grow. Therefore a thin (100 nm) layer of a noble metal such as gold or silver is sputtered or thermally evaporated on to one side of the PAA. The PAA is then configured as the cathode, where metallic ions are reduced by acquiring the supplied electrons. The reaction is generally represented by

$$M^{n+} + ne^- \rightarrow M, \tag{3.4}$$

where M denotes some metal of n valency. For instance a gold cation (Au^{3+}) requires three electrons to be reduced into its metallic form:

$$Au^{3+} + 3e^- \rightarrow Au. \tag{3.5}$$

In order to find out the quantity of the deposited metal, we start by calculating the total cathodic charge Q consumed at the working electrode (cathode):

$$Q = emnN_A, \tag{3.6}$$

where e is the electronic charge, m is the number of gram moles of the deposited metal, n is the number of electrons taking part in the reduction, and $N_A = 6.02\times10^{23}$ mol^{-1} is Avogadro's constant. The number of mole grams of the metal reduced by a charge of Q is therefore given by:

$$m = \frac{Q}{nF}, \tag{3.7}$$

where F is Faraday's constant given by $F = eN_A = 96485$ $C\cdot mol^{-1}$.

If the deposition is carried out for t_{dep} seconds, the total charge used in the deposition can be given by:

$$Q = \int_0^{t_{dep}} Idt, \tag{3.8}$$

where I is the deposition current which varies in general. However, if the deposition is done galvanostatically, with a constant I during the process, (3.8) is then reduced to the product $I\cdot t_{dep}$. The weight of the deposited metal can be calculated as

$$w = m\cdot M_w = \frac{M_w}{nF}\int_0^{t_{dep}} Idt, \tag{3.9}$$

where M_w is the atomic weight of the metal in grams. Consequently, the thickness of the deposit d_{dep} is given by:

$$d_{dep} = \frac{w}{A_{dep}\rho_V} = \frac{M_w}{nFA_{dep}\rho_V}\int_0^{t_{dep}} Idt, \tag{3.10}$$

where A_{dep} is the deposit area in cm, and ρ_V is the density of the metal in gram·cm^{-1}.

The nanowires can be electrodeposited into the nanopores of the PAA starting from the bottom of the pore where the metal coating exists, until the nanowires protrude up to the surface, at maximum. The length of the nanowires l can be simply estimated if the porosity of the PAA template p_{PAA} is known:

$$l = d_{dep} / p_{PAA}, \tag{3.11}$$

Equation (3.11) is valid if it is assumed that the electrochemical growth process takes place only within the pores. However, if the template is kept suspended inside the electrolyte, the deposition normally takes place bilaterally, that is both through the pores and at the bottom side.

In this work we used commercially available PAAs from Whatman Inc. known as Anopore® (Anodisc) inorganic membranes [100]. **Figure 3.4** shows a photograph of a variety Anodisc PAAs and **Table 3.1** lists the specifications of the particular type we have used (Anodisc 25). These membranes have two well defined sides: the bottom side is formed by interconnected pores with a nominal diameter of 20 nm, corresponding to the pore size claimed by the company, and a thickness of approximately 2 μm. The top side consists of an alumina support layer, formed by unconnected cylindrical pores of 180 nm mean diameter, with a pore density of 10^9 pores per cm^2, and a thickness of about 58 μm. The bottom side is usually used as a filter, whereas the support layer is suitable as a

template for nanowire growth [101]. The membranes are peripherally bonded to an annular polypropylene ring for ease of handling.

Figure 3.4. Whatman PAA templates with the holding ring.

Table 3.1. Specifications of a Whatman PAA membrane (Anodisc 25)

Average membrane thickness	60 μm
Membrane Diameter	21 mm
Support Ring Material	Polypropylene
Construction Process	Thermal weld
Protein Adsorption	Low
Burst Strength	6 – 110 psi
Maximum Service Temperature	400°C
Porosity	25 – 50 %
Refractive Index	1.6

The dissimilarity of pore structure at the top and the bottom sides of the membrane is clear in the cross-sectional SEM micrograph of **Figure 3.5**. Because the pores are perpendicular to the PAA surface, the embedded nanostructures will be highly ordered and vertically aligned.

Figure 3.5. SEM micrograph of the cross section of an Anodisc 25 PAA membrane showing the different pore structure at the top and the bottom (branched) sides.

Depending on which side of the Anodisc PAA is sputter coated and used as the working electrode in the electroplating process, nanostructures with deferent geometries will be created. Later in sections 3.2.2 and 3.2.3 we will demonstrate a variety of nanowires we have grown from both sides of Anodisc PAA templates.

3.2.1. General Synthesis Steps

The PAA was mounted on a custom designed fixture as shown in **Figure 3.6**. The fixture covered the holding ring and one side of the PAA, while exposed the other face (a diameter of 1.5 cm or deposition area of A_{dep} = 1.77 cm^2). The fixture was then installed in a DC magnetron sputtering machine, where the exposed face was sputter-coated with a 100 nm thick layer of Ag or Au. The other side was untouched so that it could be exposed to the electroplating solution. **Figure 3.7** shows an SEM micrograph of the coated side. It is clear that the pores are not completely covered, as the sputtered metal tends to accumulate on the pore edges.

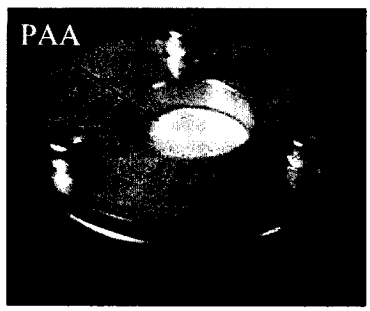

Figure 3.6. Custom-made fixture used to sputter-coat one side of the PAA template.

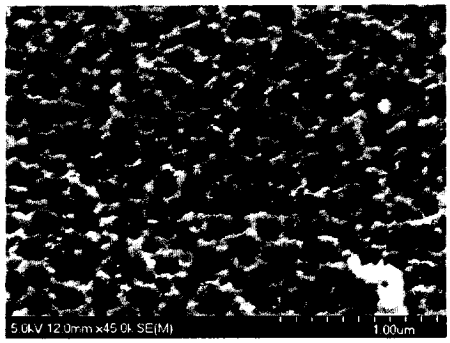

Figure 3.7. Bottom side of an Anodisc membrane sputter-coated with Ag (100 nm).

Electroplating of the AuNWs was performed in a custom-made cell based on earlier works [36, 104]. Orotemp 24T cyanide based gold solution was used as the electrolyte. It must be noted that the electrodeposition takes place bilaterally, that is both through the pores and at the exterior of the PAA membrane. Hence, the backing metal film becomes thicker during the process. Because the sputtered metal cannot seal the pores completely, the conductive part exposed to the plating solution will be a circle-like shape. When the electrochemical deposition is carried out under this condition, tubular structures will grow inside the pores by the direction of the sputtered metal circle as shown at the left of **Figure 3.8**. But as shown at the right of this figure, eventually the nanotubes will seal themselves after several hours of deposition.

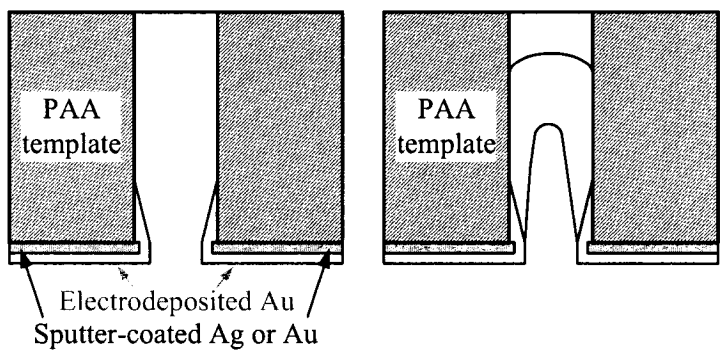

Figure 3.8. The process of electrochemical replication of the pores; left: Initial growth stage when the nanostructures are tubular; right: the nanostructures eventually seal themselves and form fibrillar wires.

Figure 3.9 shows the variation of working electrode potential versus the reference electrode (saturated Ag/AgCl) (V), with time (t), during galvanostatic electrodeposition of AuNWs. In the inset, the same curve is plotted in a semi-logarithmic scale (V vs. log(t)). The deposition was carried out under a current of I = 1mA ($J = 1/A_{dep}$ = 0.3 mA·cm^{-2}) for t = 24 hours. By substituting the deposition parameters ($Q = I \cdot t$ = 86.4 C, A_{dep} = 1.77 cm^2), and the atomic weight and density of gold (M_{Au} = 197 gr, D_{Au} = 19.3 gr·cm^{-3}) into equ. we estimated the thickness of the deposited gold film as $d_{dep} \approx 17$ μm. For the case of deposition inside the PAA pores, if an average porosity of p_{PAA} = 37.5% is assumed (see **Table 3.2**), then according to eqn. the expected length of the AuNWs would be about $l_{AuNW} = 17/0.375 \approx 45.3$ μm.

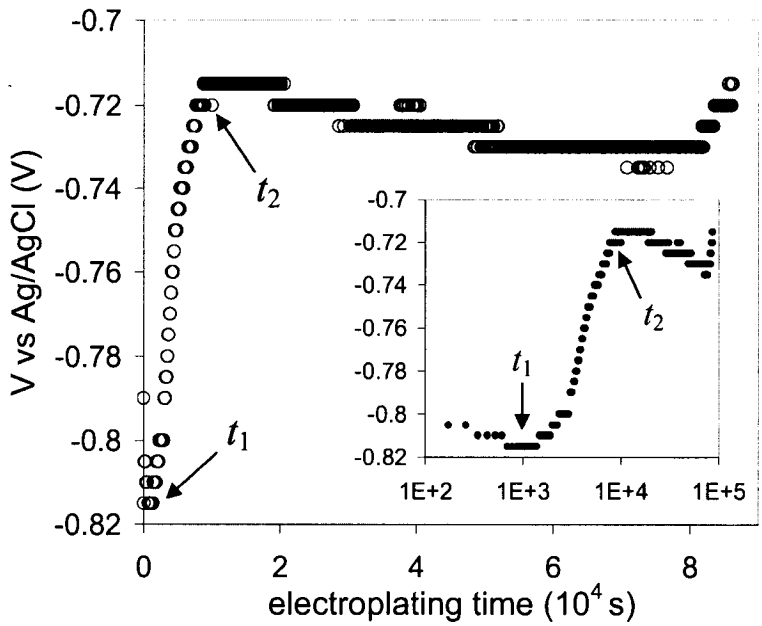

Figure 3.9. Variation of potential of the working electrode (PAA) versus the reference electrode (Ag/AgCl), V, with deposition time during galvanostatic electrolysis. t_1 denotes the start of nucleation and t_2 denotes the time when the pores are completely plugged and nanowires start to grow.

As shown in Fig. for $t_1 < t < t_2$, the reaction potential V (absolute value) decreases with time. Apparently, t_1 and t_2 are several orders of magnitude higher that the time required for settling of the reaction voltage indicated by (3.3). Therefore, the variation of $|V|$ is explained based on the change in the concentration gradient of Au^{3+} in the solution due to diffusion [114].$|V|$ drops as the ion concentration increases near the working electrode. After t_2, $|V|$ remains nearly stable through out the deposition. It slightly increases because of the increase in R_{ct} due to consumption of Au^{3+} cations.

The embedding PAA templates were removed from the electrochemical cell and attached from the sputter-coated side on a silicon substrate using diluted conductive paste. The silicon wafer was initially coated with a layer of Ti (5nm) and Ag (100nm) to provide an ohmic contact to the AuNW film. Note that the Ti coating acts as an adhesive layer. Extreme care should be taken at the bonding stage to make sure there is no trapped air bubbles between the silicon wafer and the AuNW film which cause the film to wrinkle. The structure was then immersed into a 2M NaOH solution to selectively dissolve the template, leaving the AuNWs. A snapshot of the AuNW film attached to the silicon substrate is shown in **Figure 3.10**. SEM micrographs of the initial stages of growth from the top and bottom sides are represented in **Figure 3.11**. The transformation of nanostructures from tubular to fibrillar is clearly seen in **Figure 3.11a**. Nanowires grown from the bottom side of the PAA, are formed with branched stems at their 1 – 2 μm long roots. They follow the particular pore structure of the template as mentioned earlier (**Figure 3.11b**).

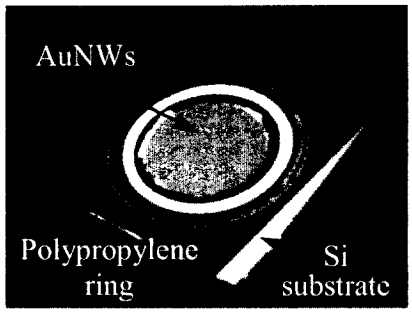

Figure 3.10. Snapshot of the AuNW film attached to an Ag/Ti coated Si substrate.

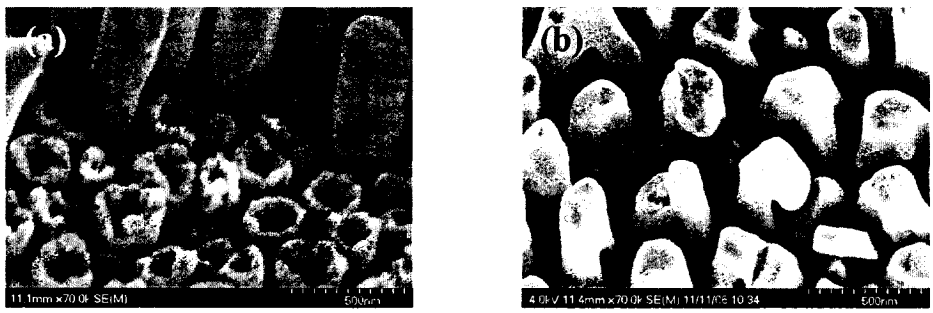

Figure 3.11. Nucleation stage of AuNWs; a) grown from the top side; b) grown from the branched side.

As AuNWs grow more than a few microns long, they tend to make bundles and collapse into an entangled mess after the embedding PAA has been removed. As shown in the SEM micrographs of **Figure 3.12**, this happens because of the surface tension forces exerted on them during the evaporation of the solvent. In fact, the collapse issue was the major obstacle that prevented synthesis of initially targeted, very high aspect ratio (*A.R.* ≈ 500), nanowires. Prior to selection of Anodisc membranes as templates, we developed our own PAAs with pore diameters of 20 nm by anodizing aluminum sheets. **Figure 3.12a** shows that the array of nanowires synthesized using these templates have formed bundles and collapsed. Moving to Anodisc PAAs did not resolve the bundling problem as the pores were still too close together (**Figure 3.12b**), therefore we employed the following method to maintain self-standing AuNWs.

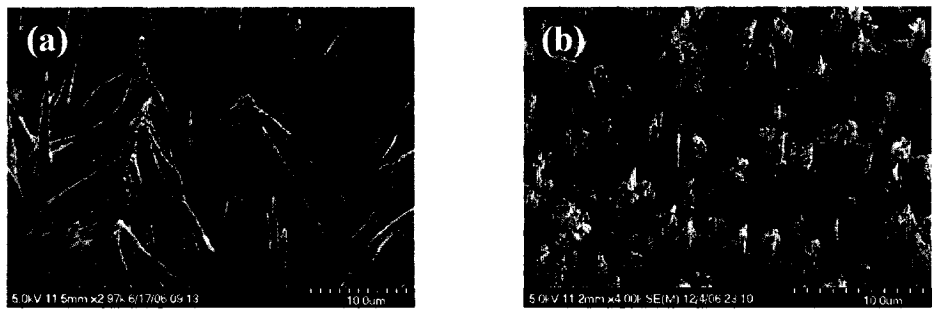

Figure 3.12. Bundling and collapse of AuNWs after removal of the PAA; a) AuNWs grown using custom made PAAs with pore diameter of 20 nm. b) AuNWs grown in Whatman membranes.

3.2.2. Reducing the Compactness of the Array of AuNWs

Before the electrochemical growth, the density of the available pores can be reduced to work around the collapse problem. Increasing the separation of the nanowires reduces the surface tension forces between them and the likelihood of bundling. It is though very difficult to control and reduce the pore density during the fabrication process of PAA membranes, because the pore diameter and spacing both increase with the anodization potential. Our.method, on the other hand, is based on modification of the as-fabricated PAA templates. Polystyrene (PS) microspheres were introduced into the template in order to reduce the density of the nanowire array by partially blocking the pores. The membrane was immersed into a suspension of PS in water (0.05% w/v) and then dried in air. **Figure 3.13** shows the bottom side of an Anodisc PAA after treatment with the PS suspension. The inset shows that some of the microspheres have penetrated inside the pores.

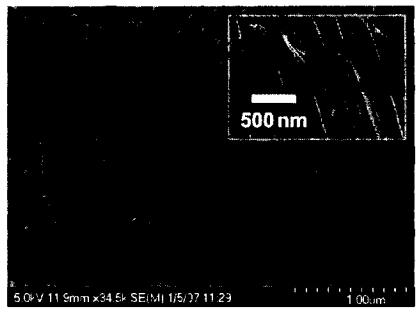

Figure 3.13. Partial blocking of the PAA pores with PS microspheres. Inset: Cross-section of the pores showing the penetrated microspheres.

The bundling problem was resolved in the AuNW arrays grown using the modified templates. SEM micrographs of freestanding AuNWs grown from the bottom and top faces of the modified templates are shown in **Figure 3.14a** and **Figure 3.14b** respectively. The insets show close-ups of the corresponding tips. For the wires grown from the bottom face, the stems are shielded by alumina. Note that the substrates are tilted 45° degrees to expose the length of the nanowires; therefore, the nanowires are actually $2^{1/2}$ times longer than they appear in the SEM image. In contradiction with the value obtained using eqn. ($l_{AuNW} \approx 45.3$ μm), the experimentally obtained nanowires had shorter lengths, because as mentioned earlier, the gold film also grows at the other side of the PAA.

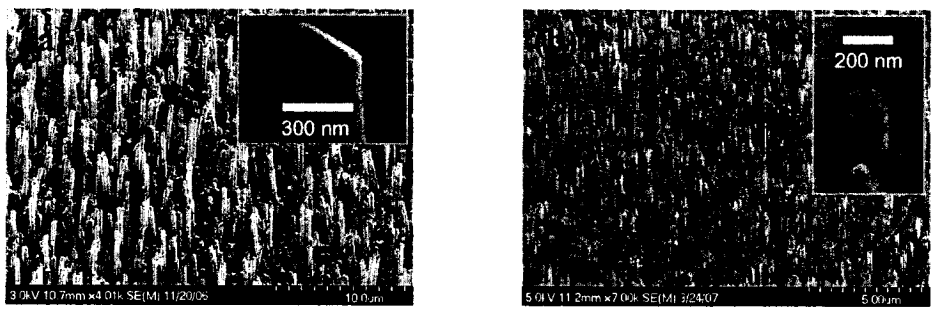

Figure 3.14. SEM images of freestanding AuNWs grown from a) the bottom and b) the top sides of modified PAAs. The insets show the corresponding tips.

3.2.3. Formation of Au Nanoparticles at the AuNW Tips by Impregnation of the PAA

To promote the geometrical field enhancement of the AuNWs, we utilized the impregnation technique to create gold nanoparticle aggregates and whiskers at their tip tops. The structures are often referred to as 'super-tips' [58, 115]. The impregnation technique employs the reduction effect of PAA pore walls and formation of gold nanoparticles inside them, which is well-documented in the literature [116]. Preparation of nanostructured gold within porous solids has been usually conducted at temperatures lower than 250°C or under hydrogen atmosphere [117, 118]. At room temperature however, it is done through a surface-mediated reduction process [116, 119]. A freshly prepared 1% (w/w) $HAuCl_4$-aceton solution as a source of Au^{3+} cations was dropped on the PAA at ambient conditions. The $HAuCl_4$ is converted to gold at rather mild conditions, when it is in contact with a substrate having surface hydroxyl groups like alumina. An H^+-Au^{3+} ion exchange takes place at the pore walls that modifies the redox potential and facilitates formation of gold atoms and clusters.

Prior to impregnation, the template was treated with PS microspheres. Electrodeposition of AuNWs was conducted regularly. Gold nanoparticle aggregates with a size of approximately 5 nm at the pore walls are discernable in the SEM image of **Figure 3.15a**. The aggregates are randomly dispersed inside the pore channels and appear to be anchored to the walls. **Figure 3.15b** shows a close-up of an AuNW tip growth using the impregnated PAA template. Apparently, gold aggregates are separated from the pore walls during the electrochemical deposition process and protruded from the AuNW tip.

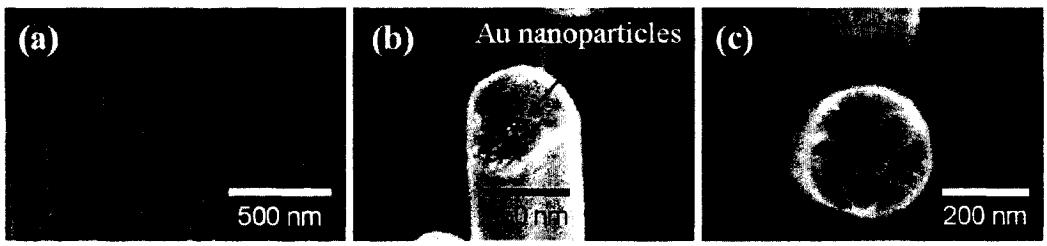

Figure 3.15. Cross section of the pore channels showing the Au aggregates on the walls; b) A single AuNW tip grown through an impregnated template, Au aggregates are swept up while the nanowire is being formed and appear at the tip in form of nanoparticles; c) Another tip containing PS microspheres.

PS microspheres introduced to partially block pores are occasionally trapped during the initial nucleation stage. **Figure 3.15c** shows four of them at the tip top of an AuNW. The similarity in the image brightness and contrast of the microspheres with that of the AuNW, substantiates that the microspheres are embedded in the electrodeposited gold.

3.3. Micro-Raman Measurements and Analysis

We performed Micro-Raman spectroscopy measurements to examine the surface composition of the as-grown AuNW film. Note that gold does not have any Raman modes. We were particularly interested to investigate traces of residual alumina (in form of nanoscale scales) on the AuNWs, after incomplete removal of the PAA. Later we will show that the Schottky-barrier field-enhanced electron emission and low-voltage field ionization mechanisms observed in our AuNW array, can be described based on the existence of residual semiconductive alumina layer.

The line profile of Raman spectra and white light optical microscopy image of a selected area of the AuNW film grown in a regular Anodisc template are presented in **Figure 3.16a** and **Figure 3.16b** respectively. The template was treated in the NaOH solution at room temperature for 7 minutes.

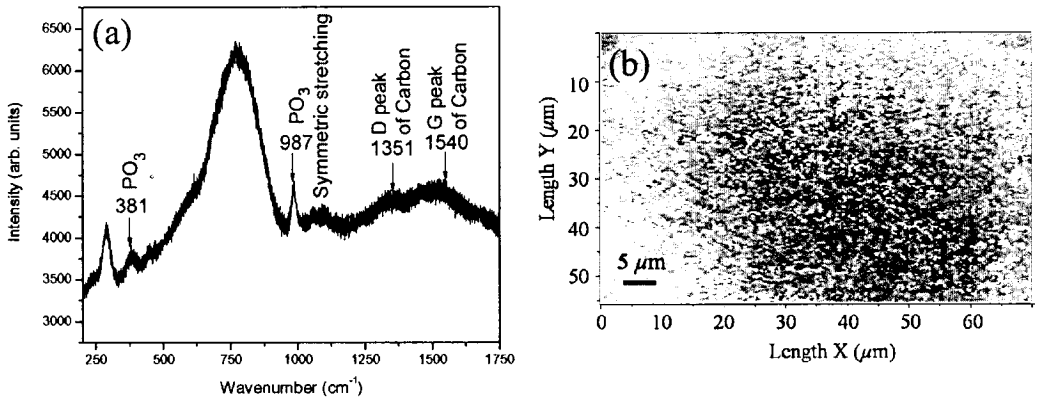

Figure 3.16. a) Raman spectra, and b) optical image of an AuNW film, synthesized within a regular PAA template.

The spectra were recorded in the range of 190 to 1750 cm^{-1}. The peak positions indicate that the sample is having Raman signals from various materials that are present. In order to identify the materials corresponding to the Raman modes, a bi-dimensional Raman mapping was carried out.

The Raman spectrum of the PAA does not have peaks corresponding to amorphous alumina. It is known though alumina has peaks only after a heat treatment at about 1100°C [120], thus the origin of the modes at 292.5 and 785.8 cm^{-1} are not clear. The peaks observed at 381 and 987 cm^{-1}, correspond to the phosphate anions incorporated into the structure of PAA membrane during anodization, suggesting that there is residual alumina on the AuNWs [121, 122]. These peaks disappeared when the template was dissolved in the NaOH solution for prolonged times.

3.4. Optical Profilometry

As mentioned earlier, in addition to filling the pores, electrodeposition of gold takes place at the sputter-coated face of the PAA and creates a backing gold film. In order to characterize our sensor, it is crucial to ascertain how much the backing gold film and the conductive paste used to bond the template to the substrate contribute the total thickness of the AuNW film (t_{AuNW}), after the PAA has been removed. We employed confocal optical profilometry to scan the edge of the deposited film with respect to the substrate. **Figure 3.17** shows an illustration of the AuNW film bonded to the silicon substrate along with the isometric optical topography of the film edge. The measurement was repeated for each sample to find its t_{AuNW}.

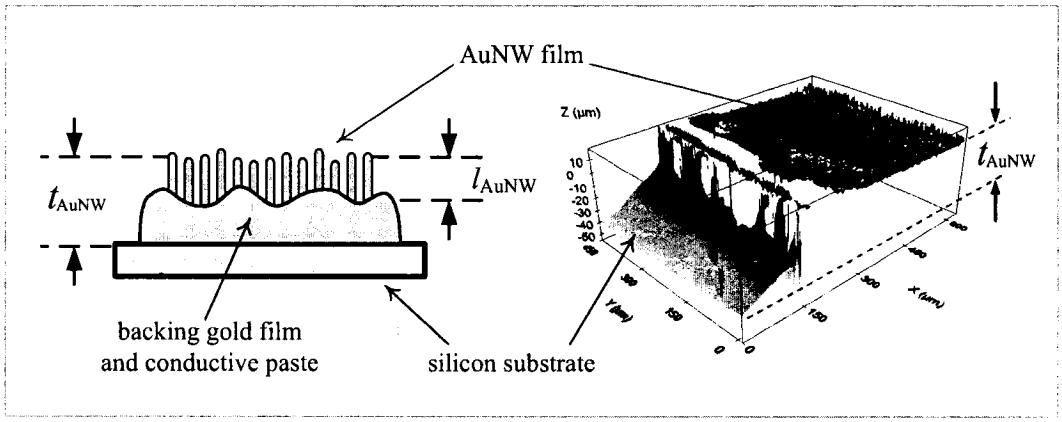

Figure 3.17. Left: Schematic illustration of the AuNW film thickness which includes the backing gold film, the conductive paste and the nanowires. t_{AuNW} and l_{AuNW} denote the total film thickness and the length of the AuNWs respectively. Right: Isometric optical profile of the AuNW film edge, the *z* axis denotes the peak to valley points.

Chapter 4

Device Fabrication and Characterization Techniques

We designed and fabricated a series of Gas Ionization Sensors (GISs) with diverse nanowire geometries and gap distances. These sensors were operated in different modes, namely breakdown discharge and pre-breakdown field-ionization and field-emission. Various characteristics of the sensors were measured at different pressures with several gases. Most of the experiments were carried out in a vacuum system, which we specifically built for this purpose. It was demonstrated that self-sustaining discharges from the nanowires occur at voltages particular to each gas and within a wide concentration range. The breakdown voltages were considerably reduced compared to uniform field conditions. We also obtained measurable field-ion and field-emission currents at pressures up to 100 torr in various gases.

This chapter describes the fabrication process steps in detail with the AuNW film as the starting material. It also explains our measurement methodology and equipment setup.

4.1. Fabrication of the Gas Ionization Sensor

The proposed GIS is basically a double electrode cylindrical cell with the AuNW film and its companion substrate as one of the electrodes. A secondary flat electrode (counter electrode) is placed at a distance *d* (henceforth referred to as gap spacing or interelectrode spacing), above the nanowire tips. We used a double side polished, p-type, 1-inch (same diameter as the Anodisc PAA) silicon wafer as the counter electrode. The exterior side of

the wafer was initially coated with a 1 μm thick layer of aluminum using PVD method and then annealed in an N_2+H_2 atmosphere at 450°C for 30 min to form an ohmic junction. The wafer was then mounted on the supporting polypropylene ring of the PAA, which was engraved at three points to facilitate the flow of gas into the space between the electrodes. Polypropylene is known to have a high volume resistivity (10^{16} – 10^{18} Ω·cm) [123, 124]. Hence, it can also serve as an excellent insulator between the electrodes. The minimum resistance of the ring was calculated to be R_{min} =1.5 × 10^{15} Ω·cm, using the relation

$$R_{\min} = \rho_{\min} \frac{l_{ring}}{A_{ring}}, \tag{4.1}$$

where the ρ_{min} = 10^{16} Ω·cm is the minimum volume resistivity, l_{ring} = 60 μm is the ring thickness, and A_{ring} = 3.9 cm^2 is the ring area.

Ohmic connections were made to either electrode using a silver epoxy. Depending on which side of the PAA was used for electrodeposition, and the amount of glue used in bonding the wafer, d varied from 70 to 140 μm. Cross-sectional and 3D schematic illustrations of the sensor with the AuNWs grown from the bottom side are presented in **Figure 4.1a** and **Figure 4.1b**. **Figure 4.1c** shows a snapshot of the final device. Using optical profilometry, the value of d was determined for each sample after mounting the counter electrode by subtracting the corresponding t_{AuNW} and the counter electrode thickness, t_{ce}, from the total height (t_{total}):

$$d = t_{total} - t_{AuNW} - t_{ce}, \tag{4.2}$$

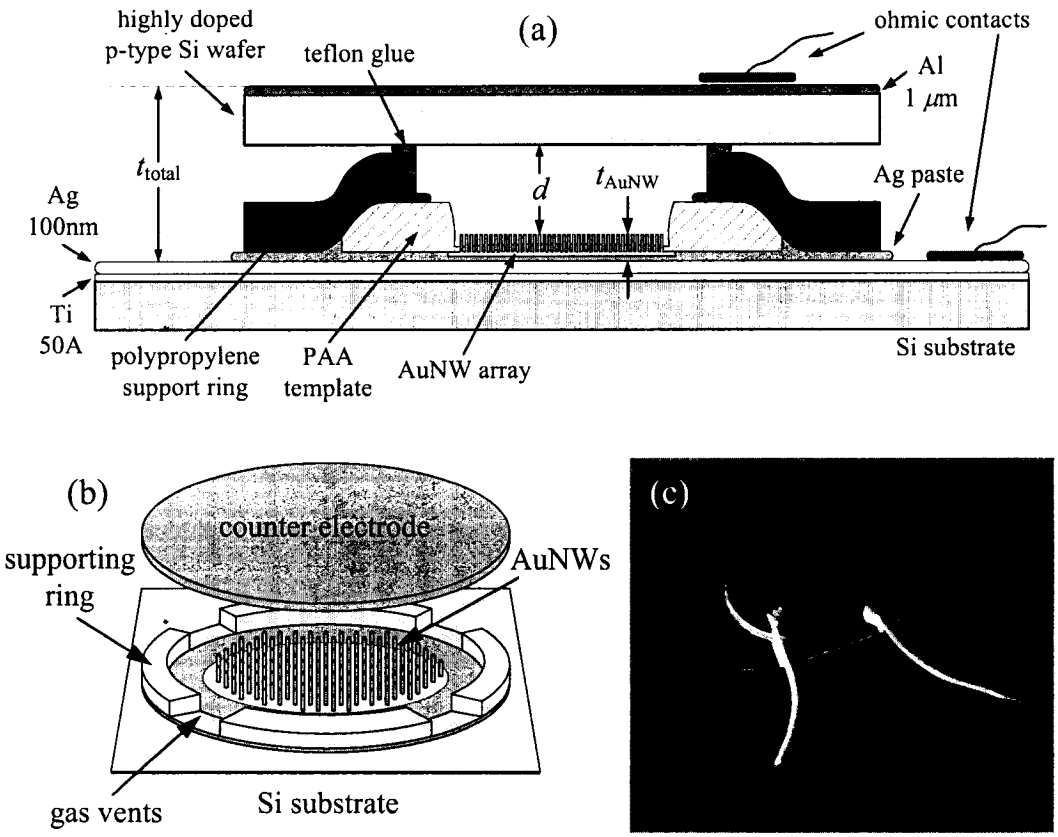

Figure 4.1. a) Cross sectional- and b) 3-D schematic illustrations of the GIS (not to scale); c) a photograph of the final device.

The fabrication process steps and final device structure were similar for all of the nanowire based GISs fabricated and characterized in this research. However, to operate the devices in different modes and study the effect of the nanowire array geometry and composition on the sensors characteristics, we used a variety of AuNW films. These AuNW arrays were grown as explained in Chapter 3. **Table 4.1** summarizes the specifications of each sensor including the AuNW growth parameters, the PAA face sputter-coated with Ag and the average length and the shape of the AuNWs.

Table 4.1. Physical parameters of the sensors fabricated in this research: d_{gap} (d) = gap distance, d_{ms} = diameter of microspheres; Electrodeposition parameters: I = constant galvanostatic current, t = deposition duration, V_i = working electrode vs. Ag/AgCl potential; Geometrical parameters of the AuNWs: l_{AuNW} = length of gold nanowires, b: branched, f: fibrillar, g: guarded, s: super tips, t: top, var: variable, w: whiskers.

Sensor number	d_{gap} (μm)	d_{ms} (nm)	electrodeposition			t_{etch} (min)	PAA face	l_{AuNW} (μm)	AnNW geometry
			t (ksec)	I (mA)	V_i (V)				
1	132	N/A	86.4	1.0	-0.60	15	b	4.5	f
2	121	50	85.6	1.0	-0.59	10	b	12.0	f
3	N/A	50	85.6	1.0	-0.59	15	b	8.0	f
4	83	50	87.3	1.0	-0.63	8	b	10.0	f, s
5	126	50	87.3	1.0	-0.63	7	b	10.0	f, s
6	N/A	100	86.7	1.0	var	30	b	?	f
7	N/A	100	86.7	1.0	var	8	b	3.0	f, s
8	N/A	100	104.0	1.0	var	15	b	?	f
9	N/A	100	93.2	0.9	var	15	b	?	f
10	N/A	100	28.8	3.0	-0.85	7	t	4.0	g, f, w
11	N/A	100	28.8	3.0	-0.85	7	b	3.0	tubular

The reaction voltage (V_i) of galvanostatic electrodeposition remained constant for the AuNW films of Sensors #1 – 5, 10 and 11, showing that the nanowires growth was consistent. For Sensors #6 – 9, we reused the Orotemp gold solution from previous electroplating processes, therefore V_i was varying during the growth. In fact $|V_i|$ increased about 25% at max. However, we did not observe any direct relation between V_i and the characteristics of the corresponding sensor.

The PAA templates used in Sensors #7, 10 and 11 were treated with the $HAuCl_4$ solution as explained in Chapter 3; as a result, their AuNWs contained gold nanoparticles at their tips. Micro-Raman measurements on the AuNWs of Sensors #4, 5, 7, 10 and 11, showed presence of residual alumina due to incomplete removal of the PAA after the NaOH treatment. These sensors were operated in field-emission and field-ionization modes. Rest of the sensors (#1, 2, 3, 6, 8 and 9), were tested in breakdown mode.

Breakdown experiments carried out with the GIS were repeated on a nanowireless parallel-plate cell (PPC), consisted of the same configuration as the GIS, except without the AuNW array. The PPC produces a uniform electric field between the electrodes and allows comparison of the breakdown voltages obtain using the GIS with that of standard flat-electrode ionization cell. As illustrated in **Figure 4.2**, the objective was to maintain the same electrode spacing, d, for both configurations. However, due to the difficulties in controlling the bonding process to the polypropylene ring, d turned out to be smaller for the PPC (d_{PPC} = 84 μm). A denotes the effective electrode area. The bottom electrode of the PPC preserved the Ag coating so that an ohmic contact identical to the GIS could be made.

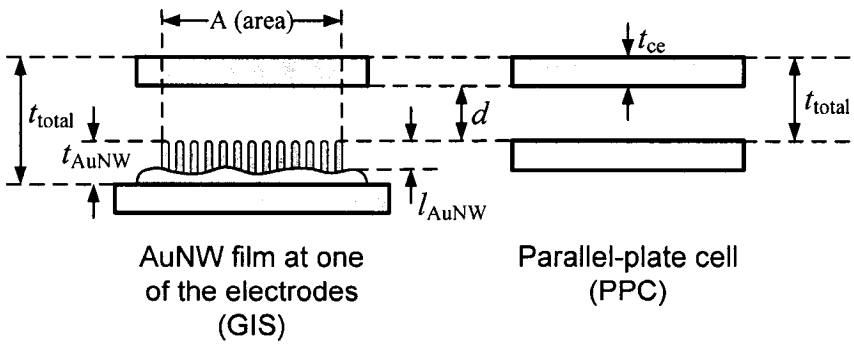

Figure 4.2. Conceptual illustration of the GIS and the PPC, showing the equivalent dimensions.

4.2. Measurement Methodology and Setup

The quantities of interest in characterization of the GIS can be divided in two major categories: a) The pre-breakdown current-voltage ($I - V$) characteristics of the device and b) The gaseous breakdown voltages (V_b), both measured in different gas types and pressures. The former entails low-level measurement techniques and the latter requires rapid detection of the occurrence of breakdown. Conducting such $I - V$ characterization may appear simple at first glance, but the major difficulty is to setup hardware/software configurations that satisfy both requirements.

4.2.1. Low Current Measurement Considerations

The GIS normally exhibits a large resistance before the electric breakdown of the residing gas. Depending on the mode of operation and electrode polarity in this case, current flows due to electron field emission, field ionization of gas, or pre-breakdown Townsend discharge, or a particular combination of these mechanisms. Therefore, in the pre-breakdown regime we are dealing with currents in the range of $10^{-12} < I < 10^{-4}$ A. After the gaseous breakdown however, current rises sharply and can only be limited by the external circuit.

Apparently, a number of error sources can have serious impacts on low-current measurement accuracy. These sources include leakage currents from cables and fixtures, as well as currents generated by triboelectric or piezoelectric effects [125]. In our particular case, due to a finite capacitance of the GIS cells, an unwanted charging current can be also added to the sensor current and explicitly affect the low level field ion and field emission currents. Following addresses the methods we employed to minimize

leakage from the connections and fixtures, as well as the capacitive charging current of the sensor during the staircase voltage sweep. These are known to be the major error sources in low level current measurement from an ultra high resistance source, namely the GIS.

a. Leakage Currents and Guarding

Leakage currents are generated by stray resistance paths between the measurement circuit and nearby voltage sources. The shunt capacitances through out the cables may also contribute to the leakage current, because it draws a charging current at voltage steps. These currents can degrade the accuracy of low current measurements considerably. Guarding is a very effective way to reduce leakage currents. It will also reduce the effect of shunt capacitance in the measurement circuit. A guard is a low impedance point in the circuit that's at nearly the same potential as the high impedance lead being guarded. Since in this research we used precision source-measure units (SMUs) to apply controlled voltages and measure currents, the guarding technique can be best explained specifically on SMUs.

The guard terminal of an SMU is usually the inside shield of the triax connector. This guard is driven by a unity-gain, low impedance amplifier. By definition, the guard terminal is nearly at the same potential as the high impedance terminal, so the guard terminal will be at the same potential as the magnitude of the voltage source.

Figure 4.3 illustrates how a driven guard prevents the leakage resistance of a cable from degrading the low current measurements. In the unguarded circuit of **Figure 4.3a,** the leakage resistance of the coax cable is in parallel with the DUT (R_{DUT}), creating an

unwanted leakage current (I_L). This leakage current will add up with the current from the DUT (I_{DUT}) and degrade very low current measurements. The current measured by the SMU ammeter (I_M) is then given by:

$$I_M = I_{DUT} + I_L . \tag{4.3}$$

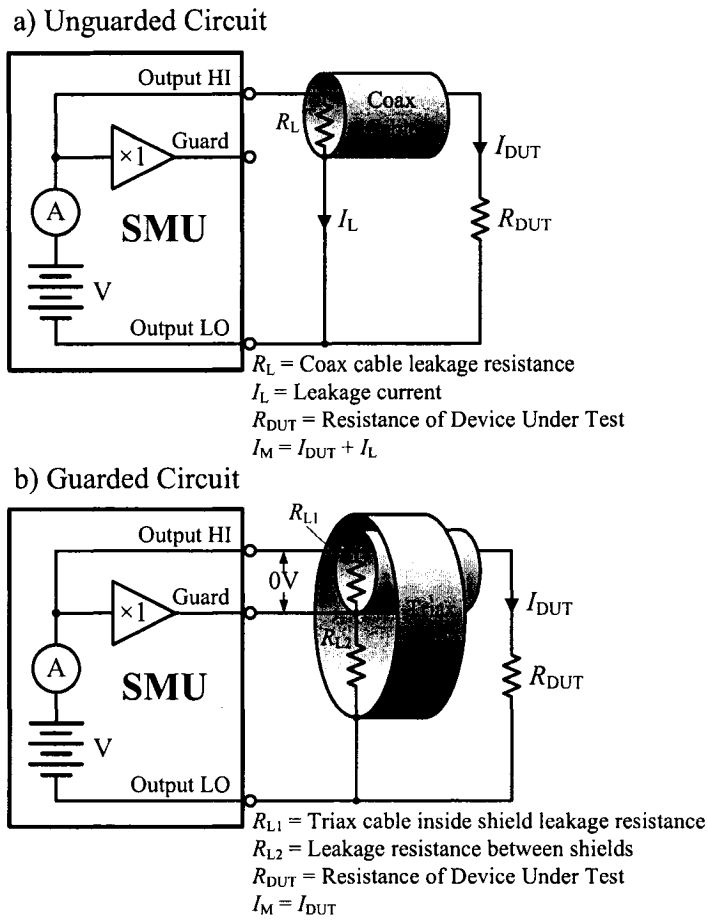

Figure 4.3. Guarding the leakage resistance of a cable with an SMU

In the guarded circuit shown in **Figure 4.3b,** the inside shield of the triax cable is connected to the guard terminal of the SMU. Now this shield is driven by a unity-gain,

low impedance amplifier (Guard). The difference in potential between the Output HI terminal and the Guard terminal is nearly 0V, so I_L is eliminated.

Figure 4.4 shows how the guard can eliminate the leakage current that may flow through the stand-off insulators in a test fixture. In **Figure 4.4a**, I_L flows through the stand-off insulators (R_L). This leakage current is added to the current from the DUT (I_{DUT}) and is measured by the SMU ammeter (I_M), adversely affecting the accuracy of the low current measurement.

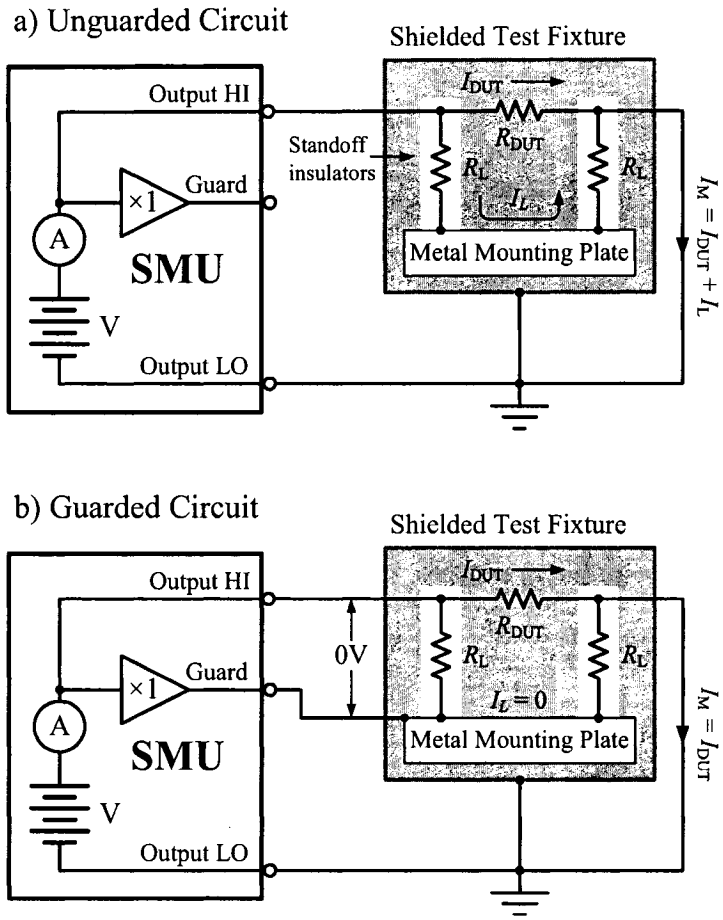

Figure 4.4. Text fixture guarding with an SMU.

In **Figure 4.4b**, the metal mounting plate is connected to the guard terminal of the SMU. The voltages at the top and the bottom of the standoff insulator are nearly at the same potential (0V drop), so no leakage current will flow through the standoffs and affect the measurement accuracy. For safety purposes, the metal shield must be connected to earth ground because the metal mounting plate will be at the guard potential.

b. The Effect of the Charging Current during the Staircase Voltage Sweep

A linear staircase sweep type was used as usual to perform the $I - V$ characterization. As shown in **Figure 4.5**, this sweep steps from a start source value to an ending (stop) source value. Programmable parameters are the start, stop, and step source levels and the source delay. When this sweep is triggered to start, the output will go from a bias level to the start source level. The output will then change in equal steps until the stop source level is reached. With trigger delay set to zero, the time duration at each step is determined by the source delay (**Figure 4.5**) plus the extra time it takes to perform the measurement or the integration period. This extra time is determined by Number of Power Line Cycles (NPLC) which expresses the integration period by basing it on the power line frequency [126]. For example, for a NPLC setting of 1, the integration period would be 1/60 (for 60 Hz line power) which is 16.67 msec.

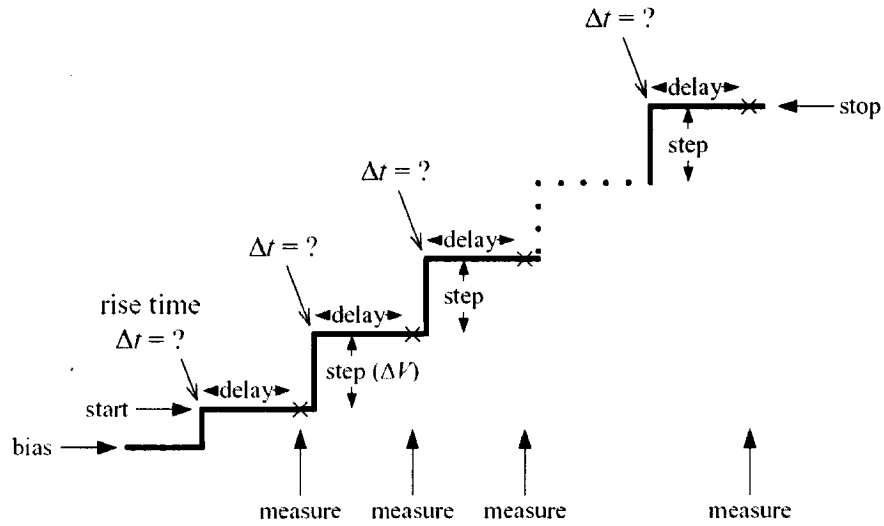

Figure 4.5. Linear staircase voltage sweep and the corresponding parameters.

Obviously, when the staircase pattern is applied to a DUT with a finite capacitance (C), a charging current (I_{cap}) is drawn from the SMU at each voltage step (ΔV). The charging current damping time is determined by the effective RC constant of the circuit. In characterization of our GIS, I_{cap} is adversely added to the pre-breakdown discharge currents. The capacitive current is given by

$$I_{cap}(t) = I_0 \exp(-t/RC), \tag{4.4}$$

where t is elapsed time, and I_0 is the peak of charging current given by

$$I_0 = C\Delta V/\Delta t, \tag{4.5}$$

where C is the cell capacitance, and ΔV and Δt are the voltage step and the pulse rise time respectively. Although Δt is relatively small compared to the source delay time, it is not documented in the SMU datasheet [126-128]. Therefore, the delay time must be chosen properly to ensure that I_{cap} becomes zero or negligible compared to the real pre-breakdown currents, before the 'measure' cycle as indicated by crosses in **Figure 4.5**.

4.2. Sensor Characterization Setup

We carried out our characterization experiments in the vacuum chamber of the DC magnetron sputtering machine (MagSput-2G2) used in the thin film coating of PAA templates. This chamber is equipped with a mass flow controller and a computer driven vacuum gauge. The chamber was connected to earth ground to also serve as the shielded test fixture. *I–V* and breakdown voltage measurements up to 200V were conducted using two SMU channels of an HP4155 semiconductor parameter with a current resolution of 10 fA [127]. To achieve higher voltages up to 420V, we used Keithley 2400 SourceMeters, with a current resolution of 10 pA [126]. Note that the individual SMU channels of HP4155 and Keithley 2400 are capable of sourcing voltages up to 100V and 210V respectively. Consequently, to achieve even higher voltages necessary to generate breakdown conditions, two SMUs were connected in series sharing the same ground. In this configuration, one SMU sweeps in positive direction while the other sweeps in negative direction. The result is a floating measurement with double the differential voltage. In this fashion also the current to either electrode can be measured individually. Two custom-made electrical feedthroughs were used to facilitate guarded triax connections from the SMUs to the exterior of chamber, and coax connections from the interior of chamber to a custom-made mounting plate. The mounting plate was insulated from the chamber and connected to the guard terminal of SMU#1, and the sensor was eventually connected to the output HI terminals. **Figure 4.6** shows a schematic of the characterization setup.

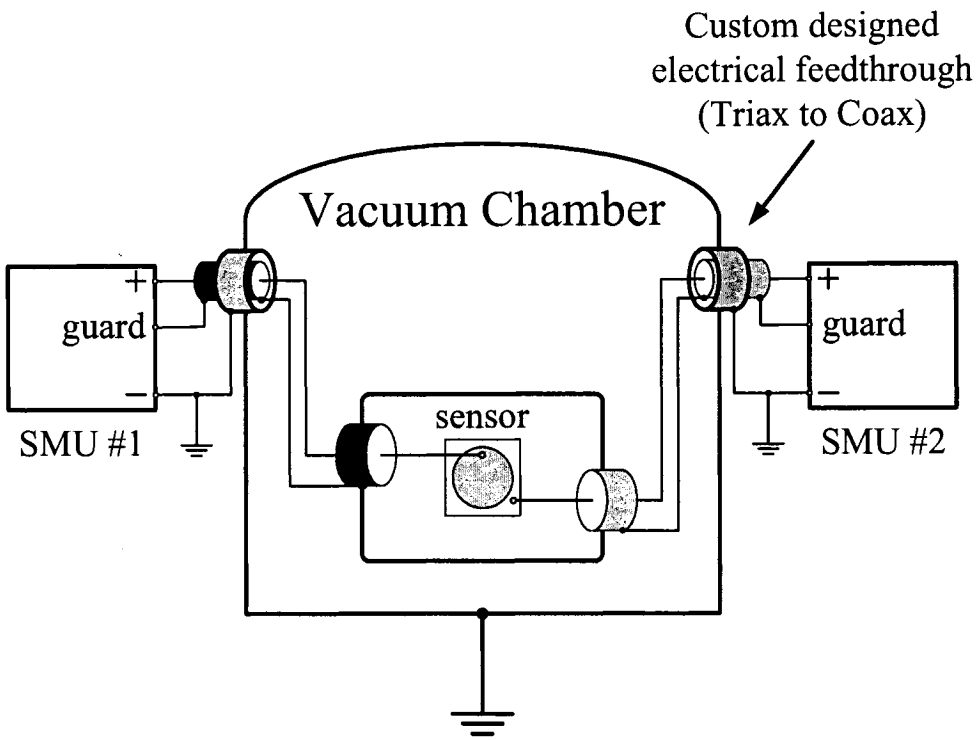

Figure 4.6. Schematic illustration of the measurement setup; The connections to the sensor are made using triax cables from the output HI terminals of SMUs to the chamber, and coax cables from the feedthroughs to the mounting plate.

A LabView code was developed to acquire the current and voltage readings from the parameter analyzer, and the chamber pressure from the vacuum gauge simultaneously into excel sheets.

The custom-made feedthroughs displayed a finite resistance (R_{FT}) that needed to be considered as well. This resistance was mainly due to moderate quality insulation used at their connectors (epoxy glue). As shown in **Figure 4.7**, R_{FT} was measured to be about 2×10^{13} Ω by running a voltage sweep with no load, and finding the slope of the resulting $I - V$ curve. During $I - V$ measurements, we made sure that the leakage current into the feedthroughs is negligible compared the real pre-breakdown current.

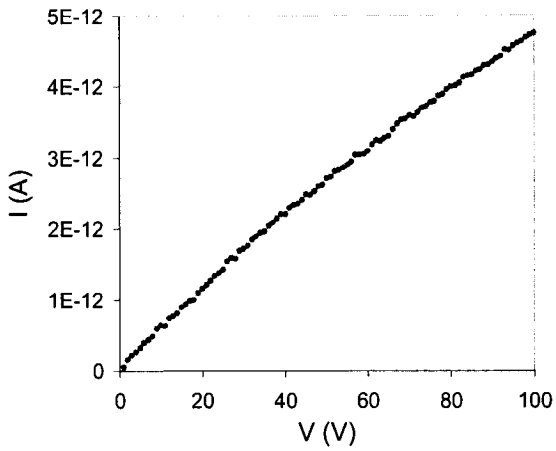

Figure 4.7. The no-load $I - V$ characteristic of the measurement setup. The finite resistance is mainly due to the electrical feedthroughs that interface the vacuum chamber to the SMUs.

We showed that for a differential voltage step of $\Delta V_{\text{diff}} = 1$ V, that is a step of $\Delta V = \Delta V_{\text{diff}}/2 = 0.5$ V for each of the SMUs, a sweep delay of $t_d = 25$ ms is sufficient to ensure that I_{cap} dies off, hence any steady-state pre-breakdown current measurement is accurate.

Chapter 5

Results and Discussions

5.1. Gaseous Breakdown Ionization Sensor

In order to achieve self-sustaining discharge at reduced voltages, one of the electrodes of the ionization cell must be stressed to create locally nonuniform fields. The breakdown process is hastened due to generation of corona at the stressed electrode, which promotes the formation of an electron avalanche or plasma streamer. Eventually, the streamer bridges the gap between the electrodes, and allows a self-sustaining interelectrode discharge to be created at relatively low voltages.

In addition to having sharp field-intensifying features, the electrode at which corona is generated must undergo an excessive heat and be chemically inert and endurable. We have shown that the array of vertically-aligned freestanding AuNWs is a reliable and efficient replacement for the CNT film used by Kim [18] and Modi et al. [19] in their miniaturized GIS. Our device exhibited breakdown characteristics similar to that of [19], and improved compared to that of [18]. The reusability of our device was enhanced compared to both CNT-film counterparts. CNT-film GISs suffer from reusability concerns, since extremely dense CNTs make dispersion of the gas difficult, so the sensor cannot be reused prior to some sort of cleaning treatment [22]. The overall field enhancement factor of the AuNWs was estimated by operating the sensor in the dark current discharge mode and found to be proportional to their aspect ratio.

5.1.1. Ohmic and Saturation Stages

Sensor #1 was developed to fingerprint the ionization breakdown voltage of a number of gases. Prior to the breakdown tests, we operated the device at lower voltages in the pre-breakdown regime to study the field enhancement effect of AuNWs on the pre-breakdown (dark) current ($I_{pre\text{-}bd}$). The effect of electrode polarity on $I_{pre\text{-}bd}$ was also studied and the results were compared to uniform field conditions. It is imperative to note that the field enhancement factor of the AuNWs of Sensror #1, (β_{AuNW}), was not high enough to generate any electron field-emission or field-ionization. Hence the dark current consisted of already generated electron-ion pairs and the charges generated by electron impact ionization.

The pre-breakdown discharge $I - V$ characteristics of Sensor #1 (GIS) with the AuNWs configured as the cathode, and the PPC in low pressure air are presented in **Figure 5.1** [129]. The pressure was kept constant during the sweep ($P = 1.4\times10^{-5}$ torr).

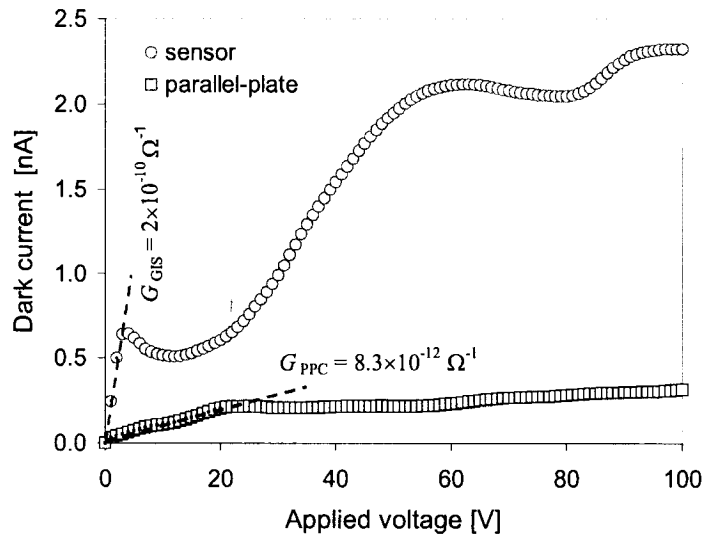

Figure 5.1 (*after Banan-Sadeghian and Kahrizi in* [129]). Dark discharge current of the GIS and the PPC in low pressure air ($P = 1.4\times10^{-5}$ torr) with the AuNWs at the cathode.

The ohmic region in both of the devices is evident in **Figure 5.1** (indicated by dashed trend lines). In this region, where there is hardly any ionization-induced current, the effective conductances of the GIS (G_{GIS}), and the PPC (G_{PPC}) in an ideal gas (air in this case), is equal to the slope of their $I - V$ characteristics.

The supposed saturation pre-breakdown region for the NWGIS, however, demonstrates a strong voltage dependence, including negative differential resistivity (NDR) regions over certain voltage ranges. The first NDR effect is observed right after leaving the ohmic region. This behavior can be attributed to a momentary increase in the ion-electron recombination rate which takes place in highly non-uniform electric fields at the nanowire tips, considering a constant generation rate in the chamber.

The NDR region is followed by a quasi-exponential current rise starting at $V = 12$ V, due to liberation of secondary electrons from the AuNWs. At this point the average applied field in the gap is about $E_{app} = 10^3$ V.cm^{-1} and the reduced field is $E/P = 7\times10^7$ V.cm^{-1}torr^{-1} (or $E/c_g = 2\times10^{-9}$ V.cm^2). This value of E/c_g is almost four orders of magnitude larger than the maximum E/N employed to measure ω/α of air in [130]. However, considering the monotonic growth of ω/α above $E/c_g = 7\times10^{-15}$ V.cm^2 (where $\omega/\alpha \approx 0.0015$), remarkably large ω/α values can be expected. Conversely, α shrinks to a very small value, indeed below 1cm^{-1}, because λ_e becomes much longer than the gap spacing d. At $V = 60$V a second NDR state is observed because of a recombination dominated regime. Apparently, the number and amplitude of current peaks depend on the non-uniformity of AuNWs at the cathode. Consequently, in the GIS with cathode AuNWs a non-self-sustaining Townsend discharge dominated by secondary electrons, replaces the field independent saturation regime (J_{sat}) as observed in the PPC.

5.1.1.a. Field Enhancement Effect of the cathode AuNWs and their Aspect Ratio

Looking back to **Figure 5.1**, it is clear that G_{GIS} is considerably higher than G_{PPC}. Considering constant mobilities within the studied electric field range, the increase in the conductivity of the sensor can be related to the local enhancement of electric field at the nanowire tips. A general expression that explains this relationship can be extracted as follows:

In the PPC, the electric field is more or less uniform and is equal to the applied field E_{app}. According to (2.3), the current density can be obtained by

$$J_{PPC} = \sigma_{Gas} E_{app} \tag{5.1}$$

In the GIS, however, the electric field is nonuniform, so E_{app} should be replaced by E_{eff}, an effective enhanced value. From (2.34), E_{eff} can be defined as

$$E_{eff} = \beta_{GIS} E_{app} \tag{5.2}$$

where β_{GIS} is assumed to be the average field enhancement factor through the gap spacing of the sensor. The current density can then be expresses as

$$J_{GIS} = \sigma_{Gas} \beta_{GIS} E_{app} \tag{5.3}$$

Since both of the devices were examined at the same time and in the same chamber, gas conductivity would be the same, so the ratio of the current densities would be

$$J_{GIS}/J_{PPC} = \beta_{GIS} \tag{5.4}$$

and from that

$$\frac{G_{GIS}}{G_{PPC}} = \frac{I_{GIS}/V_{GIS}}{I_{PPC}/V_{PPC}} = \frac{\left(J_{GIS}A_{GIS}\right)/\left(E_{app}d_{GIS}\right)}{\left(J_{PPC}A_{PPC}\right)/\left(E_{app}d_{PPC}\right)} = \beta_{GIS}\frac{A_{GIS}d_{PPC}}{A_{PPC}d_{GIS}} \tag{5.5}$$

where A_{GIS}, d_{GIS}, A_{PPC} and d_{PPC} are the respective areas and electrode separations for the GIS and the PPC. As a result β_{GIS} can be found by substituting the values of G_{GIS} and G_{PPC} from **Figure 5.1**, d_{GIS} = 132 μm (from **Table 4.1**), and d_{PPC} = 84 μm into

$$\beta_{GIS} = \frac{G_{GIS}}{G_{PPC}} \frac{A_{PPC} d_{GIS}}{A_{GIS} d_{PPC}}. \tag{5.6}$$

For $A_{GIS} \approx A_{PPC}$, the above formula results $\beta_{GIS} \approx 37.9$. This is almost 8 times higher than the enchantment factor of the CNT film sensor [22].

Lee and Huang [131] have shown that in an array of field-emitting sharp protrusions, as the emitter tip-to-tip spacing (s) is narrowed, the field strength at the apex of the tips is diminished due to the larger electrostatic interaction between them. We carried out finite element analysis on a well-aligned metallic nanowire array model to demonstrate the aforementioned effect on the field enhancement factor of individual nanowires. The parameters employed in the analysis are shown in **Table 5.1**. Provided that the condition: $l << d$ is met, β was almost independent of l and d_{gap} [54]. A maximum value of β_{max} = 36 was obtained, which corresponds to the local field at the apex of the tips and is close to the value estimated using (5.6).

Table 5.1. Parameters used in finite element simulation of the field enhancement effect.

V_{app}	l_{AuNW}	d	r_{tip}	s
100 V	1 μm	100 μm	20 nm	50 – 350 nm

Figure 5.2 shows the spatial distribution of electric field strength at the vicinity of two nanowire tips, 50 nm apart. The normalized value of β with respect to its maximum, as a function of s is shown in **Figure 5.3a**. Also **Figure 5.3b** and **Figure 5.3c**, show the

contours of the field strength at the apex of nanowire tips for s = 50 nm and s = 350 nm respectively. It can be seen that for s < 300 nm, β starts to drop and reaches to 90% of its maximum value at s = 50 nm. At smaller distances, β decreases drastically. For distances above 300 nm, β is almost unaltered. As seen in the SEM micrographs of **Figure 3.14**, it is clear that the average AuNWs separation is higher than 300 nm. Note that we have addressed the worst case scenario, where the neighboring nanowires have the same length. Therefore, the contraction of equipotential lines is at maximum.

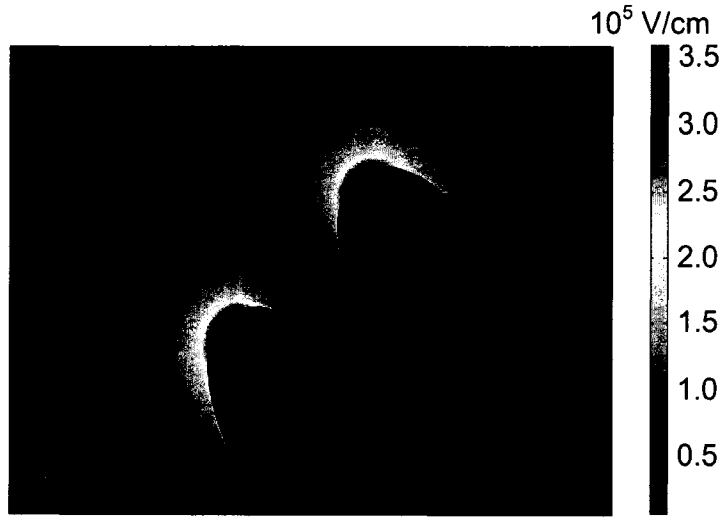

Figure 5.2. Spatial distribution of the electric field at the vicinity of two nanowire tips.

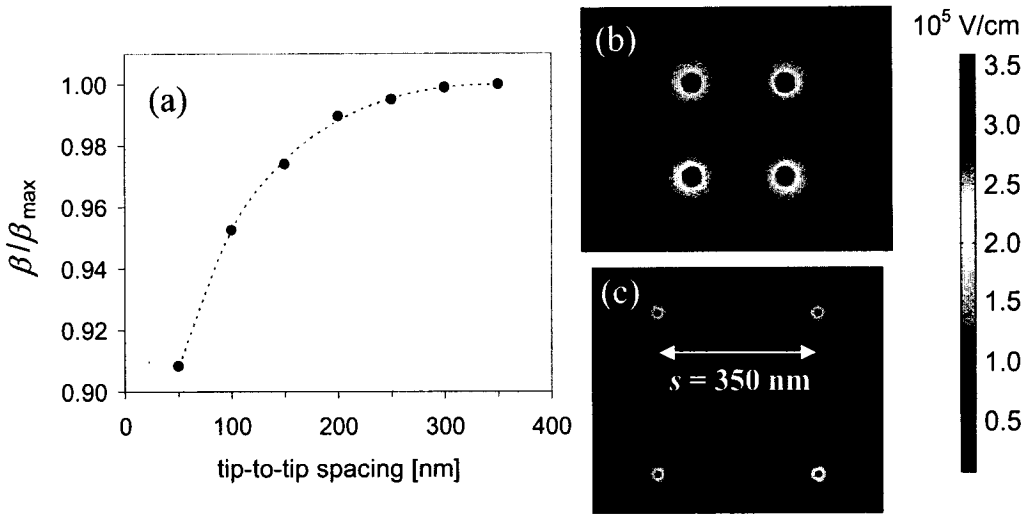

Figure 5.3. Normalized β as a function of nanowire tip-to-tip spacing, and the electric field distribution contours at the apex of four nanowires with separation of b) 50 nm and c) 350 nm.

To further validate the value of β obtained from conductance measurements, in addition to finite element analysis, we employed the 'hemisphere on a post' model. According to this model and (2.39), the nanowire aspect ratio (*A.R.*) can be explained by

$$A.R. = \frac{l}{2\rho} = \frac{\nu}{2} \approx \frac{1}{2}\left[0.90\sqrt{\frac{\beta_{GIS}}{1.2}} - 2.15 \right] \tag{5.7}$$

where 2ρ denotes the nanowire diameter.

By substituting $\beta_{GIS} \approx 37.9$ obtained from (5.6), and $2\rho \approx 180$ nm into (5.7), and assuming that the average AuNW diameter is equal to the average pore diameter of the embedding Anodisc template, the average length of AuNWs was estimated to be

$l_{AuNW} = 2\rho \times A.R. = 0.18\mu m \times 24.8 \cong 4.0\mu m$,

which is interestingly, in good agreement with our SEM observations (see **Figure 5.4**).

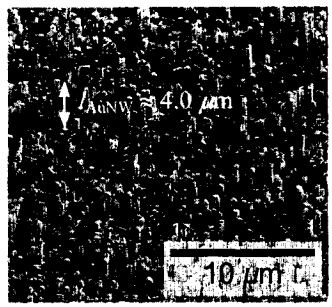

Figure 5.4. SEM micrograph of the AuNW film incorporated in Sensor #1.

In fact, the aspect ratio of AuNWs is less than that of CNTs, but unlike CNTs, AuNW tips are far from each other so that the interactions between the tips do not reduce the effective field enhancement factor. As a result, our nanowire based GIS and its CNT film counterpart are expected to exhibit substantially similar device characteristics, as far as the local field strength is concerned. For instance we demonstrated that the $V_b - P$ characteristic of our GIS is similar to the MWCNT film sensor of Modi et al. [19]. The breakdown characteristics of our GIS will be discussed in detail in section 5.1.2.

5.1.1.b Anode AuNWs

Unlike the former case, with the AuNW film configured as the anode, the enhanced ionization at low voltages was not observed and both the PCC and the GIS displayed similar *I–V* characteristics (**Figure 5.5**)

In this case, positive ions strike the polished counter electrode where the conditions to provide sufficient secondary electrons are not met. The higher saturation current observed in the GIS, however, can be attributed to higher number of carriers residing in the gap, due to its larger effective volume compared to that of PPC. The ratio of the dark currents in the saturation regime is $I_{GIS}/I_{PPC} = 1.48$. According to (2.4), this value agrees well with the ratio of interelectrode distances, $d_{GIS}/d_{PPC} = 1.48$, provided that the devices have same electrode areas ($A_{GIS} = A_{PPC}$).

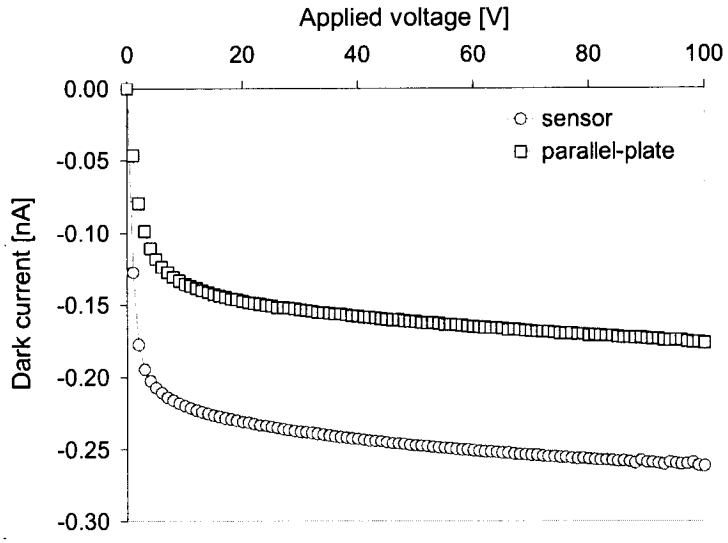

Figure 5.5 (*after Banan-Sadeghian and Kahrizi in* [129]). Dark discharge current of the GIS and the PPC in low pressure air, when the AuNWs are configured as the anode ($P = 1.0\times10^{-5}$ torr).

5.1.2. Breakdown Voltage

Variation of the breakdown voltage V_b, versus gas pressure P, in our GIS device was studied and compared to the PPC. The general gas law states that P is proportional to c_g, provided that a constant temperature is stipulated. According to the Paschen law, V_b is a function of the product of gas pressure and the gap distance ($P.d$). Therefore, for a specific value of d, the $V_b - P$ characteristic of the sensor can be used as a measure of its sensitivity, in a sense that a more sensitive device detects lower gas concentrations (pressures) with a smaller V_b.

Figure 5.6 displays the $V_b - P$ curves of the GIS (Sensor #1) and the PPC at sub-torr pressures of Ar, where the Townsend theory of discharge applies. Note that V_b is the minimum voltage measured that initiated a self-sustaining discharge. It is clear that the GIS demonstrated a lower V_b than the PPC. The reduction effect was even more pronounced when the AuNW film was configured as the cathode, because in this case

secondary electrons repelled away from the AuNW tips into the gap make more ionizing collisions, causing the breakdown to happen at lower voltages.

Apparently, the reduction of V_b in the GIS was not proportional to the field enhancement factor ($\beta_{GIS} \approx 37.9$) obtained earlier. This is due to the fact that the distribution of the intensified field is limited to a short distance within the gap spacing, i.e. at the vicinity of AuNW tip tops.

Considering the gap spacing of the PPC, ($d_{PPC} = 84\ \mu m$), the sub-torr pressure regime corresponds to $P{\cdot}d$ values less than 8.4×10^{-3} torr.cm. Hassouba et al. reported earlier that for $P{\cdot}d \lesssim 10^{-2}$ torr·cm, the minimum breakdown voltage of Ar in uniform fields is 360V, for a polished Ag film cathode [132]. This is indicated by a dashed line in **Figure 5.6** for comparison. Our PPC on the other hand, showed a slightly lower V_b . The lower V_b of PPC can be explained based on an increase in the value of γ, due to the rough microstructure of the Ag-coated bottom electrode.

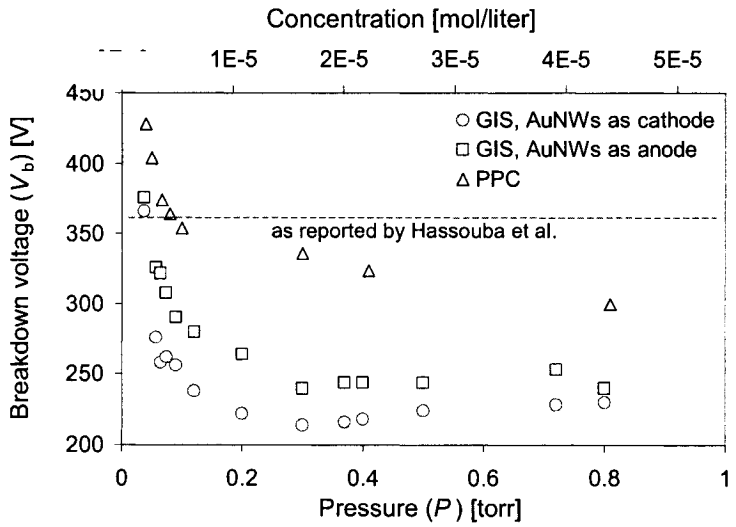

Figure 5.6 (*after Banan-Sadeghian and Kahrizi in* [129]). $V_b - P$ characteristics of the GIS and PPC, in sub-torr Ar at $T = 22$ °C. The NWGIS with cathode AuNWs displays lowest breakdown voltages within the studied pressure (concentration) range. Dashed line shows the uniform field minimum V_b adapted from Hassouba et al. in [132], within the same $P.d$ range.

Figure 5.7 shows the $V_b - P$ curves of a few gases measured using the GIS (Sensor #1) with the AuNWs at the cathode. Each gas displayed a unique V_b at room temperature within the studied pressure range of $0.03 < P < 10$ torr or $4\times10^{-4} < P{\cdot}d < 0.132$ torr·cm (corresponding to concentrations from 1.8×10^{-6} to 1.8×10^{-4} mol·liter^{-1}).

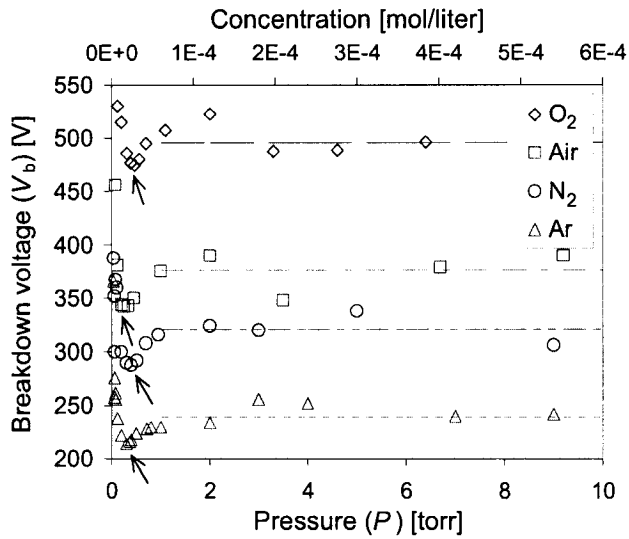

Figure 5.7 (*after Banan-Sadeghian and Kahrizi in* [129]). $V_b - P$ curves of Sensor #1 for Ar, N_2, Air and O_2 (AuNWs at the cathode). The minimum breakdown voltage $(V_b)_{min}$, observed here, occurred within a pressure range of $0.3 < P < 0.5$ torr, which is far less than the pressures at which V_b is minimum in uniform fields.

Table 5.2 represents the mean V_b values indicated by dashed lines in Figure **5.7**. The breakdown voltages measured here, were much less than the values reported in [18] using CNTs as the cathode, and demonstrated very less dependence on gas concentration within a wider range. For instance in the CNT-based GIS [18], V_b of Ar increased from 270V to 1000V, when the gas concentration decreased from 10^{-5} to 1.3×10^{-6} mol·liter^{-1}, yet in our GIS the maximum span of V_b was 214 – 366V that happened for Ar concentrations

below 1.6×10^{-5} mol·liter^{-1}, while for higher concentrations V_b remained almost unaffected.

Table 5.2. Room temperature V_b values of several gas types measured with our GIS (AuNWs at the cathode).

Ar	N_2	Air	O_2
239 V	321 V	377 V	495 V

As shown in **Figuer 5.7**, the Paschen-like minima (i.e. $(V_b)_{min}$, P_{min} pair) of the studied gases, occurred within the range of $0.3 < P_{min} < 0.5$ torr $(0.0396 < (P.d)_{min} < 0.066$ torr·cm). In fact, these values of $(P.d)_{min}$ measured by our GIS, are far less than the typical $(P.d)_{min}$ values in uniform field conditions [30]. **Table 5.3** illustrates a comparison between the P_{min} values of the GIS obtained from the curves of **Figure 5.7** and the typical P_{min} values obtained in uniform fields, considering the same gap distance of d_{GIS} = 132 μm (compare the 1st and the 3rd rows).

Table 5.3. Comparison of the P values at which minimum V_b is measured, between our GIS and the standard Paschen curves obtained in uniform fields.

	P_{min} of the GIS (see **Figure 5.7**) (torr)	$(P.d)_{min}$ uniform fields [30] (torr.cm)	$P_{min} = (P.d)_{min} / d_{GIS}$ (torr) ↑ uniform fields
Ar	*0.30*	0.90	*68.2*
N_2	*0.40*	0.67	*50.8*
Air	*0.40*	0.57	*43.2*
O_2	*0.47*	0.70	*53.0*

The irregular (V_b, P) pair minima observed in the $V_b - P$ characteristics at certain low concentrations, can also be ascribed based on the increase in ω/α. Breakdown voltages increased at very low pressures (below ~0.4 torr) because there were very few number of gas molecules that could diffuse through the vents into the space between electrodes, therefore higher voltages were required to trigger an avalanche breakdown.

In addition to Sensor #1, we tested 5 other GISs (#2, 3, 6, 8, and 9) in the breakdown mode, among which only Sensor #2 displayed a breakdown characteristics superior to Sensor #1. Moreover, Sensor #2 was successfully tested only in sub-torr argon. **Figure 5.8** displays the resultant $V_b - P$ curves obtained with both polarities of the AuNW film [133]. Similar to Sensor #1, the breakdown voltages were lower when the AuNWs were at the cathode. V_b remained constant for $P > 0.1$ torr and increased at lower pressures. On the other hand, Sensor #2 displayed a considerably lower V_b for Ar in average, than Sensor #1 ($V_{b2} = 162$ V vs. $V_{b1} = 239$ V).

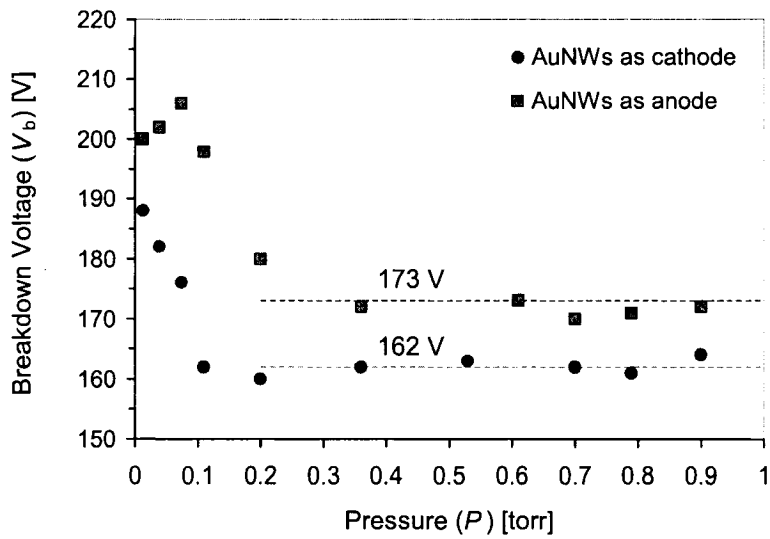

Figure 5.8 (*after Banan-Sadeghian and Kahrizi in* [133]). $V_b - P$ characteristic of GIS (Sensor #2) in sub-torr argon, with both polarities of the AuNW film.

The reason of such reduction can be described based on the different morphology of the AuNW films incorporated in each of these sensors, noting that the gap distance is almost identical for both GISs (see **Table 4.1**). SEM micrographs taken from the AuNWs of Sensor #1 and Sensor #2 are presented in **Figure 5.9**. It can be seen that Sensor #2 contains longer AuNWs. The density of AuNW array is also less in Sensor #2, because polystyrene microspheres where used to reduce the density of available pores.

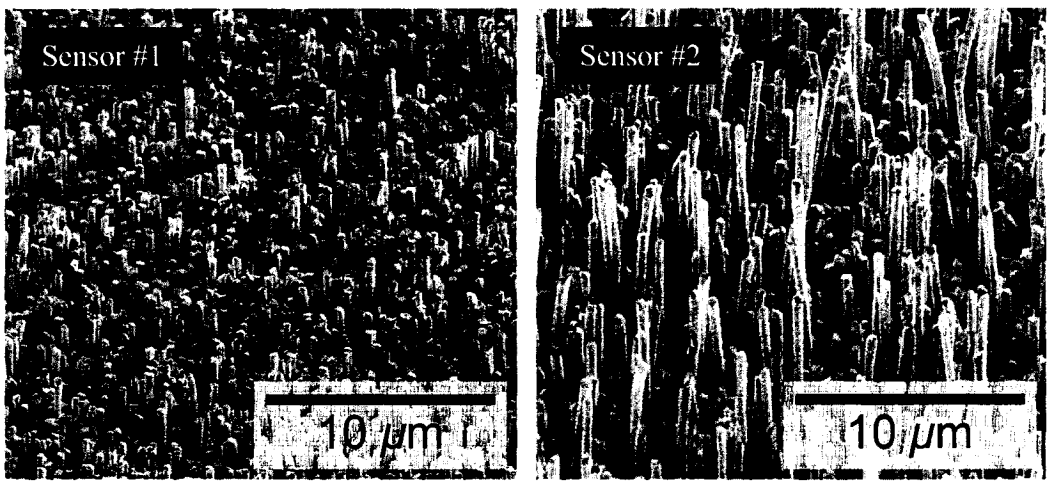

Figure 5.9. SEM micrographs of the AuNW films incorporated in Sensors #1 and #2. The substrate is tilted 45°. Note the difference in morphologies. Sensor #2 has longer nanowires with larger separation and larger length distribution.

Knowing the length of AuNWs in these GISs (**Table 4.1**), we can calculate the ratio of the field enhancement factors. From (2.39), we have

$$\frac{\beta_{GIS1}}{\beta_{GIS2}} = \left(\frac{2.15+\nu_1}{2.15+\nu_2}\right)^{0.90} = \left(\frac{2.15\rho + l_{\mathrm{AuNW1}}}{2.15\rho + l_{\mathrm{AuNW2}}}\right)^{0.90} \tag{5.8}$$

where β_{GIS1}, β_{GIS2} , l_{AuNW1} and l_{AuNW2} are the corresponding field enhancement factors and average nanowire lengths, and ρ is the average nanowire diameter, assumed to be the same in both films ($2\rho \approx 180$ nm).

By substituting the values l_{AuNW1} = 4.5 μm and l_{AuNW2} = 12 μm from **Table 4.1** into (5.8), we find $\beta_{GIS2}/\beta_{GIS1}$ = 2.38 and from that, β_{GIS2} = 2.38×37.9 = 90.2.

To compare with Sensor #1, we would expect a reduction in the breakdown voltages measured by Sensor #2, proportional to the field enhancement factor ratios. In other word, since the electric fields are 2.38 times higher at the AuNW tips of Sensor #2, V_{b2} should be 2.38 times smaller than V_{b1}. However, V_{b1}/ V_{b2} = 239/162 = 1.48.

Apparently, the reduction of the breakdown voltages (e.g. of argon in this case), could not be quantified based on the ratio of field enhancement factors. In addition to the local amplification of the electric field at the nanowire tips, the extent at which this field is distributed should be taken into account. **Figure 5.10** illustrates two different cases to clarify the effect of extension of the enhanced electric field through the gap on the breakdown behavior.

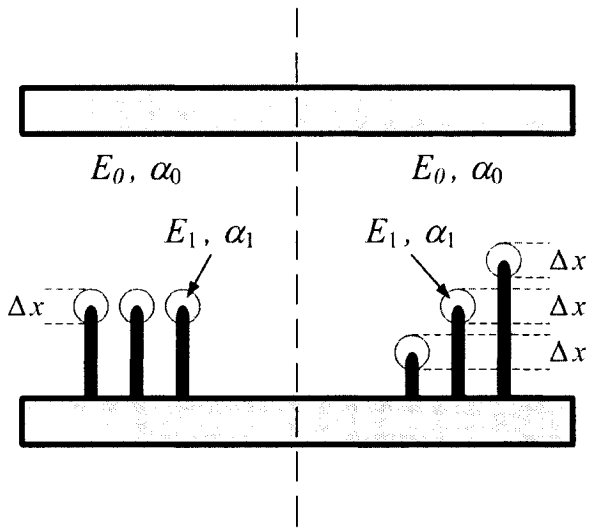

Figure 5.10. Schematic illustration of the distribution of enhanced electric field in the gap, where AuNWs have uniform lengths (at the left), and non-uniform lengths (at the right).

In general, α_0 denotes the Townsend's first coefficient in the gap far from the AuNW tips, where the field strength is the same as applied (E_0). At the vicinity of tips (shown by halos), electric field is intensified (E_1) and the primary electron generation rate takes a different value (α_1). Normally in the low field regime, α is an increasing function of E/P. As a result, $\alpha_1 >> \alpha_0$, and the electron multiplication factor, $M = \exp\left(\int \alpha dx\right)$, is determined by the greatest value (α_1). When the nanowires have uniform lengths, as shown at the left of **Figure 5.10**, E_1 is limited to Δx. In this case, the electron multiplication factor can be roughly estimated as $\int \alpha dx \approx \alpha_1 \Delta x$. For the nonuniform nanowires at the right of **Figure 5.10**, alternatively, we have $\int \alpha dx \approx \sum \alpha_1 \Delta x = 3\alpha_1 \Delta x$.

We therefore conclude that if the nanowires have a wider distribution in their lengths, electron impact ionization breakdown will require a lower applied field strength.

5.1.3. PIC-MCC Simulations

We developed a Particle-in-Cell–Monte-Carlo-Collision (PIC-MCC) model to simulate the discharge and breakdown behavior in our GIS. Our model incorporated the OOPIC-Pro computational tool, a widely used object oriented PIC code [134]. Since OOPIC-PIC is essentially a 2-D simulator, the nanowire array was modeled by parallel rectangular conductive sheets along the 3rd imaginary dimension (z) with unity length. The contribution of primary electrons, secondary electrons, neutrals and ions to the discharge was considered and the simulation was carried out in different pressures to obtain a Paschen-like characteristic. At each pressure, the minimum voltage that led to formation of a streamer from the nanowire tips was recorded as the corresponding V_b.

Figure 5.11 shows the 2-D phase space plots of electrons and Ar+ ions of the first streamer at P = 5 torr. The nanowires were at a potential of V_b = –350 V with respect to the counter electrode. The streamer is formed at t = 42 nsec after the voltage was applied. **Table 5.4** represents the parameters used in simulation, where Δt is the time step, *np2c* is the superparticle ratio, $\Delta t_i/\Delta t$ is the ion subcycle, γ is the secondary electron factor per incident positive ion to the cathode (a typical constant value), U_γ is the threshold ion energy required for secondary electron emission (a typical value obtained from [135]), $U_{\gamma\text{-max}}$ is the maximum allowed energy of the secondary electron, r_κ is the dielectric reflection factor and ε_r is the dielectric constant of the walls. For further explanation on the PIC-MCC parameters, the reader may refer to [134].

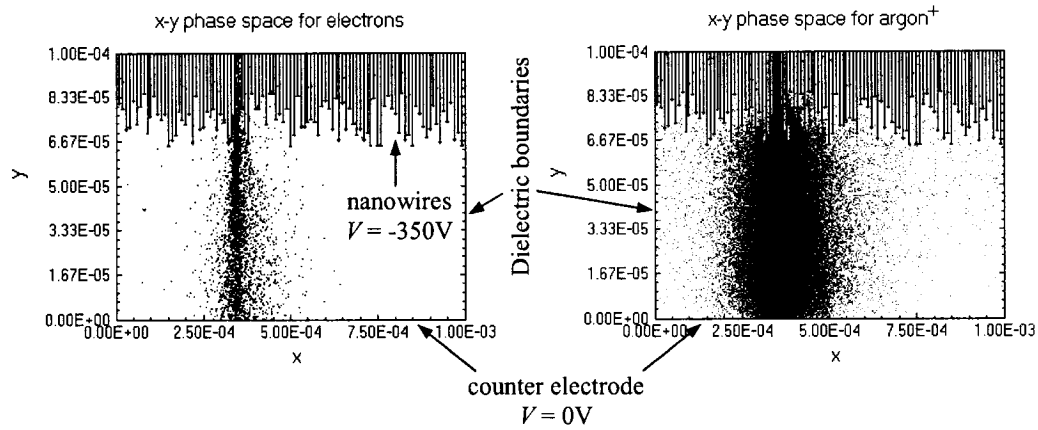

Figure 5.11. Phase space plots of electrons and argon ions of a streamer in our 2-D model for the AuNW based GIS. The nanowires and the counter electrode are separate equipotential boundaries, and the walls are dielectrics. *y* corresponds to the gap spacing and *x* corresponds to the cell width, both are given in meters.

Table 5.4. Parameters employed in our PIC-MCC model for the GIS.

Cell geometry	$x, y\ (d_{gap}), z$	# of cells ($\Delta x = x/m$, $\Delta y = y/n$)	l_{AuNW} (μm)	V_{AuNW}	P (torr)	Δt (s)
Cartesien	1 mm, 100 μm, 1 m	$m = 300$, $n = 100$	25 ± 5	0 - –900V (–50V steps)	0.1 - 760	10^{-14}

np2c	$\Delta t_i/\Delta t$	γ	U_γ	$U_{\gamma\text{-max}}$	r_κ	ε_r
for $P < 10$ torr: $10^7/760$ for $P \geq 10$ torr: $P \times 10^7/760$	10	1.2	12.5 eV	20 eV	0.5	1.0

Since the software does not include circuit implementation, when driving the model with an ideal voltage source it can draw very large currents corresponding to increasing power input. With that positive feedback (increasing current via increasing conductivity of the plasma) it is very difficult to make a DC discharge with an ideal voltage source [136].

Simulations were carried out for different pressures of argon. **Figure 5.12** shows the comparison between breakdown voltages of argon obtained in different devices with our

PIC-MCC simulations. The V_b data of the Modi's CNT based sensor was extracted from the V_b versus concentration curve of argon in Figure 3a of [19], and then mapped into standard *Paschen* coordinates.

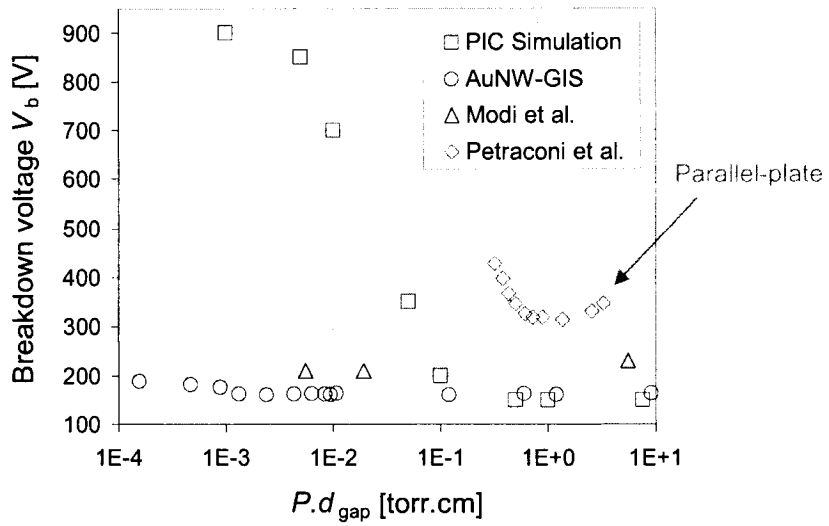

Figure 5.12. Paschen curves of breakdown in Ar, obtained in different gas ionization configurations, along with our PIC-MCC simulation results. The curve for the parallel plate ionization cell was obtained from *Petraconi et al.* in [135].

Apparently, our AuNW-GIS exhibited a similar V_b vs. $P{\cdot}d$ characteristic as the CNT-based sensor. The simulated breakdown voltages on the other hand, followed that of the sensors for $P{\cdot}d_{gap} \geq 0.1$ torr·cm, but increased for the $P{\cdot}d_{gap}$ values below this range, as in uniform field configurations (parallel-plate). We have included the results of a parallel-plate ionization cell of Petraconi et al. [137] for comparison reasons. Such an inconsistency is because our model lacks inclusion of secondary electron emission by incident photons. Photo-ionization of the gas which occurs in conjunction with the other secondary ionization processes is known to have a major impact on the breakdown process in non-uniform fields [28, 29].

5.2. Field Ionization Sensor

SEM studies showed abundance of nanoscale features on the AuNW tips of Sensors #4, 5, 7, 10 and 11, originated from gold clusters that were formed during the impregnation stage. The AuNW tips were also covered by a thin layer of alumina. In addition, the AuNWs of Sensor #10 were terminated by sharp whiskers. All of these devises were tested with the nanowires at the anode and exhibited exceptional low voltage field ionization. The low voltage field ionization was explained based on a combination of geometrical field enhancement and semiconductor-assisted field ionization effects and the technique was employed to detect several gas types and measure their concentration. In the following, we focus on the results obtained on Sensor #10, because of the highest and most stable field-ion current obtained with this device. Any necessary comparisons were made to Sensors #11 which had quite a different AuNW tip nanostructure.

Figure 5.13 represents the room temperature field-ion $I - V$ curves of helium at different pressures. The measurements were carried out using Sensor #10, in a wide range of pressure $0.01 \leq P \leq 100$ torr (corresponding to concentrations of $5\times10^{-7} \leq c_g \leq 5\times10^{-3}$ mol·liter^{-1}).

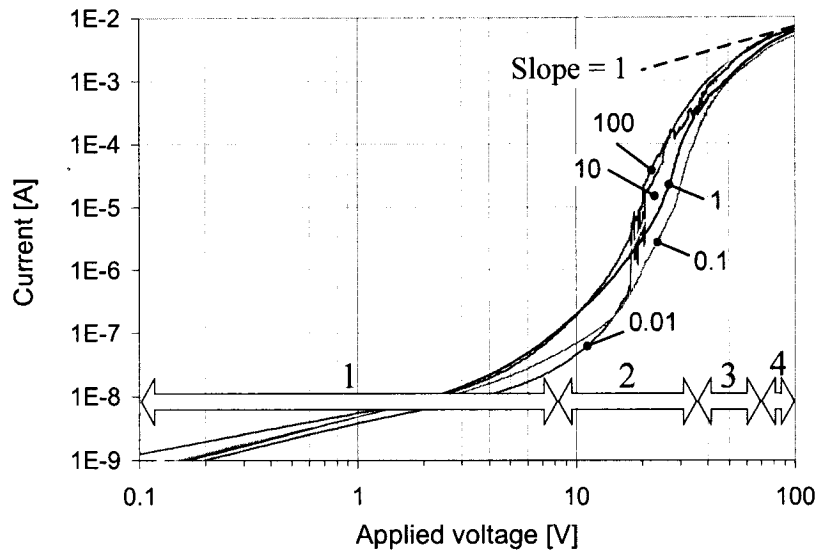

Figure 5.13. Room temperature field-ion $I - V$ curves of helium, measured under different pressures using Sensor #10. The curves identified by the corresponding pressure (in torrs), are plotted in log-log coordinates to distinguish the four different regimes: 1) Ohmic (pre-ionization), 2) Field-limited, 3) Intermediate and 4) Supply-limited. As the field ion characteristic approaches the supply-limited regime, it becomes ohmic and converges to the line with unity slope.

The curves exhibit four distinct zones as indicated by the block arrows. At zone 1, where the field strength is less than the ionization threshold, current flows by the movement of existing radiation-generated electron-ion pairs. The current density is therefore determined by the speed at which carriers travel and corresponds to the ohmic region of discharge explained by (2.3). In the ohmic region, σ_{Gas} is almost independent of the gas type and constant at similar ambient conditions (i.e. temperature, humidity and amount of radiation). Note that the ohmic $I - V$ characteristic always has a unity slope in a full logarithmic scale, no matter how much the conductance is.

When the voltage increases towards zone 2, the ionization is initiated in the field-limited regime and the current increases sharply according to (2.74). As shown in **Figure 5.14**, field-limited current increases with gas pressure (or concentration, if a constant temperature is stipulated). However, the increase is not quite proportional to P (or c_g) as predicted by (2.74), mainly because gas particle accommodation on the tip does not follow the concentration far from it, and/or the effective ϕ increases upon the creation of a multilayer of ad-particles [43, 138]. Note that (2.74) is valid only when the current determined from it is much less than that given by (2.76).

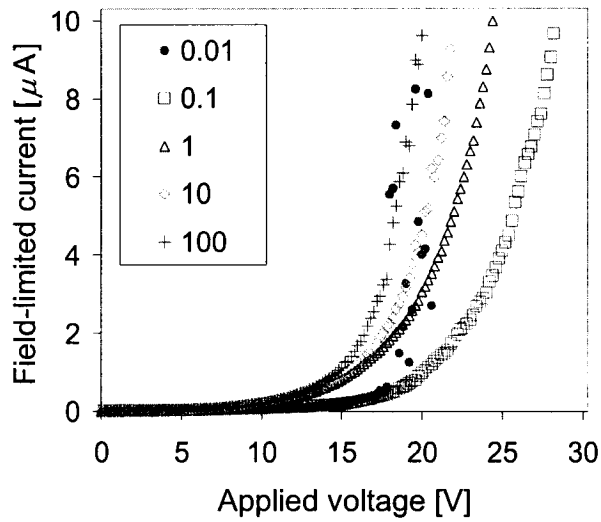

Figure 5.14. Helium ionization currents of Sensor #10 in the field-limited regime at different pressures (in torr).

At intermediate fields (zone 3), the exact ionization mechanism is difficult to quantify. A simplified case would be when the kinetic energy of gas particles rebounding to the tip $(3/2)kT_t$, exceeds the polarization energy V_P. The particles will then escape the ionization region and hoping trajectories from the AuNR shank can be neglected [43, 79]. In this

case, particles approach to the ionization region only from the gas phase, where the arrival rate is determined by the supply function of (2.77).

Zone 4 ($V \gtrsim 70$V) corresponds to the supply-limited ionization regime. According to (2.77), at a constant pressure, the supply function Y is proportional to E via V_P. Therefore, the supply-limited characteristic given by (2.76) shows an ohmic behavior. In this regime, as shown in Fig. 4, the log(I) vs. log (V) curves converged to the unity slope line (dashed), which confirms the ohmic behavior similar to zone 1. **Figure 5.15** shows the supply-limited characteristics under different pressures. It seems that the supply-limited current increases with gas concentration up to the point where it saturates due to accumulation of space charge.

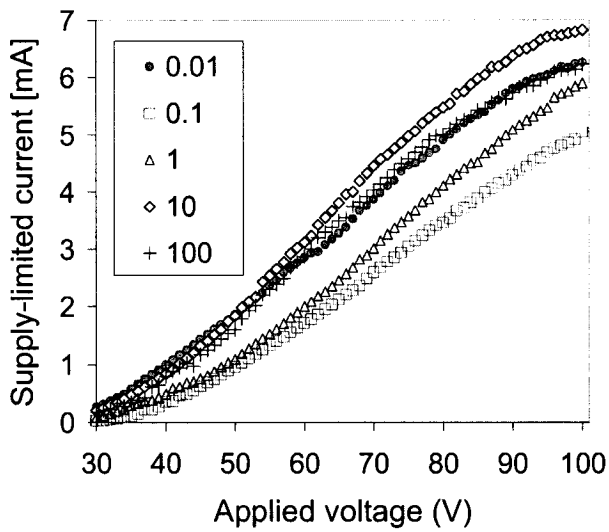

Figure 5.15. Supply-limited ionization currents of helium at different pressures (in torr), measured using Sensor #10.

FI characteristics of Ar, He and N_2 were measured using Sensor #10. **Figure 5.16** shows their $I - V$ curves at $P = 0.01$ torr. It is noticeable that these gases display quite distinctive characteristics, particularly in the field-limited ionization regime. For instance note the field-limited current values of these gases at $V = 10$ V shown at the table in inset of **Figure 5.16**. According to (2.74), and consistent with its higher ionization potential and low polarizability, helium displayed the highest threshold field as it entered the field-limited regime at a higher voltage. The FI current was smaller for He as well, however, the pre-ionization current was noticeably higher in He because of its higher mobility compared to N_2 and Ar.

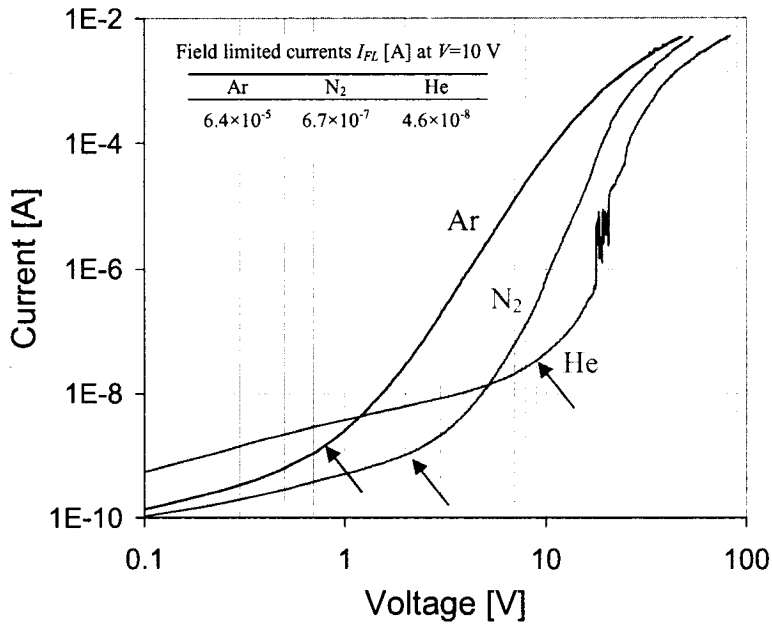

Figure 5.16. Room temperature field ion $I - V$ curves of Ar, N_2, and He, on a log-log scale, measured at $P = 0.01$ torr using Sensor #10. The arrows indicate the approximate ionization threshold points. The table at the inset shows the field-limited ionization currents of the tested gases at $V = 10$ V.

As the voltage further increased, all of the three curves converged together in the supply-limited regime, because in accord to (2.76), the current no longer depends on the ionization energy U_I of the gases in this regime.[2]

The field-ion $I - V$ curves of Sensor #10 and 11, are presented in **Figure 5.17** for comparison. Both curves were obtained at similar conditions (helium, $P = 0.01$ torr, $T =$ 22 °C). Two interesting observations were made: First, the currents at the pre-ionization, field-limited and supply-limited regimes measured using Sensor #10, were about four orders of magnitude higher than the corresponding currents of Sensor #11. The larger current is attributed to a larger effective ionization area ($\sim \pi r_t^2$) of the AuNW tips in Sensor #10 and a greater number of ionization sites (whiskers). Second, both the field-limited and supply-limited thresholds occurred at lower voltages in Sensor #11. This is because the AuNWs of Sensor #11 have sharper features at the edges of their tubular tips, so that the value of β is higher compared to that of Sensor #10. Sharper edges can be interpreted as smaller ionization areas which again reconfirms the first observation. The sudden discharge observed in Sensor #11 at $V = 18$V was due to creation of positive corona or streamer that bridges the gap between the electrodes. As mentioned earlier, the likelihood of avalanche discharge can be reduced by reducing the interelectrode spacing d, because according to Townsend's theory, the electron-impact multiplication factor depends exponentially on d [28-30].

[2] The supply-limited current is however, proportional to $(\alpha_p/m)^{1/2}$, but such a linear dependency is weak compared to the strong exponential dependency of the field-limited current upon U_I.

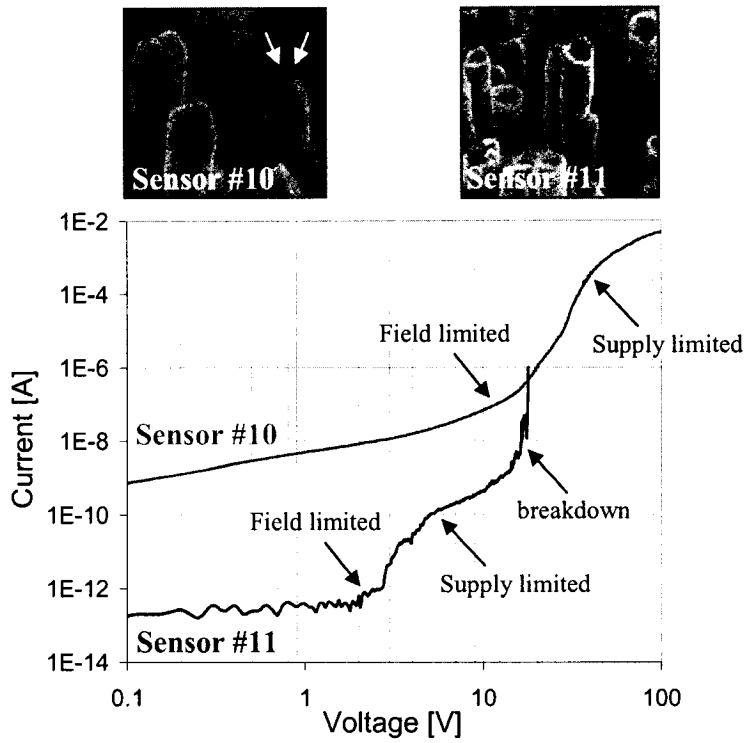

Figure 5.17. Field-ion currents of 0.1 torr helium, measured by Sensors #10 and #11.The threshold points of field-limited and supply-limited regimes are indicated by arrows. Generation of positive corona led to an avalanche breakdown in Sensor #11 at V = 18V. The SEMs show the corresponding AuNW tip nanostructure: Sensor #10 contains many sharp whiskers and Sensor #11 contains tubular tips.

Literature reports a threshold field of $E_i \approx 6.33\times10^8$ V·cm^{-1} for helium ionization using a tungsten specimen [78]. In order to estimate the field enhancement factor of the AuNWs in Sensor #10 and explain the enhanced ionization mechanism, we used the threshold ionization voltage of helium taken from the first knee of the corresponding $I-V$ curve in **Figure 5.16**. ($V_i \approx$ 10V). At such a low threshold voltage, even if we assume that the maximum possible local field is obtained at the ionization sites (i.e. whiskers at the tips of AuNWs), that is the upper limit value given by

$$E_i = E_{loc} = V_i / 5r_t \,, \tag{5.9}$$

an average value of $r_t \approx 0.32$ Å is obtained for the radii of whiskers which is unrealistic because it is even smaller than the atomic radius of gold (1.79 Å) [139]. The conventional field enhancement formalisms that incorporate the applied field in parallel-plate structures such as the one given by (2.39), would predict astonishing geometries as well. In the cylindrical configuration of Sensor #10 for instance, the applied field between the electrodes is $E_{app} \approx 10\text{V}/100\mu\text{m} = 1000\ \text{V}\cdot\text{cm}^{-1}$ (We assumed an average value of $d = 100\mu$m for the gap distance of Sensor #10, as the exact value was not available (see **Table 4.1**). This field strength must be amplified $\beta = E_i/E_{app} = 6.33\times10^5$ times to generate field ionization of helium. According to (5.7), a protrusion aspect ratio as high as $A.R. \approx 7.0\times10^4$ is required. This value appears to be far higher than the features observed in the SEM micrographs at the insets of **Figure 5.17**. Therefore, the actual fields at the ionization sites must be lower than expected. It is concluded that Sensor #10 and Sensor #11, field ionize gas particles at field strengths considerably lower than the reported values on metal tips.

As discussed earlier, we suggest that the ionization is governed by tunneling into the surface states of the residual anodic alumina scales, semiconductive in character, that remain on the AuNW tips due to incomplete dissolution of PAA. Presence of the surface states due to Al and Au contaminants [140], and band bending due to field penetration [34], both increase the effective work function at the surface of the semiconductor with respect to the bulk value (**Figure 2.13**). As a result, field ionization in this case entails lower fields than the values reported for field ionization on metal specimens, although the penetrated field is reduced by a factor of $1/\varepsilon_r$. The exact values of ϕ, ϕ_S, λ_S and therefore, E_i, are difficult to quantify because there is no knowledge on the impurity concentration

of the amorphous alumina after dissolution in NaOH, nor on the nature and quantity of the surface states.

5.3. Field Emission

In addition to the field ionization action, low-voltage electron field emission was observed from the AuNWs of Sensors #4, 5, 7, 10 and 11, when they were negatively biased. The resultant $I - V$ characteristics were plotted in F-N coordinates and the effect of ambient gas on the field emission current was studied. It was concluded that the conduction mechanism is governed by SBFE emission.

Field emission currents of Sensor #10 were measured in helium atmosphere under pressures of P = 0.01, 1, and 100 torr. **Figure 5.18** displays the resultant $I - V$ characteristics in experimental F-N coordinates.

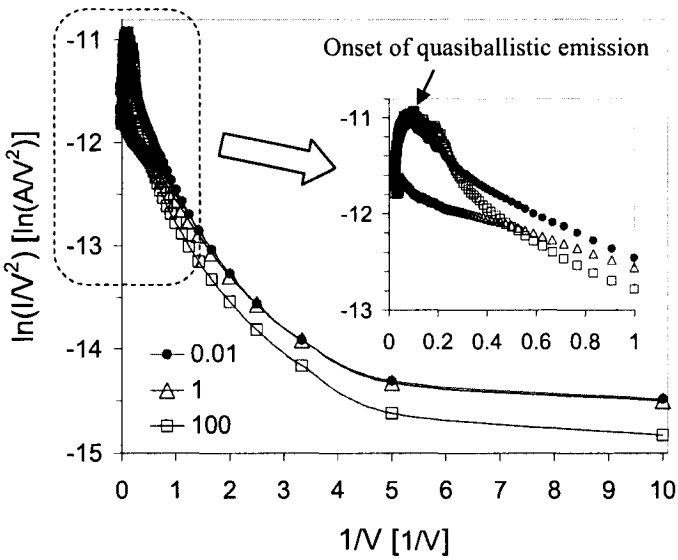

Figure 5.18. F-N plots of the emission currents of Sensor #10 obtained in helium under different pressures: P = 0.01 torr (solid circle), P = 1 torr (triangle), and P = 100 torr (square).

According to (2.59), variations in the slope of an F-N plot S_{FN}, reflect the changes in the emission barrier height, which is the metallic workfunction ϕ, in case of regular F-N emission, or the effective Schottky barrier height ϕ_{Bn}, in case of SBFE emission.

As seen in **Figure 5.18** irrespective of the gas pressure, field emission is initiated at a threshold voltage of V_t = 0.2 V. In addition, in the low field regime ($V_t \leq V \lesssim 1$ V) the slopes did not vary with the gas pressure, suggesting that the height of the barrier through which electrons tunnel is unaffected by gas ad-particles. The curves in the inset show a magnified view of the F-N plots at the high field regime ($V > 1$ V). The turning points indicate the onset of quasiballistic emission (at $V \sim 10$ V) due to disappearance of the Schottky barrier when the modified image force factor becomes greater than one [63, 67, 141]

$$y_{SBFE} = \frac{y}{\varepsilon_r} > 1, \tag{5.10}$$

where y is given by (2.44). The F-N equation no longer applies for over-barrier transport.

Both of the experimental observations – low threshold voltage and the fact that the slopes are independent on the gas pressure – can be accounted for by SBFE emission mechanism. Tunnelling experiments on thin alumina films have shown an asymmetric potential barrier that can be interpreted in terms of the existence of an *n-type* semiconductor phase with negative or close to zero electron affinity (χ) [142-144]. Therefore, a Schottky barrier is created at the interface of gold and the residual alumina on our nanowires. Upon applying a negative bias to the nanowires, a narrow depletion region is formed at the junction, which in turn produces high local electric fields at the interface. At the AuNW ends, because of the tip curvature, the SBFE is combined with

the geometric field enhancement, causing electrons to tunnel the barrier, even under a low bias of 0.2 V.

The nanoparticle aggregates at the tips act as so-called 'supertips' [115] and provide a TSFE effect as discussed in section 2.2.1. We employed the formalism outlined in the last paragraph of section 2.3.2 to estimate the overall value of β for the array of AuNWs. It is imperative to note that in addition to the geometrical field enhancement, this value may also include the enhancement effect of the applied field in the Schottky depletion region. Using (2.38), (2.21), and the parameters shown in **Table 5.5** (ϕ_{Bn} from [145] and m_e/m_0 from [146]). we obtained an average field enhancement factor of $\beta \approx 2.2\times10^6$ and a turn on (threshold) applied field of $E_{app} = V_t/d_{gap} = 0.2\text{V}/100\ \mu\text{m} = 2\times10^{-3}\ \text{V}/\mu\text{m}$. To our knowledge, this value of β is considerably higher than the highest values ever reported earlier for structures pertinent to arrays of high aspect ratio nanowires or CNTs of different kind [58, 60, 66, 73-75, 147-154].

Table 5.5. Parameters used in computing the β factor of AuNWs. S_{FN} is extracted from the plots of **Figure 5.18**.

S_{FN}	V (V)	d_{gap} (μm) Sensor #10	ϕ_{Bn} (eV) gold-alumina interface [145]	m_e/m_0 alumina [146]	ε_r alumina
≈ 1.2	1 – 2	100	3.5	0.5	9.4

Apparently, as shown in the inset of **Figure 5.18**, the slope of the F-N plots, S_{FN}, in the high field regime (particularly at $V \geq 2$), slightly increase prior to disappearance of the barrier. According to (2.24), for an invariant ϕ_{Bn}, S_{FN} is inversely proportional to the field factor ζ, and thus β. It is therefore concluded that the field enhancement effect decreases

at high fields. Such a reduction, beyond any doubt, cannot be mainly due to accumulation of space charge as predicted by Batrakov et al. [155] or the screening effect of positive ions, because it is not a function of pressure. However, it can be attributed to the adverse effect of gas exposure on the electron affinity of the semiconductor [156, 157]. As it can be seen in the energy band diagram of Figure 2.6, if $\chi_{Al_2O_3}$ becomes slightly positive, electrons liberated from the Schottky barrier, cannot leave the semiconductor without energy loss. The decrease in the apparent β, can therefore be accounted for by reduction of the field emission current due to the increase in the electron affinity of the residual alumina. Interestingly, field emission was not observed, when the template was immersed into the NaOH solution for prolonged times, because the alumina was completely dissolved (in Sensors #1, 2, 3, 6, 8, and 9). This experiment confirms the contribution of the thin residual alumina scale, *n-type* in character, to the resultant $I - V$. We were not equipped to directly measure $\chi_{Al_2O_3}$, by photoemission spectroscopy or any other similar technique.

Chapter 6

Conclusions, Contributions and Future work

6.1. Conclusions and Contributions.

In this work, we fabricated and successfully tested a new generation of miniaturized field-effect gas sensors that work by two different mechanisms: First, by fingerprinting the ionization breakdown voltages, and second, by measuring the tunneling field-ionization currents of the unknown gas species.

Freestanding arrays of gold nanowires were incorporated as field-amplifying elements to reduce the gaseous breakdown voltages. Non-uniform electric fields generated at the nanowire tips, not only hasten the breakdown process, but also decrease the dependence of the breakdown voltage upon the gas concentration (pressure). As a result, the curves of breakdown voltage against gas concentration were almost flat within a certain range. Such a characteristic is desirable for an ionization gas sensor, in a sense that, the discrimination of different gases can be performed irrespective of their pressure.

The effective field enhancement factor of the nanowires was estimated by operating the sensor in the pre-breakdown dark discharge mode and comparing the currents with that of a nanowireless parallel-plate cell. The aspect ratio of nanowires was computed and the result showed good agreement with SEM observations. Because of the nature of the field distribution in the gap, no quantitative relationship could be established between the field enhancement factor of the nanowires and the breakdown voltage.

We used a tailored version of the template-assisted electrochemical technique to fabricate our freestanding gold nanowires. The technological hurdle of preventing the nanowires from collapse was surmounted by reducing the number of template pores available for electrochemical nucleation. Polystyrene microspheres were introduced into the template pores in a controlled manner, thus blocking them partially.

To simulate the breakdown behavior in our sensor, a 2-D PIC-MCC model was developed. The model successfully predicted breakdown voltages at pressures above a certain value ($P \cdot d_{gap} \geq 0.1$ torr·cm). The simulated breakdown voltages, increased at lower pressures, as in uniform fields, because such a model does not take account of secondary electron generation due to photoionization in the gap.

It was shown that a particular set of AuNW arrays were able to field-ionize several test gases at exceptionally low voltages (sub-10V). In this case, the apparent field enhancement factors were far higher that the values predicted from the nanowire geometry. It was concluded that these AuNWs, while terminated with nanoscale features at their tips, contained a residual amorphous alumina layer due to incomplete dissolution of the template. Field penetration and band bending at the surface of this layer and the existence of surface states, facilitate tunneling even if there is no inversion. The tunneling probability in this case is increased compared to field ionization on metals, and the threshold ionization voltage is considerably reduced. Presence of amorphous alumina was confirmed by the surface Raman spectra.

The resulting distinct field-ion currents, at constant applied voltage, were used as signatures to identify the unknown gas type. The $I - V$ characteristic in the field-limited

regime showed pressure dependence, though such dependence could not be precisely quantified.

In addition, low-voltage electron field emission form the same set of AuNWs was observed. The currents, gathered at different gas pressures, were plotted in Fowler-Nordheim coordinates. The low tunneling threshold voltages, as well as the independence of the current from gas pressure was described based on the Schottky barrier field enhancement theory which confirms the presence of a semiconductive alumina layer on the metallic tips. An effective field enhancement factor for the AuNWs that includes the contributions of both geometric and Schottky-barrier field enhancement effects, was computed.

Upon successful fabrication, test and characterization of the proposed structure in commercially available alumina templates, the first nanowire based gas ionization sensor compatible with microelectronics is introduced. The contributions of this research are summarized in the list below:

- Freestanding gold nanowires with aspect ratios as high as 180 were synthesized. In order to avoid bundling and collapse of the nanowires, the density of the available pores was reduced by partially blocking them, using polystyrene microspheres. We also fabricated nanowires with nanoscale gold particles at their tips to boost the electric field enhancement factor.
- Gas ionization sensors were fabricated by incorporating the nanowire array films at one of the electrodes of a parallel-plate ionization cell.

- Sensors containing regular gold nanowires were used to measure the breakdown voltages of several gas species in a certain range of pressure. The breakdown voltages obtained were reduced compared to uniform field conditions and did not vary significantly with gas pressure.
- The effect of electrode polarity on the pre-breakdown discharge current and the breakdown voltage was studied. The breakdown voltages were smaller for the cathode-AuNW device.
- Sensors fabricated using nanowires with nanoscale features, displayed low-voltage field-ionization. This phenomenon was employed as a second approach to identify unknown gases.
- The Schottky barrier field enhancement model was used in conjunction with Fowler-Nordheim formalism to compute an effective value for the field enhancement factor of the nanowires containing residual alumina scales.

6.2. Future Work

The concept of using arrays of micro- or nano-protrusions to detect gases based on their ionization characteristics, can be explored further. Innovative devices can be developed, that use advanced materials and modern nanolithography and nanopatterning techniques to form more efficient field-intensifying elements. We suggest that the results of this work be extended and investigated in following topics:

- Study the breakdown and ionization behavior of the GIS in gas mixtures.
- Towards detection of gas combinations, a number of GISs that contain nanowires with different aspect ratios can be fabricated. These GIS, each sensitive to a

particular gas type, can then be interconnected in an array to enable detection of gas .mixtures.

- Deposit diamond as a robust NEA material on nanowire tips to develop Schottky barrier emitter arrays, and study the effect of gas exposure on the field emission current.
- Carefully investigate and quantify the semiconductor properties (e.g. electron affinity) of the amorphous alumina remaining from PAA templates after treatment with NaOH.

Bibliography

[1] A. Mandelis and C. Christofides, *Physics, Chemistry and Technology of Solid State Gas Sensor Devices.* New York: John Wiley & Sons, 1993.

[2] S. J. Gentry and T. A. Jones, "The role of catalysis in solid-state gas sensors," *Sensors and Actuators,* vol. 10, pp. 141-163, 1986.

[3] Q. Wan, Q. H. Li, Y. J. Chen, T. H. Wang, X. L. He, J. P. Li, and C. L. Lin, "Fabrication and ethanol sensing characteristics of ZnO nanowire gas sensors," *Appl. Phys. Lett.,* vol. 84, pp. 3654-3656, 2004.

[4] Z. Fan, D. Wang, P.-C. Chang, W.-Y. Tseng, and J. G. Lu, "ZnO nanowire field-effect transistor and oxygen sensing property," *Appl. Phys. Lett,* vol. 85, pp. 5923-5925, 2004.

[5] Z. Liu, T. Yamazaki, Y. Shen, T. Kikuta, N. Nakatani, and T. Kawabata, "Room temperature gas sensing of p-type TeO_2 nanowires," *Appl. Phys. Lett,* vol. 90, pp. 173119 – 1-3, 2007.

[6] E. Comini, S. Bianchi, G. Faglia, G. Sberveglieri, J. Arbiol, J. R. Morante, and L. Zanotti, "Tin and indium oxide nanocrystals based gas sensors characterization," *Proc. IEEE Sensors Conf.,* 2005, pp. 1330-1334.

[7] A. Z. Sadek, W. Wlodarski, K. Kalantar-zadeh, and S. Choopun, "ZnO Nanobelt Based Conductometric H_2 and NO_2 Gas Sensors," *Proc. IEEE Sensors Conf.*, 2005, pp. 1326-1329.

[8] S. Iijima, "Helical microtubules of graphitic carbon," *Nature,* vol. 354, pp. 56-58, 1991.

[9] S. G. Wang, Q. Zhang, D. J. Yang, P. J. Sellin, and G. F. Zhong, "Multi-walled carbon nanotube-based gas sensors for NH_3 detection," *Diam. Relat. Mater.,* vol. 13, pp. 1327-1332, 2004.

[10] A. Chambers, C. Park, R. T. K. Baker, and N. M. Rodriguez, "Hydrogen Storage in Graphite Nanofibers," *J. Phys. Chem. B,* vol. 102, pp. 4253-4256, 1998.

[11] P. G. Collins, K. Bradley, M. Ishigami, and A. Zettl, "Extreme Oxygen Sensitivity of Electronic Properties of Carbon Nanotubes," *Science,* vol. 287, pp. 1801-1804, March 10, 2000.

[12] A. C. Dillon, K. M. Jones, T. A. Bekkedahl, C. H. Kiang, D. S. Bethune, and M. J. Heben, "Storage of hydrogen in single-walled carbon nanotubes," *Nature,* vol. 386, pp. 377-379, 1997.

[13] G. U. Sumanasekera, C. K. W. Adu, S. Fang, and P. C. Eklund, "Effects of Gas Adsorption and Collisions on Electrical Transport in Single-Walled Carbon Nanotubes," *Phys. Rev. Lett.,* vol. 85, pp. 1096-1099, 2000.

[14] A. Zahab, L. Spina, P. Poncharal, and C. Marlière, "Water-vapor effect on the electrical conductivity of a single-walled carbon nanotube mat," *Phys. Rev. B,* vol. 62, pp. 10000-10003, 2000.

[15] L. Valentini, I. Armentano, J. M. Kenny, C. Cantalini, L. Lozzi, and S. Santucci, "Sensors for sub-ppm NO_2 gas detection based on carbon nanotube thin films," *Appl. Phys. Lett,* vol. 82, pp. 961-963, 2003.

[16] O. K. Varghese, P. D. Kichambre, D. Gong, K. G. Ong, E. C. Dickey, and C. A. Grimes, "Gas sensing characteristics of multi-wall carbon nanotubes," *Sensors and Actuators B: Chemical,* vol. 81, pp. 32-41, 2001.

[17] M. J. Madau and S. R. Momson, *Chemical sensing with solid state devices.* San Diego, CA: Academic Press Inc., 1989.

[18] S. Kim, "CNT Sensors for Detecting Gases with Low Adsorption Energy by Ionization," *Sensors,* vol. 6, pp. 503-513, 2006.

[19] A. Modi, N. Koratkar, E. Lass, B. Wei, and P. M. Ajayan, "Miniaturized gas ionization sensors using carbon nanotubes," *Nature,* vol. 424, pp. 171-174, 2003.

[20] ____, *Flame ionization detector, product data sheet* [Online]. SRI Instruments, Torrance, CA, Available: http://www.srigc.com/FID.pdf as of 8/29/2007.

[21] S. C. Terry, J. H. Jerman, and J. B. Angell, "A gas chromatographic air analyzer fabricated on a silicon wafer," *IEEE Trans. Electron Devices,* vol. 26, pp. 1880-1886, 1979.

[22] Y. Zhang, J. Liu, X. Li, and C. Zhu, "The structure optimization of the carbon nanotube film cathode in the application of gas sensor," *Sensors and Actuators A: Physical,* vol. 128, pp. 278-289, 2006.

[23] Z. Yong, L. Junhua, L. Xin, T. Xiaojun, and Z. Changchun, "Study of improving identification accuracy of carbon nanotube film cathode gas sensor," *Sensors and Actuators A: Physical,* vol. 125, pp. 15-24, 2005.

[24] Z. Yong, L. Junhua, L. Xin, D. Juying, L. Weihua, H. Yongning, and Z. Changchun, "Study of gas sensor with carbon nanotube film on the substrate of porous silicon," *Proc. IEEE IVMC*, 2001, pp. 13-14.

[25] C. Xing, H. Zhongying, H. Jiarui, L. Jinhuai, and K. Mingguang, "Gas ionization sensors using well-aligned MWCNT arrays grown in porous AAO template," *Proc. IEEE ICIA*, Hong Kong and Macau, China, 2005, pp. 290-293.

[26] Z. Hou, D. Xu, and B. Cai, "Ionization gas sensing in a microelectrode system with carbon nanotubes," *Appl. Phys. Lett,* vol. 89, pp. 213502-1 - 213502-3, 2006.

[27] G. Hui, L. Wu, M. Pan, Y. Chen, T. Li, and X. Zhang, "A novel gas-ionization sensor based on aligned multi-walled carbon nanotubes," *Meas. Sci. Technol.,* vol. 17, pp. 2799-2805, 2006.

[28] A. M. Howatson, *An introduction to gas discharges*, 2nd ed. Oxford: Pergamon Press, 1976.

[29] J. M. Meek and J. D. Craggs, *Electrical Breakdown of Gases*. New York: John Wiley & Sons, 1978.

[30] M. Abdel-Salam, H. Anis, A. El-Morshedy, and R. Radwan, *High Voltage Engineering–Theory and Practice*, 2nd ed. New York: Dekker, 2000.

[31] M. J. Madou and S. R. Morrison, "High-field operation of submicrometer devices at atmospheric pressure," in *Solid-State Sensors and Actuators, 1991. Digest of*

Technical Papers, TRANSDUCERS '91., 1991 International Conference on, 1991, pp. 145-149.

[32] B. Ghodsian, M. Parameswaran, and M. Syrzycki, "Gas detector with low-cost micromachined field ionization tips," *IEEE Electron Device Lett.*, vol. 19, pp. 241-243, 1998.

[33] B. Ghodsian, "Development of Micromachined Field Ionization Tips for Use As An Integrated Gas Detector In a Micromachined Gas Chronlatogaphy System," Ph.D. dissertation, School of Engineering Science, Simon Fraser University, Vancouver, BC, Canada, 1997.

[34] M. K. Miller, A. Cerezo, M. G. Hetherington, and G. D. W. Smith, *Atom Probe Field Ion Microscopy*. New York: Oxford, 1996.

[35] J. Zhang, N. Xi, H. Chan, and G. Li, "Single Carbon Nanotube Based Ion Sensor for Gas Detection," *Proc. IEEE-NANO,* 2006, pp. 790-793.

[36] P. Forrer, F. Schlottig, H. Siegenthaler, and M. Textor, "Electrochemical preparation and surface properties of gold nanowire arrays formed by the template technique," *J. Appl. Electrochem.*, vol. 30, pp. 533-541, 2000.

[37] L. Dusan, G. S. Joe, G. M. James, and H. V. Nicolas, "Fabrication of gold nanorod arrays by templating from porous alumina," *Nanotechnology,* vol. 16, pp. 2275-2281, 2005.

[38] C. A. Foss, G. L. Hornyak, J. A. Stockert, and C. R. Martin, "Template-Synthesized Nanoscopic Gold Particles: Optical Spectra and the Effects of Particle Size and Shape," *J. Phys. Chem.*, vol. 98, pp. 2963-2971, 1994.

[39] A. Huczko, "Template-based synthesis of nanomaterials," *Appl. Phys. A: Mater. Sci. Process.*, vol. 70, pp. 365-376, 2000.

[40] R. Liu, "Synthesis, characterization and properties of nanostructured materials by template-directed method," M.Sc. thesis, Dept. of Chemistry: Univ. of New Orleans, New Orleans, LA, 2004.

[41] J. C. H. a. C. R. Martin, "A general template-based method for the preparation of nanomaterials," *J. Mater. Chem.*, vol. 7, pp. 1075-1087, 1997.

[42] R. G. Longwitz, "Study of Gas Ionization in a Glow Discharge and Development of a Micro Gas Ionizer for Gas Detection and Analysis." Ph.D. dissertation, EPFL, Lausanne, Switzerland, 2004.

[43] R. Gomer, *Field emission and Field ionization*. Cambridge: Harvard Univ. Press, 1961.

[44] T. T. Tsong, *Atom-Probe Field Ion Microscopy*. Cambridge: Harvard Univ. Press, 1990.

[45] T. Sakurai, A. Sakai, and H. W. Pickering, *Atom-Probe Field Ion Microscopy and Its Applications*. San Diego: Academic Press Inc., 1989.

[46] P. G. Slade and E. D. Taylor, "Electrical breakdown in atmospheric air between closely spaced (0.2 μm - 40 μm) electrical contacts," *IEEE Trans. Compon. Packag. Technol.*, vol. 25, pp. 390-396, 2002.

[47] C.-H. Chen, J. A. Yeh, and P.-J. Wang, "Electrical breakdown phenomena for devices with micron separations," *J. Micromech. Microeng.*, vol. 16, pp. 1366-1373, 2006.

[48] J. M. Torres and R. S. Dhariwal, "Electric field breakdown at micrometre separations," *Nanotechnology*, vol. 10, pp. 102-107, 1999.

[49] N. Zouache and A. Lefort, "Electrical breakdown of small gaps in vacuum," *IEEE Trans. Dielectr. Electr. Insul.*, vol. 4, pp. 358-364, 1997.

[50] B. Held, N. Soulem, R. Peyrous, and N. Spyrou, "Self-Sustained Conditions in Inhomogeneous Fields," *Journal de Physique III*, vol. 7, pp. 2059-2077, 1997.

[51] A. E. D. Heylen, "Ionization coefficients and sparking voltages in argon and argon-ethane mixtures," *J. Phys. D: Appl. Phys.*, vol. 1, pp. 179-188, 1968.

[52] N. Spyrou, R. Peyrous, N. Soulem, and B. Held, "Why Paschen's law does not apply in low-pressure gas discharges with inhomogeneous fields," *J. Phys. D: Appl. Phys.*, vol. 28, pp. 701-710, 1995.

[53] T. Sakurai and E. W. Müller, "Field Calibration Using the Energy Distribution of Field Ionization," *Phys. Rev. Lett.,* vol. 30, pp. 532-535, 1973.

[54] R. G. Forbes, C. J. Edgcombe, and U. Valdre, "Some comments on models for field enhancement," *Ultramicroscopy,* vol. 95, pp. 57-65, 2003.

[55] F. H. Read and N. J. Bowring, "Field enhancement factors of random arrays of carbon nanotubes," *Nucl. Instrum. Methods Phys. Res. Sect. A,* vol. 519, pp. 305-314, 2004.

[56] H. C. Miller, "Change in Field Intensification Factor beta of an Electrode Projection (Whisker) at Short Gap Lengths," *J. Appl. Phys.,* vol. 38, pp. 4501-4504, 1967.

[57] C. J. Edgcombe and U. Valdre, "The enhancement factor and the characterization of amorphous carbon field emitters," *Solid-State Electronics,* vol. 45, pp. 857-863, 2001.

[58] A. Wisitsorat-at, "Micropatterned diamond vacuum field emission devices," Ph.D. dissertation, Dept. Elect. Eng., Vanderbilt Univ., Nashville, TN, 2002.

[59] E. I. Givargizov, V. V. Zhirnov, A. N. Stepanova, E. V. Rakova, A. N. Kiselev, and P. S. Plekhanov, "Microstructure and field emission of diamond particles on silicon tips," *Appl. Surf. Sci.,* vol. 87-88, pp. 24-30, 1995.

[60] E. I. Givargizov, V. V. Zhirnov, A. V. Kuznetsov, and P. S. Plekhanov, "Cold emission from the single-crystalline microparticle of diamond on a Si tip," *Proc. 8th IEEE-IVMC*, Portland, OR, 1996, pp. 2030-2033.

[61] M. Sedlacek, *Electron Physics of Vacuum and Gaseous Devices*. New York: John Wiley & Sons, 1996.

[62] S. M. Sze and K. K. Ng, *Physics of semiconductor devices*, 3rd ed. New York: Wiley Interscience, 2007.

[63] R. G. Forbes, "Use of a spreadsheet for Fowler-Nordheim equation calculations," *Proc. 11th IEEE-IVMC*, Asheville, NC, 1999, pp. 534-541.

[64] R. E. Burgess, H. Kroemer, and J. M. Houston, "Corrected Values of Fowler-Nordheim Field Emission Functions $v(y)$ and $s(y)$," *Phys. Rev.,* vol. 90, p. 515, 1953.

[65] E. V. Albano and H. O. Mártin, "Depolarization effects due to the interaction between adsorbed dipoles on stepped surfaces," *Phys. Rev. B,* vol. 38, pp. 7932-7939, 1988.

[66] J. P. Singh, F. Tang, T. Karabacak, T. M. Lu, and G. C. Wang, "Enhanced cold field emission from <100> oriented β-W nanoemitters, *J. Vac. Sci. Technol. B: Microelectronics and Nanometer Structures,* vol. 22, pp. 1048-1051, 2004.

[67] P. Lerner, P. H. Cutler, and N. M. Miskovsky, "Theoretical analysis of field emission from a metal diamond cold cathode emitter," *J. Vac. Sci. Technol. B: Microelectronics and Nanometer Structures,* vol. 15, pp. 337-342, 1997.

[68] E. Segré, "E. Fermi, Nuovo Cimento 11, 157 (1934)," in *The Collected Papers of Enrico Fermi.* vol. 1 Chicago: Univ. of Chicago Press, 1962, p. 706.

[69] J. C. T. M. W. Geis, and T. M. Lyszczarz, "Fabrication and Theory of Diamond Emitters," *Lincoln Lab. Journal,* vol. 8, pp. 161-172, 1995.

[70] N. N. E. M. W. Geis, K. E. Krohn, J. C. Twichell, T. M. Lyszczarz, R. Kalish, J. A. Greer, and M. D. Tabat, "Theory and Experimental Results of a New Diamond Surface-Emission Cathode," *Lincoln Lab. Journal,* vol. 10, pp. 3-18, 1997.

[71] M. W. Geis, N. N. Efremow, K. E. Krohn, J. C. Twichell, T. M. Lyszczarz, R. Kalish, J. A. Greer, and M. D. Tabat, "A new surface electron-emission mechanism in diamond cathodes," *Nature,* vol. 393, pp. 431-435, 1998.

[72] V. V. Zhirnov, G. J. Wojak, W. B. Choi, J. J. Cuomo, and J. J. Hren, "Wide band gap materials for field emission devices," in *The 43rd national symposium of the American Vacuum Society*, Philadelphia, PA, 1997, pp. 1733-1738.

[73] A. F. Myers, S. M. Camphausen, J. J. Cuomo, J. J. Hren, J. Liu, and J. Bruley, "Characterization of amorphous carbon coated silicon field emitters," *Proc. 8th IEEE-IVMC*, Portland, OR, 1996, pp. 2024-2029.

[74] J. T. T. Chih-Chiang Hua, C.S. Huang, B.R. Huang, J. Sung, "The electron emitting characteristics of amorphous diamond deposited on the Copper nanowires," *Proc. IEEE ICSS*, 2005, pp. 1264-1267.

[75] M. Chhowalla, C. Ducati, N. L. Rupesinghe, K. B. K. Teo, and G. A. J. Amaratunga, "Field emission from short and stubby vertically aligned carbon nanotubes," *Appl. Phys. Lett,* vol. 79, pp. 2079-2081, 2001.

[76] M. S. Chung, B. G. Yoon, P. H. Cutler, and N. M. Miskovsky, "Theoretical analysis of enhanced field electron emission from the triple junction," *Proc. 16th IEEE-IVMC*, 2003, pp. 121-122.

[77] K. Okano, S. Koizumi, S. R. P. Silva, and G. A. J. Amaratunga, "Low-threshold cold cathodes made of nitrogen-doped chemical-vapour-deposited diamond," *Nature,* vol. 381, pp. 140-141, 1996.

[78] D. G. Brandon, "The resolution of atomic structure: recent advances in the theory and development of the field ion microscope," *Brit. J. Appl. Phys.,* vol. 14, pp. 474-484, 1963.

[79] X. Liu and J. Orloff, "Analytical model of a gas phase field ionization source," *J. Vac. Sci. Technol. B: Microelectronics and Nanometer Structures,* vol. 23, pp. 2816-2820, 2005.

[80] T. Sakurai and E. W. Muller, "Field calibration using the energy distribution of a free-space field ionization," *J. Appl. Phys.,* vol. 48, pp. 2618-2625, 1977.

[81] H. D. Beckey, "Experimental techniques in field ionisation and field desorption mass spectrometry," *J. Phys. E: Scientific Instruments,* vol. 12, pp. 72-83, 1979.

[82] E. W. Müller and K. Bahadur, "Field Ionization of Gases at a Metal Surface and the Resolution of the Field Ion Microscope," *Phys. Rev.,* vol. 102, pp. 624-634, 1956.

[83] J. H. Orloff and L. W. Swanson, "Study of a field-ionization source for microprobe applications," *J. Vac. Sci. Technol.,* vol. 12, pp. 1209-1213, 1975.

[84] T. T. Tsong, "Field penetration and band bending for semiconductor of simple geometries in high electric fields," *Surf. Sci.*, vol. 85, pp. 1-18, 1979.

[85] L. Ernst, "On the field penetration into semiconductors in the field ion microscope," *Surf. Sci.*, vol. 85, pp. 302-308, 1979.

[86] L. Ernst and J. H. Block, "Field ion microscopy of germanium: Field ionization and surface states," *Surf. Sci.*, vol. 49, pp. 293-309, 1975.

[87] Y. Ohno, S. Nakamura, T. Adachi, and T. Kuroda, "Field-ion microscopy of GaAs and GaP," *Surf. Sci.*, vol. 69, pp. 521-532, 1977.

[88] G. C. Dousmanis and J. R. C. Duncan, "Calculations on the Shape and Extent of Space Charge Regions in Semiconductor Surfaces," *J. Appl. Phys.*, vol. 29, pp. 1627-1629, 1958.

[89] R. Seiwatz and M. Green, "Space Charge Calculations for Semiconductors," *J. Appl. Phys.*, vol. 29, pp. 1034-1040, 1958.

[90] T. Sakurai, R. J. Culbertson, and A. J. Melmed, "Anomalous field evaporation of silicon," *Surf. Sci.*, vol. 78, pp. L221-L226, 1978.

[91] H. Y. Peng, X. T. Zhou, H. L. Lai, N. Wang, and S. T. Lee, "Microstructure observations of silicon carbide nanorods," *Mater. Res. Soc.*, vol. 15, pp. 2020-2026, 2000.

[92] M. Tsuji, M. Hashimoto, Y. Nishizawa, and T. Tsuji, "Synthesis of gold nanorods and nanowires by a microwave-polyol method," *Mater. Lett.*, vol. 58, pp. 2326-2330, 2004.

[93] B. S. Doyle, S. Datta, M. Doczy, S. Hareland, B. Jin, J. Kavalieros, T. Linton, A. Murthy, R. Rios, and R. Chau, "High performance fully-depleted tri-gate CMOS transistors," *IEEE Electron Device Lett.*, vol. 24, pp. 263-265, 2003.

[94] S. Cristoloveanu and S. S. Li, *Electrical Characterization of Silicon-On-Insulator Materials and Devices*: Kluwer Academic Publishers, 1995.

[95] T. Ernst, S. Cristoloveanu, G. Ghibaudo, T. Ouisse, S. Horiguchi, Y. Ono, Y. Takahashi, and K. Murase, "Ultimately thin double-gate SOI MOSFETs," *IEEE Trans. Electron Devices,* vol. 50, pp. 830-838, 2003.

[96] P. Chang, Z. Fan, D. Wang, W. Tseng, W. Chiu, J. Hong, and J. G. Lu, "ZnO Nanowires Synthesized by Vapor Trapping CVD Method," *Chem. Mater.,* vol. 16, pp. 5133-5137, 2004.

[97] Q. Yang, J. Sha, X. Ma, and D. Yang, "Synthesis of NiO nanowires by a sol-gel process," *Mate. Lett.,* vol. 59, pp. 1967-1970, 2005.

[98] L. Vayssieres, "Growth of Arrayed Nanorods and Nanowires of ZnO from Aqueous Solutions," *Adv. Mater.,* vol. 15, pp. 464-466, 2003.

[99] ____, *Nuclepore® track-etched polycarbonate membranes, product data sheet* [Online], Whatman Inc., Florham Park, NJ: Available: http://www.whatman.com/products/?pageID=7.57.291.22 as of 8/29/2007.

[100] ____, *Anopore® inorganic membranes, product datasheet* [Online], Whatman Inc., Florham Park, NJ, Available: http://www.whatman.com/products/?pageID=7.57.293 as of 8/29/2007.

[101] G. Riveros, S. Green, A. Cortes, G. H, Gomez, R. E. Marotti, and E. A. Dalchiele, "Silver nanowire arrays electrochemically grown into nanoporous anodic alumina templates," *Nanotechnology,* vol. 17, p. 561, 2006.

[102] M. J. Zheng, L. D. Zhang, G. H. Li, and W. Z. Shen, "Fabrication and optical properties of large-scale uniform zinc oxide nanowire arrays by one-step electrochemical deposition technique," *Chem. Phys. Lett.,* vol. 363, pp. 123-128, 2002.

[103] R. M. Penner and C. R. Martin, "Preparation and electrochemical characterization of ultramicroelectrode ensembles," *Anal. Chem.,* vol. 59, pp. 2625-2630, 1987.

[104] M. J. Tierney and C. R. Martin, "Transparent metal microstructures," *J. Phys. Chem.,* vol. 93, pp. 2878-2880, 1989.

[105] C. A. Foss, M. J. Tierney, and C. R. Martin, "Template synthesis of infrared-transparent metal microcylinders: comparison of optical properties with the predictions of effective medium theory," *J. Phys. Chem.*, vol. 96, pp. 9001-9007, 1992.

[106] C. A. Foss, G. L. Hornyak, J. A. Stockert, and C. R. Martin, "Optical properties of composite membranes containing arrays of nanoscopic gold cylinders," *J. Phys. Chem.*, vol. 96, pp. 7497-7499, 1992.

[107] Y. Li, G. W. Meng, L. D. Zhang, and F. Phillipp, "Ordered semiconductor ZnO nanowire arrays and their photoluminescence properties," *Appl. Phys. Lett,* vol. 76, pp. 2011-2013, 2000.

[108] Z. Wang, Y. K. Su, and H. L. Li, "AFM study of gold nanowire array electrodeposited within anodic aluminum oxide template," *Appl. Phys. A: Mater. Sci. Proc.*, vol. 74, pp. 563-565, 2002.

[109] M. Tian, J. Wang, J. Kurtz, T. E. Mallouk, and M. H. W. Chan, "Electrochemical Growth of Single-Crystal Metal Nanowires via a Two-Dimensional Nucleation and Growth Mechanism," *Nano Lett.*, vol. 3, pp. 919-923, 2003.

[110] J. Bao, Z. Xu, J. Hong, X. Ma, and Z. Lu, "Fabrication of cobalt nanostructures with different shapes in alumina template," *Scripta Materialia,* vol. 50, pp. 19-23, 2004.

[111] Y. Liang, C. Zhen, D. Zou, and D. Xu, "Preparation of Free-Standing Nanowire Arrays on Conductive Substrates," *J. Am. Chem. Soc.*, vol. 126, pp. 16338-16339, 2004.

[112] M. Paunovic and M. Schlesinger, *Fundamentals of Electrochemical Deposition.* New York: Wiley, 1998.

[113] M. Schlesinger and M. Paunovic, *Modern Electroplating*, 4th ed. New York: Wiley, 2000.

[114] D. M. Davis, "ELECTRODEPOSITION OF MAGNETIC NANOWIRES AND NANOTUBES," M.Sc. thesis, Dept. Chem. Eng., Louisiana State Univ., Baton Rouge, LA, 2005.

[115] A. Knoblauch, C. Wilbertz, T. Miller, and S. Kalbitzer, "Field electron emission properties of a supertip," *J. Phys. D: Appl. Phys.*, vol. 29, pp. 470-473, 1996.

[116] P. Goring, E. Pippel, H. Hofmeister, R. B. Wehrspohn, M. Steinhart, and U. Gosele, "Gold/Carbon Composite Tubes and Gold Nanowires by Impregnating Templates with Hydrogen Tetrachloroaurate/Acetone Solutions," *Nano Lett.*, vol. 4, pp. 1121-1125, 2004.

[117] P. Claus and H. Hofmeister, "Electron Microscopy and Catalytic Study of Silver Catalysts: Structure Sensitivity of the Hydrogenation of Crotonaldehyde," *J. Phys. Chem. B,* vol. 103, pp. 2766-2775, 1999.

[118] H. Shi, L. Zhang, and W. Cai, "Preparation and optical absorption of gold nanoparticles within pores of mesoporous silica," *Mate. Res. Bull.*, vol. 35, pp. 1689-1695, 2000.

[119] C. Kan, W. Cai, Z. Li, G. Fu, and L. Zhang, "Reduction effect of pore wall and formation of Au nanowires inside monolithic mesoporous silica," *Chem. Phys. Lett.*, vol. 382, pp. 318-324, 2003.

[120] W. L. Xu, M. J. Zheng, S. Wu, and W. Z. Shen, "Effects of high-temperature annealing on structural and optical properties of highly ordered porous alumina membranes," *Appl. Phys. Lett,* vol. 85, pp. 4364-4366, 2004.

[121] G. Xiong, J. W. Elam, H. Feng, C. Y. Han, H. H. Wang, L. E. Iton, L. A. Curtiss, M. J. Pellin, M. Kung, H. Kung, and P. C. Stair, "Effect of Atomic Layer Deposition Coatings on the Surface Structure of Anodic Aluminum Oxide Membranes," *J. Phys. Chem. B,* vol. 109, pp. 14059-14063, 2005.

[122] W. L. Marshall and G. M. Begun, "Raman spectroscopy of aqueous phosphate solutions at temperatures up to 450 °C. Two liquid phases, supercritical fluids, and pyro- to ortho-phosphate conversions," *J. Chem. Soc., Faraday Trans. 2,* vol. 85, pp. 1963-1978, 1989.

[123] C. Rodehed, A. Gustafsson, and U. W. Gedde, "Electrical strength and chemical surface analysis of polypropylene after exposure to external partial discharges," *IEEE Trans. Dielectr. Electr. Insul.*, vol. 25, pp. 1066-1076, 1990.

[124] ____, *Polypropylene (PP) - Material Information* [Online]. Available: http://www.goodfellow.com/csp/active/STATIC/A/Polypropylene.HTML as of 8/29/2007.

[125] *Low Level Measurements Handbook, Precision DC Current, Voltage, and Resistance Measurements*, 6th ed. Cleveland, OH: Keithley Instruments Inc., 2004.

[126] *Model 2400 Series SourceMeter, User's Manual*, 7th ed. Cleveland, OH: Keithley Instruments, Inc., 2002.

[127] *HP4155A/4156A User's Dictionary Reference*, 3rd ed. Tokyo: Yokogawa-Hewlett-Packard, 1995.

[128] *HP4155A/4156A User's Task Guide*, 3rd ed. Tokyo: Yokogawa-Hewlett-Packard, 1995.

[129] R. B. Sadeghian and M. Kahrizi, "A novel miniature gas ionization sensor based on freestanding gold nanowires," *Sensors and Actuators A: Physical,* vol. 137, pp. 248-255, 2007.

[130] C. R. Rao and G. R. G. Raju, "Growth of ionization currents in dry air at high values of *E/N*," *J. Phys. D: Appl. Phys.,* vol. 4, pp. 494-503, 1971.

[131] H. C. Lee and R. S. Huang, "Simulation and design of field emitter array," *IEEE Electron Device Lett.,,* vol. 11, pp. 579-581, 1990.

[132] M. Ali Hassouba, F. Fahmy Elakshar, and A. Abuwali Garamoon, "Measurements of the breakdown potentials for different cathode materials in the Townsend discharge," *Fizika A,* vol. 11, pp. 81-90, 2003.

[133] R. B. Sadeghian and M. Kahrizi, "A Low Pressure Gas Ionization Sensor Using Freestanding Gold Nanowires," *Proc. IEEE-ISIE*, Vigo, Spain, 2007, pp. 1387-1390.

[134] ____, *OOPIC Pro User's Guide*, Boulder, CO: Tech-X Corporation, 2006.

[135] J. R. M. Vaughan, "A new formula for secondary emission yield," *IEEE Trans. Electron Devices,* vol. 36, pp. 1963-1967, 1989.

[136] J. Verboncoeur, "OOPIC users digest, Re: Electrode Circuit Current Measurement," L. Weber, Ed.: Tech-X Corporation, 2007.

[137] G. Petraconi, H. S. Maciel, R. S. Pessoa, G. Murakami, M. Massi, C. Otani, W. M. I. Uruchi, and B. N. Sismanoglu, "Longitudinal magnetic field effect on the electrical breakdown in low pressure gases," *Braz. J. Phys.*, vol. 34, pp. 1662-1666, 2004.

[138] C. Fall, "Ab initio study of the work functions of elemental metal crystals," Ph.D. dissertation, Dept. of Physics., EPFL, Lausanne, Switzerland, 1999.

[139] ____, *Gold. Wikipedia, the free encyclopedia* [Online]. Available: http://en.wikipedia.org/wiki/Gold as of 8/29/2007.

[140] G. Dittmer, "Electron conduction, electron emission and electroluminescence of MIM sandwich structures with Al_2O_3 insulating layers," *Thin Solid Films,* vol. 9, pp. 141-172, 1972.

[141] R. G. Forbes, "Field emission: New theory for the derivation of emission area from a Fowler-Nordheim plot," *Proc. 11th IEEE-IVMC*, Asheville, NC, 1999, pp. 526-533.

[142] I. Costina and R. Franchy, "Band gap of amorphous and well-ordered Al_2O_3 on $Ni_3Al(100)$," *Appl. Phys. Lett,* vol. 78, pp. 4139-4141, 2001.

[143] J. C. Fisher and I. Giaever, "Tunneling Through Thin Insulating Layers," *J. Appl. Phys.*, vol. 32, pp. 172-177, 1961.

[144] Negative electron affinity spark plug, by M. N. Yoder. (1996, Aug. 27). *Patent 5550425* [Online]. Available: http://www.freepatentsonline.com/5550425.html

[145] J. C. Brewer, R. J. Walters, L. D. Bell, D. B. Farmer, R. G. Gordon, and H. A. Atwater, "Determination of energy barrier profiles for high-k dielectric materials utilizing bias-dependent internal photoemission," *Appl. Phys. Lett,* vol. 85, pp. 4133-4135, 2004.

[146] J. Kim, J. Song, O. Kwon, S. Kim, C. S. Hwang, S.-H. K. Park, S. J. Yun, J. Jeong, and K. S. Hyun, "Improvement in electrical insulating properties of 10-

nm-thick Al_2O_3 film grown on Al/TiN/Si substrate by remote plasma annealing at low temperatures," *Appl. Phys. Lett,* vol. 80, pp. 2734-2736, 2002.

[147] N. S. Lee, D. S. Chung, I. T. Han, J. H. Kang, Y. S. Choi, H. Y. Kim, S. H. Park, Y. W. Jin, W. K. Yi, M. J. Yun, J. E. Jung, C. J. Lee, J. H. You, S. H. Jo, C. G. Lee, and J. M. Kim, "Application of carbon nanotubes to field emission displays," *Diamond and Related Materials,* vol. 10, pp. 265-270, 2001.

[148] Y. B. Tang, H. T. Cong, Z. G. Zhao, and H. M. Cheng, "Field emission from AlN nanorod array," *Appl. Phys. Lett,* vol. 86, pp. 153104 – 1-3, 2005.

[149] Y. Saito and S. Uemura, "Field emission from carbon nanotubes and its application to electron sources," *Carbon,* vol. 38, pp. 169-182, 2000.

[150] J. M. Kim, W. B. Choi, N. S. Lee, and J. E. Jung, "Field emission from carbon nanotubes for displays," *Diamond and Related Materials,* vol. 9, pp. 1184-1189, 2000.

[151] C. J. Lee, T. J. Lee, S. C. Lyu, Y. Zhang, H. Ruh, and H. J. Lee, "Field emission from well-aligned zinc oxide nanowires grown at low temperature," *Appl. Phys. Lett,* vol. 81, pp. 3648-3650, 2002.

[152] L. Liao, J. C. Li, D. F. Wang, C. Liu, C. S. Liu, Q. Fu, and L. X. Fan, "Field emission property improvement of ZnO nanowires coated with amorphous carbon and carbon nitride films," *Nanotechnology,* vol. 16, pp. 985-989, 2005.

[153] D. Banerjee, S. H. Jo, and Z. F. Ren, "Enhanced Field Emission of ZnO Nanowires," *Adv. Mater.,* vol. 16, pp. 2028-2032, 2004.

[154] A. Buldum and J. P. Lu, "Electron Field Emission Properties of Closed Carbon Nanotubes," *Phys. Rev. Lett.,* vol. 91, p. 236801, 2003.

[155] A. Batrakov, I. Pegel', and D. Proskurovskii, "Limitation of the field emission current density by the space charge of the emitted electrons," *Tech. Phys. Lett.,* vol. 25, pp. 454-455, 1999.

[156] G. Piantanida, A. Breskin, R. Chechik, O. Katz, A. Laikhtman, A. Hoffman, and C. Coluzza, "Effect of moderate heating on the negative electron affinity and

photoyield of air-exposed hydrogen-terminated chemical vapor deposited diamond," *J. Appl. Phys.*, vol. 89, pp. 8259-8264, 2001.

[157] A. Tomescu and R. Roescu, "Electron affinity changes induced by gaseous species present in the sourrounding atmosphere," *J. Optoelect. Adv. Mater.*, vol. 7, pp. 1529-1532, 2005.